EMISSION CHARACTERISTICS OF QUANTUM DISK-IN-NANOWIRE (QD-NW) LIGHT EMITTING DIODES

BY

IRFAN KHAN

A Thesis Presented to the
DEANSHIP OF GRADUATE STUDIES

KING FAHD UNIVERSITY OF PETROLEUM & MINERALS

DHAHRAN, SAUDI ARABIA

In Partial Fulfillment of the
Requirements for the Degree of

MASTER OF SCIENCE

In

ELECTRICAL ENGINEERING

APRIL 2015

KING FAHD UNIVERSITY OF PETROLEUM & MINERALS
DHAHRAN 31261, SAUDI ARABIA

DEANSHIP OF GRADUATE STUDIES

This thesis, written by **IRFAN KHAN** under the direction of his thesis adviser and approved by his thesis committee, has been presented to and accepted by the Dean of Graduate Studies, in partial fulfillment of the requirements for the degree of **MASTER OF SCIENCE IN ELECTRICAL ENGINEERING**.

Thesis Committee

Dr. Mohammad A. Alsunaidi
(Adviser)

Dr. Boon S. Ooi
(Member)

Dr. Hussain Ali Al-Jamid
(Member)

Dr. Ali Ahmad Al-Shaikhi
Department Chairman

Dr. Salam A. Zummo
Dean of Graduate Studies

17/6/15
Date

Dedicated to my beloved Parents

ACKNOWLEDGMENTS

I would like to thank my thesis advisor Dr. Mohammad A. Alsunaidi for his expert advice, appreciation and encouragement throughout this thesis. I would also like to thank my thesis committee members Dr. Hussain Ali Al-Jamid and Dr. Boon S. Ooi for their advice, valuable suggestions and positive feedback.

I would also like to thank my colleague and fellow graduate students at Noor Lab, KFUPM for their support. I am also thankful to King Fahd University of Petroleum and Minerals (KFUPM), Technology Innovation Center (TIC) on Solid State Lighting at KAUST and KAUST Photonics Lab for supporting this thesis.

TABLE OF CONTENTS

LIST OF TABLES

LIST OF FIGURES

LIST OF ABBREVIATIONS

DFPT	Density Functional Perturbation Theory
EBL	Electron Blocking Layer
FDTD	Finite Difference Time Domain
FWHM	Full Width Half Maximum
IQE	Internal Quantum Efficiency
LDA	Local Density Approximation
LED	Light Emitting Diode
MQW	Multiple Quantum Wells
PML	Perfectly Matched Layer
Q-FDTD	Quantum Coupled Finite Difference Time Domain
QCSE	Quantum Confined Stark Effect
QDNW	Quantum Disk in Nano Wire
QW	Quantum Well
SOR	Successive Over Relaxation

SQW	Single Quantum Well
SRH	Shockley Read Hall
SSL	Solid State Lighting
TDD	Threading Dislocation Density
UV	Ultra-Violet

THESIS ABSTRACT

NAME:	Irfan Khan
TITLE OF STUDY:	Emission characteristics of quantum disk-in-nanowire (QD-NW) Light Emitting Diodes
MAJOR FIELD:	Electrical Engineering
DATE OF DEGREE:	April, 2015

In this thesis, we have developed a time domain Q-FDTD (Quantum coupled Finite Difference Time Domain) model to study the emission characteristics of a Quantum-Disk-in-Nanowire (QD-NW) structure for solid state lighting applications. The Q-FDTD solver presented here is based on self-consistent solution of Schrödinger equation with the classical Drift-Diffusion model. The solver is developed for solving both one and two dimensional structures. Various physical properties of III-nitride materials such as spontaneous and piezoelectric polarization, electric field and doping dependence of mobility and diffusion coefficient are incorporated in the solver. Various electronic device properties such as I-V curves, recombination rates, band diagrams, carrier concentrations and electron hole wave function overlap are studied for the QD-NW structure. The 1D solver is used to *perform various parametric studies on an SQW structure. Parametric studies about the effects of crystal polarity, quantum well thickness, Indium concentration in the well, the effects of electron blocking layer and asymmetric quantum well are performed. The two dimensional solver is used to study the effect of the radius on the emission characteristics of the disk-in-nanowire structure. For fixed bias, the current density in the device increases with increasing the radius. The recombination rates increase with decreasing the radius. Similarly, when the radius of the nanowire increases, the overlap between electron and hole wavefunctions decreases.*

ملخص الرسالة

الاسم الكامل : عرفان خان

عنوان الرسالة : خصائص الانبعاث الضوئي لتشكيلات الأسلاك النانوية ذات القرص الكمومي

التخصص : الهندسة الكهربائية

تاريخ الدرجة العلمية : الرجب 1436

في هذه الرسالة تم تطوير نموذج محاكاة متكامل لدراسة خواص الانبعاث الضوئي لتشكيلات الأسلاك النانوية ذات القرص الكمومي (QD-NW) المبنية من مركب وخلائط نيترات الجاليوم GaN/InGaN والمستخدمة في الانارة. يعتمد هذا النموذج على دمج مجموعة مكونات في المجال الزمني (time domain) هي معادلة شرودنجر (Schrödinger) المعتمدة على الزمن لايجاد الطاقات الكمومية في منطقة القرص الكمومي وأشكال الدوال الكمومية المتعلقة بها، معادلة شدة التيار المبنية على الانجراف-الانتشار للشحنات (drift-diffusion) ، معادلة بوسون (Poisson) لإيجاد قوة وتوزيع المجالات الكهربائية داخل التشكيل ومعادلة الاستمرارية. هذا وقد أخذ بعين الاعتبار كل من اعتماد حركية الاجسام المشحونة على المجال الكهربائي الموضعي والطبيعة القطبية لنيترات الجاليوم حيث تتكون مجالات قطبية ذاتية وأخرى إجهاديه عند المنطقة البينية للطبقات المختلفة تؤثر في سلوك نطاقات الطاقة داخل المواد.

أستخدم الحل العددي للنموذج السابق باعتماد طريقة الفروقات المحدودة (Finite-difference Time-domain) مضافا اليها الحل العددي لمعادلة شرودنجر لتصبح QFDTD وذلك في بعد واحد وفي بعدين لاستخراج أهم خصائص التشكيل الباعث للضوء مثل علاقة التيار-الجهد (IV curves)، معدلات توليف الالكترون-الفجوة، تركيز ناقلات الشحنة، نطاقات الطاقة وتداخل الدوال الموجية للإلكترون والفجوة. هذا وقد أجريت دراسات متعددة على مجموعة من التشكيلات لدراسة أثر قطبية الشبيكة، سمك القرص الكمومي، تركيز الأنديوم (In)، قطر السلك النانوي، طبقة عزل الالكترونات وفقدان التماثل في منطقة القرص الكمومي. ولقد أظهرت نتائج المحاكاة ضعف تداخل الدوال الموجية للإلكترون والفجوة عند زيادة قطر السلك النانوي ومن ثم تدني مستوى الانبعاث الضوئي.

CHAPTER 1

INTRODUCTION

Since the invention of the incandescent bulb in the 18th century, different methods of generating white light efficiently have been investigated. Roughly, more than $1/5^{th}$ of the electricity produced in the US is used to power artificial lighting [1]. If all the artificial lighting sources are converted to energy-efficient LED sources, worldwide energy consumption could be reduced by around 1000 TWh/yr, equivalent to 230 typical 500 MW coal plants, reducing greenhouse green emission by about 200 million tons a year [2]. White light emitting sources based on energy efficient LEDs have recently been made possible with the advent of direct bandgap III-Nitride materials with luminous efficiencies of over 100 lm/W [2].

LED technology offers a lot of advantages over conventional incandescent and fluorescent light bulbs like high energy efficiency, longer lifetime, directional light, robustness, dimming capability without colour shifting, absence of hazardous substances like mercury, absence of heat or UV in light beam, low-voltage d.c. operation and design flexibility [3]. The recent progress in efficiency enhancement of nitride based LEDs, as shown in Fig. 1.1, has led to a steadily increasing adoption of solid state lighting which is expected to replace incandescent lighting and even fluorescent lamps in the near future [4].

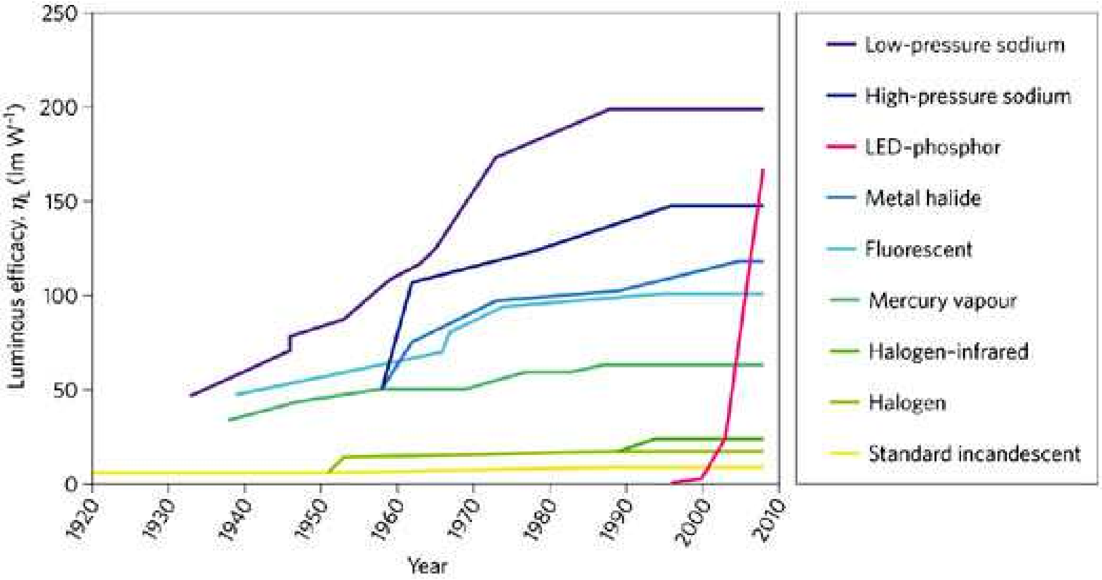

Figure 1.1: Progress in the improvement of luminous efficiency of different white light generating sources with time[5]

1.1 III-Nitride Materials for Light Emitting Devices

Group III-nitride materials refer to Gallium Nitride (GaN), Indium Nitride (InN), Aluminum Nitride (AlN) and their binary and ternary alloys. These materials have been under intense investigation due to their possible applications in light emitting devices in the spectral range from the visible to ulta-voilet (UV) region. The band gap of III-Nitride materials can be varied in a wide spectral range from 0.65 eV to 6.13 eV. This large variation in bandgap is obtained by alloying GaN with InN and AlN. GaN, when alloyed with InN, a bandgap in the range of 0.65-3.42 eV can be achieved. Similarly, when alloyed with AlN, a bandgap in the range of 3.42-6.13 eV can be obtained.

1.2 Conventional White LED Devices

Due to significant progress in the development of white light LEDs, high efficiency white light LEDs can be manufactured. The most popular approaches are: blue LED with yellow phosphors; UV LED with blue and yellow phosphors and a combination of red, green and blue LEDs in a single device [5]. Blue LED and yellow phosphor have high theoretical efficacy, but have very low color-rendering index (CRI) which makes them undesirable for indoor use. On the other hand, UV LEDs with phosphor mixtures have better CRI, but have very poor efficacy. The combination of red, green and blue LEDs is an attractive choice but is not cost effective and production of green light is not very efficient [4]. Conventional and QW III-nitride LEDs also suffer from efficiency droop and large density of threading dislocations due to high lattice mismatch substrates which degrade optical emission efficiency [6].

1.3 Nano-Structures for Efficiency Enhancement

One focus of the current research in white light emitting diodes is the enhancement of the efficiency of LEDs for lighting by using nano-structures [7]. Various nano-structures like quantum dots [8, 9, 10], nanowires/nanorods [11], nanodiscs [12] are proposed in the literature. Fig. 1.2 shows some recent nano-structures used for increasing the efficiency of LED's.

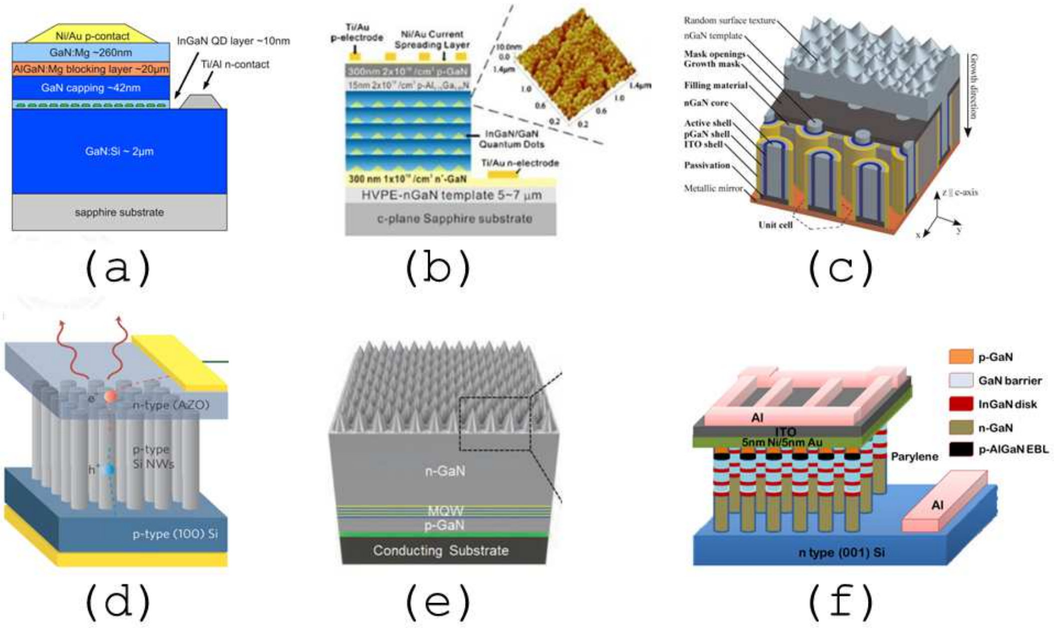

Figure 1.2: Nanostructures for efficiency enhancement (a) Single QD layer [13], (b) Multiple quantum dots layers [14], (c) Core shell nanorod structure [15], (d) Nanowire structure [16],(e) Cone shaped nano-structure [17], (f) Quantum disks in nanowires structure [18]

1.3.1 Advantages of Nano Structures

Compared to conventional and planar QW structures, nanostructured devices such as nanowires have advantages which include [11]

- Strain in nanostructures is relaxed due to which threading dislocations can be lower, and conversion efficiency is enhanced.
- Quantum confined stark effect (QCSE) which arises in quantum wells due to large polarization fields is absent in nanowires [18].
- Due to small cross sections, nanowires can accommodate higher lattice mismatch with the substrate, which allows defect free growth on a variety of substrates [19].
- Lower strain induced defects allow for higher indium content and more flexibility in bandgap engineering, which could lead to full spectrum light emitting diodes.
- Nanostructures in the active region provide high confinement and hence higher temperature stability of threshold current and luminescence.
- High crystalline quality of nanowires persists when quantum heterostructures like quantum discs are incorporated in them [20].

1.4 Quantum-Disk-in-Nanowire Structure

The Quantum Disk in Nano Wire (QD-NW) structure is the subject of this thesis. The QD-NW structures are exciting due to the fact that they can provide an alternative to phosphor based white light emitting diodes. The quantum disks in QD-NW structure can be tuned to obtain broad emission spectrum or emission of dual or multiple wavelengths, which combine to produce white light [21]. The inclusion of quantum disc heterostructures inside GaN nanowire (QD-NW) opens new prospects for light emitting devices and the possibility to cover the full visible spectrum [22].

Despite recent progress in nitride structures, experimental results on optical properties of QD-NW structures are scarce and demand numerical investigations. The physics of these devices is not fully transparent [7], which also makes them harder to analyze experimentally. Numerical simulations help to bridge the gap between theory and experiment. They can also help to understand the nanoscale effects influencing the performance of the device that cannot be explained experimentally. Therefore, advanced numerical simulation models for such devices need to be developed for future advancements. In this thesis, a finite difference time domain coupled Poisson-Schrodinger model for QD-NW LEDs is developed to study and analyze light emission properties of quantum disk in nanowire structure as shown in Fig. 1.3 for solid state lighting applications.

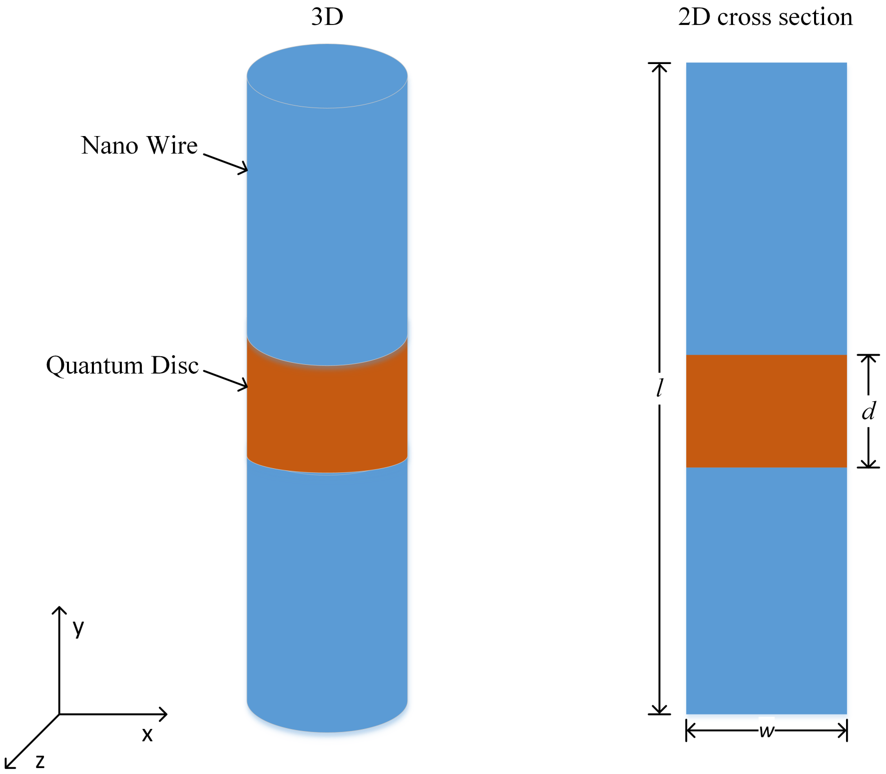

Figure 1.3: Schematic of the Disk in Nanowire structure studied in this thesis.

1.5 Literature Review

Due to the unique properties of GaN material, it has been subject to intense research in the past decade. Despite this, there is still considerable disagreement regarding its physical properties. Large background n-type carrier concentration, the difficulty in p-type doping and the lack of lattice matched substrate materials were the main difficulties that discouraged researchers in the past [23]. In 1989, p-doping of GaN was realized with Mg-doped GaN by Amano *et al.* [24] and later in 1991, Nakamura *et al.* reported the first high power GaN blue homojunction LED [25]. Double heterojunction LED's with low FWHM (Full Width Half Maximum) and high external quantum efficiency were also first reported in 1993 by Nakamura *et al.* [26]. This heterojunction was acheived by sandwitching an InGaN active layer between GaN n and p contact layers. Following these early breakthroughs, III-nitride material have been the subject of intense experimental research and numerical investigations.

The development of numerical models is important for LED optimization and development. Some of the numerical models developed for the simulation of transport equations are summarized below

- Self-consistent solution of Poisson and Schrödinger equations for semiconductor heterostructures in multiband k.p framework using finite element formulation [27]
- A quantum corrected energy transport model for simulation of nanoscale semiconductor devices using the density gradient (DG) model is presented in [28].
- A microscopic model based on full Brillouin zone electronic structure to study Auger transitions in InGaN/GaN quantum wells is presented in [29]. The dependence of Auger coefficients on temperature and QW thickness is analyzed.
- Modelling and optimization of electric current spreading in III-nitride base light emitting diode in performed using Finite Volume method and Montecarlo ray tracing technique [30]
- One-dimensional drift-diffusion model for group III-nitrides is used to sim-

ulate carrier transport and recombination properties [31].

Using different numerical solvers numerous studies have been performed to investigate the properties of III-nitride materials. Most of these studies are performed with commercial CAD softwares like APSYS, SiLENSE, TiberCaD, COMSOL etc. A few examples of the numerical studies performed over III-nitride material devices are:

- Modeling of injection characteristics of III-nitride polar and non-polar MQW structures is presented in [32]. COMSOL simulation tool is used for solving the Drift-Diffusion model. It was found that polarization-matched design of electron-blocking layer can noticeably improve the injection uniformity in polar MQW structure and enhance the internal quantum efficiency.

- Effect of quantum barrier (QB) thickness on electric field in the MQW active region of GaN/InGaN LED, the influence of QB thickness on the IQE, the emission wavelength shift with injection current and on the efficiency droop are discussed in [33]. Using APSYS simulation tool, it was found that thinner QBs result in a smaller electric field in the quantum wells. The smaller electric field in the quantum wells leads to a better efficiency performance and better carrier confinement due to a smaller QCSE.

- The effect of dislocation density of light emission efficiency in gallium nitride is presented in [34]. They found that dislocation density must be reduced to $\approx 10^7\ cm^{-2}$ to get emission efficiency close to unity.

- Investigation of the quantum well width dependence of the ground level emission of GaN/AlGaN quantum wells is performed in [35]. It was found that for quantum well widths larger than 3 *nm*, the luminescence intensity reduce with increasing QW thickness.
- The impact of electron leakage on the internal quantum efficiency droop is investigated using APSYS simulation tool by Piprek *et al.* [36]. They found that for suppression of electron leakage, it is important to achieve high Mg acceptor doping densities at the interface between blocker layer and the last quantum well barrier. Contrary to common assumptions, it was found that electron leakage decreases with increasing temperature.
- The effect of temperature and drive current on the light output and efficiency of blue InGaN/GaN LEDs is discussed in [37].

The incorporation of quantum effects in numerical solvers is a relatively recent idea. Due to the recent nature of the subject very limited number of studies has been performed to model and simulate electronic and optical properties of nano structures. Electronic and optoelectronic properties of InGaN based nanocolumn quantum disk LEDs are investigated by Lopez *et al.* [22] with multiscale simulation tool tiberCAD. Calculations are performed with an atomistic tight-binding model. For particle transport, Poisson/Drift-Diffusion models are solved using a finite element mesh. It is found that the variation of nanocolumn width has only minor effects on the electronic and optical properties of the QD active region. Riguitti *et al.* investigates electronic transport in GaN nanowires with a single GaN/AlN quantum disc or multiple GaN/AlN quantum discs [6]. They found out that if the quantum disks are surrounded by a GaN shell, the electron transport is restricted to a narrow surface region, leading to high dependence of the conductivity of the structure on environmental conditions. In case no GaN shell is present, electron transport occurs by tunneling through the quantum disk structure giving rise to a negative differential resistance in the I-V curves. Kölper *et al.* presents a coupled electronic and optical model to derive efficiency estimation and design rules of electrically driven core-shell nanorod LEDs. The model takes carrier density dependent internal quantum efficiency (IQE) as well as reabsorption and photon recycling in m-plane quantum wells into account. Empirical rate equation model calibrated on measurements of thin film structures is used for current density dependent emission. Light extraction and Purcell enhancement of the spontaneous emission are obtained by FDTD simulations, solving Maxwell equations [15].

Electronic and optical properties of nano-structured LEDs are affected by various factors such as surface charges, surface recombination and piezoelectric effects. Surface charge and surface recombination effects on an InGaN/GaN quantum disk in nano wire LED are investigated by Römer *et al.* using numerical simulations [7]. The implementation of the simulation model considers surface effects using a numerically accurate true area box method discretization. The transport and the Schrödinger solver are executed in a self-consistent Gummel iteration. Both effects have been found to decrease the internal quantum efficiency. To numerically investigate the influence of linear and nonlinear piezoelectric fields on the electronic and optical properties of GaN/InN/GaN disk-in-wire LED structures, Yalavarthi *et al.* used a combination of fully atomistic valence force-field molecular mechanics and 10-band sp^3s^*-SO tight binding electronic band structure models. They used the open source NEMO 3-D software as a computational framework. The calculations show that 2^{nd} order piezoelectric contribution has insignificant effects on the overall electronic and optical properties in reduced dimensionality nanoscale disk-in-wire LED structures [38].

The numerical models described above deal with the confinement problem in the steady state only. To the best of our knowledge no time domain models for solving the Schrödinger equation were reported in the literature, for studying the emission properties of the QD-NW LEDs.

1.6 Thesis Objectives

The main objective of this thesis is to study the emission properties of a Quantum Disk in a Nanowire (QD-NW) LED using a self-consistent time domain Q-FDTD solver.

Specific objectives are given below

- To perform an extensive literature survey on QD-NW structures.
- To develop an FDTD solver for one and two dimensional Schrödinger equation.
- To couple the FDTD model of the Schrödinger equation to Poisson and Transport equations.
- To study the effect of different parameters that characterize the behavior of QD-NW structures.
- To extend to the Q-FDTD model to simulate a QD-NW based light emitting diode.
- To perform various parametric studies like I/V curves, recombination rates etc on the QD-NW based LED.

1.7 Thesis Organization

This thesis is organized as follows.

Chapter 1 presents an overview of GaN based LED devices and the importance of numerical modeling and simulation in the development of these devices. This chapter also presents literature review and thesis objectives.

Chapter 2 presents the essential theoretical background for modeling of III-Nitride based semiconductor devices. Detailed description and expressions are provided for Poisson equation, Schrödinger equation, Current continuity equation and Drift-Diffusion equation both in the bulk region and in the quantum well structure.

Chapter 3 discusses the transport and material properties of III-Nitride materials. Specifically, it discusses the field dependent mobility and diffusion coefficient, spontaneous and piezoelectric polarization and recombination properties of III-Nitride materials and its alloys.

Chapter 4 presents the Q-FDTD algorithm. Discretized equations for Poisson equation, Schrödinger equation, Current Continuity equation and Drift-Diffusion current equations are presented in this chapter.

Chapter 5 contains the simulation results for one-dimensional Disk-in-Nanowire GaN based light emitting diode performed using the Q-FDTD solver.

Chapter 6 contains the simulation results for a two-dimensional single quantum well structure obtained using the Q-FDTD solver.

Chapter 7 contains summary and conclusion. It also suggests possible future work related to this thesis.

CHAPTER 2

THEORETICAL BACKGROUND

In this chapter, the essential theoretical background for modeling semiconductor devices is presented. We discuss in detail Poisson equation, Schrödinger equation, Current continuity equation and Drift-Diffusion equation both in the bulk region and in the quantum well structure.

2.1 Poisson Equation

Poisson equation is used to determine the electrostatic potential distribution due to charge density and applied external fields. Poisson equation is derived from Maxwell's equation given as

$$\vec{\nabla} \cdot \vec{D} = \rho \tag{2.1}$$

where, $\vec{D}$ is the electric flux density and ρ is the total charge density. Using

$\vec{D} = \varepsilon \vec{E}$ and $\vec{E} = -\nabla V$, (2.1) can be written as

$$-\vec{\nabla} \cdot (\varepsilon \nabla V) = \rho \tag{2.2}$$

where, V is the electrostatic potential and ε is the dielectric permitivity of the material.

2.1.1 Poisson Equation for Bulk Region

In case of III-nitride materials there are large built-in electric field in the material due to spontaneous and piezoelectric polarization. Incorporating total polarization field $\mathbf{P^{tot}}$ in (2.2), Poisson equation can be written as [39]

$$\vec{\nabla} \cdot \left(\mathbf{P^{tot}} - \hat{\varepsilon}^{*} \nabla V\right) = \rho = q_e \left(N_D^+ - N_A^- + p - n\right) \tag{2.3}$$

Here, n and p are the electron and hole concentrations and N_D^+ and N_A^- are the concentration of ionized donors and acceptors, respectively. $\hat{\varepsilon}^{*}$ is the effective dielectric permitivity tensor with the diagonal component given by

$$\varepsilon_{11}^{*} = \varepsilon_{22}^{*} = \varepsilon_0 \varepsilon_{11} + \frac{e_{15}^2}{C_{44}} \tag{2.4}$$

$$\varepsilon_{33}^{*} = \varepsilon_0 \varepsilon_{33} + \frac{e_{33}^2}{C_{33}} \tag{2.5}$$

In (2.4) and (2.5), ε_{ij}, e_{ij} and C_{ij} are the components of relative permitivity tensor, piezoelectric tensor and stiffness tensor, respectively, whose values for III-nitrides are given in Table 3.6. ε_0 is the permitivity of free space. The concentration of ionized donors (N_D^+) and acceptors (N_A^-) in (2.3) is given by [40]

$$N_D^+ = \frac{N_D}{1 + g_D \exp\left(\dfrac{E_{fn} - E_c - q_e V + E_D}{k_B T}\right)} \tag{2.6}$$

$$N_A^- = \frac{N_A}{1 + g_A \exp\left(\dfrac{E_v - E_{fh} - q_e V + E_A}{k_B T}\right)} \tag{2.7}$$

where,

$k_B = Boltzmann\ constant, (eV/K)$

$T\ = Lattice\ Temperature, (K)$

$E_{fh} = Fermi\ level\ for\ holes, (eV)$

$E_{fn} = Fermi\ level\ for\ electrons, (eV)$

$g_D = Donor\ degeneracy\ factor,\ 2$

$g_A = Acceptor\ degeneracy\ factor,\ 4$

$E_v = Top\ of\ the\ valence\ band,\ (eV)$

$E_c = Bottom\ of\ the\ conduction\ band,\ (eV)$

$E_D = Donor\ Ionization\ energy, (eV)$

$E_A = Acceptor\ Ionization\ energy, (eV)$

$N_A = Doping\ concentration\ of\ holes,\ (cm^{-3})$

$N_D = Doping\ concentration\ of\ electrons,\ (cm^{-3})$

2.1.2 Poisson Equation for Quantum Well

Due to the bound carrier density in the quantum well layers, Poisson equation in (2.3) can be re-written as

$$\vec{\nabla} \cdot \left(\mathbf{P^{tot}} - \hat{\varepsilon}^{*} \nabla V\right) = q_e \left(N_D^+ - N_A^- + p - n + p_{QW}^{3D} - n_{QW}^{3D}\right) \tag{2.8}$$

where, $n_{QW}^{3D} = n_{QW}/L_{QW}$ and $p_{QW}^{3D} = p_{QW}/L_{QW}$. L_{QW} is the width of the quantum well. n_{QW} and p_{QW} are the bounded carrier concentration of electrons and holes in the quantum well, respectively.

2.2 Schrödinger Equation

Schrödinger equation describes how the wavefunction of a physical system evolves over time. Schrödinger equation is given by [41]

$$\frac{\partial^2 \psi(r,t)}{\partial t^2} = \frac{1}{\hbar} \left(\frac{\hbar^2}{2m} \nabla^2 - U(r,t) \right)^2 \psi(r,t) \tag{2.9}$$

where, $\hbar$ is the reduced Plank's constant, U is the potential energy, m represents the mass and ψ is the state variable. The parameter ψ does not have a direct physical meaning itself, but a number of meaningful quantities like position, momentum, kinetic and potential energy can be determined from it [42]. Equation (2.9) is second order in time and fourth order in space. If we consider ψ to be a complex function, then (2.9) can be simplified to

$$j\hbar\frac{\partial\psi(r,t)}{\partial t} = \left(-\frac{\hbar^2}{2m}\nabla^2 + U(r,t)\right) \tag{2.10}$$

By substituting $\psi = \psi_{re} + j\psi_{im}$ in (2.10) and then equating real and imaginary parts to each other, we get two coupled equations given by

$$\frac{\partial\psi_{re}(r,t)}{\partial t} = \frac{1}{\hbar}\left(-\frac{\hbar^2}{2m}\nabla^2 + U(r,t)\right)\psi_{im}(r,t) \tag{2.11}$$

$$\frac{\partial\psi_{im}(r,t)}{\partial t} = \frac{1}{\hbar}\left(+\frac{\hbar^2}{2m}\nabla^2 - U(r,t)\right)\psi_{re}(r,t) \tag{2.12}$$

2.2.1 Band Alignment

The alignment of energy bands in the heterojunctions for the quantum well is performed using the Anderson's rule [43] also referred to as the electron affinity rule. According to electron affinity rule, when constructing the energy band diagram, the vacuum levels of all the semiconductors must be at the same energy level. Once the vacuum levels are aligned, electron affinity χ and energy band gap E_g of each semiconductor material is used to calculate the conduction and valence band offsets as shown in Fig. 2.1. Conduction band offset at the heterojunction interface can found from

$$\Delta E_c = \chi_2 - \chi_1 \tag{2.13}$$

Valence band offset is calculated as

$$\Delta E_v = (\chi_1 + E_{g_1}) - (\chi_2 + E_{g_2}) \tag{2.14}$$

where, χ_1 and χ_2 are the electron affinities and E_{g_1} and E_{g_2} are the band gap energies at each side of the hetero-junction interface.

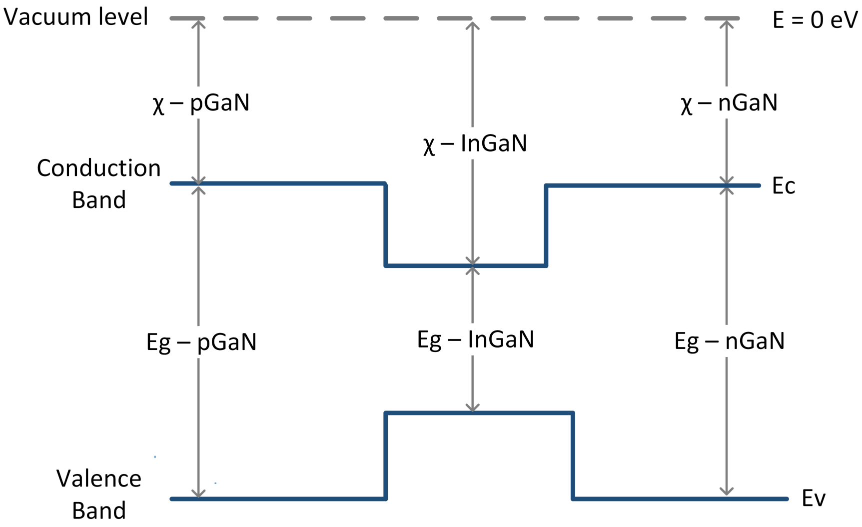

Figure 2.1: Schematic for band alignment for a quantum well structure using Anderson's rule.

2.3 Drift-Diffusion Current Model

The two main effects which lead to current flow in semiconductors are the drift and diffusion of carriers. Drift current arises due to the influence of electric field, while Diffusion current is obtained due to concentration gradient of the carriers.

2.3.1 Drift Current

In semiconductors, carriers when subjected to an electric field accelerate and attain a certain drift velocity. The drift velocity of holes is in the direction of the electric field, while electrons accelerate in the opposite direction. Drift current can be expressed in terms of Ohm's law as

$$\begin{aligned} J_n^{drift} &= \sigma_n E \\ J_h^{drift} &= \sigma_h E \end{aligned} \tag{2.15}$$

where, E is the electric field and $\sigma_{n(h)}$ is the conductivity of electrons or holes. Conductivity can be expressed in terms of carrier concentration and mobility as

$$\begin{aligned} \sigma_n &= q_e n \mu_n \\ \sigma_h &= q_e p \mu_h \end{aligned} \tag{2.16}$$

By substituting the expression for conductivity from (2.16) in (2.15), the equation for drift current can be written as

$$\begin{aligned} J_n^{drift} &= q_e n \mu_n E \\ J_h^{drift} &= q_e p \mu_h E \end{aligned} \tag{2.17}$$

2.3.2 Diffusion Current

Diffusion current is the result of concentration gradient of carriers in semiconductor devices. Carrier diffusion occurs due to the thermal energy of carriers which tend to redistribute from high concentration areas to lower concentration regions. The expression for Diffusion current can be written as

$$\begin{aligned} J_n^{diff} &= +q_e D_n \nabla n \\ J_h^{diff} &= -q_e D_h \nabla p \end{aligned} \tag{2.18}$$

where, D_n and D_h are the diffusion coefficients for electrons and holes, respectively.

Total current is obtained by adding the drift current from (2.17) and the diffusion current from (2.18) as given by

$$J_n = q_e \mu_n n E + q_e D_n \nabla n \tag{2.19}$$

$$J_h = q_e \mu_h p E - q_e D_h \nabla p \tag{2.20}$$

2.3.3 Thermionic Emission in the Bulk

At abrupt hetero-junctions, drift diffusion model fails due to the band edge discontinuity. Carriers can become hot due to injection from wide bandgap into a narrower bandgap material [44]. For hetero interface between two bulk materials, carrier transport can be approximated by coupling drift-diffusion on both sides of the hetero-junction and thermionic emission at the interface [45]. Thermionic emission current for electrons across the hetero-junction interface as shown in Fig. 2.2 is given by [46]

$$J_n = -q_e v_{n_1} n_1(0^-) \exp\left(-\frac{\Delta E_c}{k_b T}\right) + q_e v_{n_2} n_2(0^+) \tag{2.21}$$

where, $n_1(0^-)$ and $n_2(0^+)$ are electron concentrations, ΔE_c is the difference between the conduction band energy level on each side of the interface and v_n is the mean thermal velocity of electrons given by

$$v_{n_i} = \frac{A^* T^2}{q_e N_{c_i}} \quad , \quad i = 1, 2 \tag{2.22}$$

Here, N_c is the electron density of states, T is the lattice temperature and $A^* = m^* k_b^2/(2\pi^2\hbar^3)$ is the effective Richardson constant [47] for electrons. The effective mass m^* in the Richardson constant is typically chosen as the smaller of the two effective masses across the interface [48]. By using different values of effective Richarson constant, it is possible to include tunneling effect as well as propagation from direct to indirect semiconductor materials and vice-versa [49].

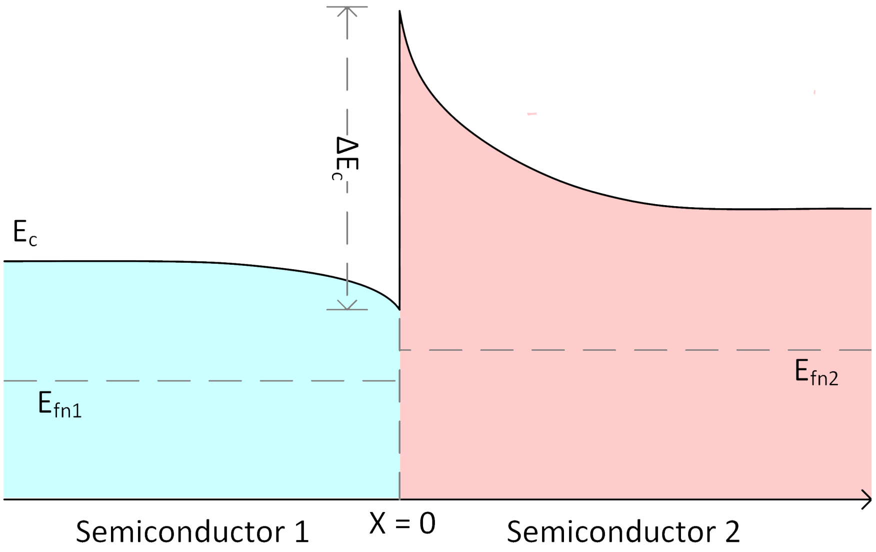

Figure 2.2: Schematic band diagram of an abrupt heterojunction interface. E_{fn1} and E_{fn2} represents the Fermi level across each side of the interface.

Similarly, thermionic emission current for holes can be written as [46]

$$J_h = q_e v_{h_1} p_1(0^-) \exp\left(-\frac{\Delta E_v}{k_b T}\right) - q_e v_{h_2} p_2(0^+) \tag{2.23}$$

$$v_{h_i} = \frac{A^* T^2}{q_e N_{v_i}} \qquad , \qquad i = 1, 2 \tag{2.24}$$

where, $p_1(0^-)$ and $p_2(0^+)$ are hole concentrations, ΔE_v is the difference between the valence band energy level, v_h is the mean thermal velocity of holes and N_v is the holes density of states at each side of the interface. In case of thermionic emission, carriers injected from material 1 scatter into thermal equilibrium in material 2. This assumption is valid only when the hetero-junction is between two bulk materials, because most of the carriers crossing the interface will scatter within a mean free path of a few nanometers [44].

2.3.4 Thermionic Emission in the Quantum Well

For hetero-junctions with quantum wells, thermionic emission coupled to drift-diffusion model cannot be used in its current form to describe carrier transport. Since the size of the quantum well is of the order or smaller than the mean free path, there is a non zero probability that the injected carriers will traverse the QW without being scattered into a bound state. For this reason, thermionic emission in sub-section 2.3.3 is modified with the introduction of capture and escape currents for transport across quantum wells. Fig. 2.3 shows the schematic diagram of the conduction band edge of a quantum well sand-witched between bulk material. The figure shows the bulk states outside the QW, the continuum states above the well and bound states which consist of the eigenstates with energy below the confining energy of the quantum well.

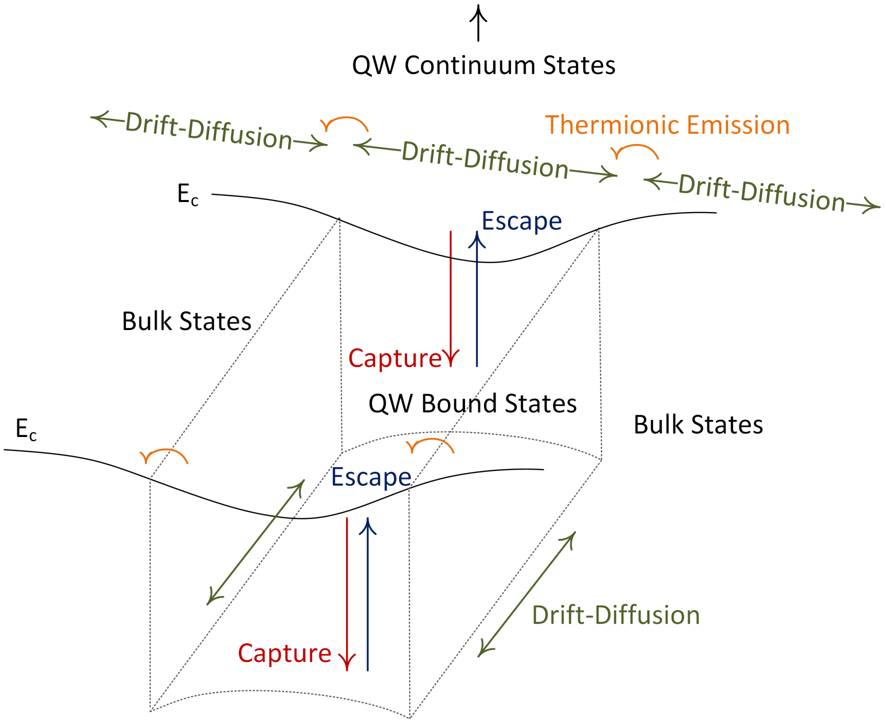

Figure 2.3: Schematic diagram of an abrupt heterojunction interface with quantum well.

Fig. 2.3 shows that carriers move via drift-diffusion in the bulk region. At the QW interface, carriers are injected into the continuum states of the QW using thermionic emission. Carriers from continuum states are captured into the bound states via capture current, where they are distributed in real space according to eigen-functions determined by Schrödinger equation. From bound states, carriers can either jump back to the continuum states via escape current or recombine. Carriers can move freely in directions parallel to the QW interfaces via drift-diffusion current.

Capture Current

Capture current is the result of carriers jumping from the continuum states to the bound states of the quantum well. The expression for finding the capture current for electrons can be written as [50]

$$J_{n,QW}^{cap} = -q_e n \left(\frac{kT}{2\pi m_{e,\parallel}}\right)^{1/2} \exp\left(\frac{-E_c + E_{e,1}}{kT}\right) \tag{2.25}$$

where, n is the electron concentration in the continuum states, $m_{e,\parallel}$ is the inplane mass of electrons, E_c is bottom of the conduction band in the quantum well and $E_{e,1}$ is the lowest lying quasi bound eigen state in the well.

Similarly, capture current for holes can be calculated using

$$\begin{aligned} J_{h,QW}^{cap} = q_e p \left(\frac{kT}{2\pi m_{hh,\parallel}}\right)^{1/2} \exp\left(\frac{E_v - E_{hh,1}}{kT}\right) \\ + q_e p \left(\frac{kT}{2\pi m_{lh,\parallel}}\right)^{1/2} \exp\left(\frac{E_v - E_{lh,1}}{kT}\right) \end{aligned} \tag{2.26}$$

where, p is the holes concentration in the continuum states, $m_{hh,\parallel}$ and $m_{lh,\parallel}$ is the inplane mass of heavy and light holes, E_v is top of the valence band and $E_{hh,1}$ and $E_{lh,1}$ is the first eigen state in the quantum well for heavy and light holes, respectively. The values of $E_{e,1}$, $E_{hh,1}$ and $E_{lh,1}$ are calculated by solving the Schrödinger equation.

Escape Current

Escape current is due to the carriers jumping from the bound states to the continuum states of the quantum well. Escape current for electrons can be written as [50]

$$J_{n,QW}^{esc} = q_e n_{QW}^{3D} \left(\frac{kT}{2\pi m_{e,\|}} \right)^{1/2} \exp\left(\frac{-E_c + E_{e,1}}{kT} \right) \tag{2.27}$$

where, $n_{QW}^{3D} = n_{QW}/L_{QW}$ is the concentration of electrons in the bounded states. Escape current for holes can be derived from

$$\begin{aligned} J_{h,QW}^{esc} = -q_e p_{QW}^{3D} \left(\frac{kT}{2\pi m_{hh,\|}} \right)^{1/2} \exp\left(\frac{E_v - E_{hh,1}}{kT} \right) \\ - q_e p_{QW}^{3D} \left(\frac{kT}{2\pi m_{lh,\|}} \right)^{1/2} \exp\left(\frac{E_v - E_{lh,1}}{kT} \right) \end{aligned} \tag{2.28}$$

where, $p_{QW}^{3D} = p_{QW}/L_{QW}$ is the concentration of bounded holes in the quantum well.

2.4 Current Continuity Equation

The current continuity equation is position and time dependent equation which contains all the main carrier actions like drift, diffusion, recombination and generation under bias [51]. For quantum well structures, carrier capture and escape also need to be incorporated as shown in Fig. 2.4. Current continuity equation is defined differently in the bulk and quantum well regions. In this section, we derive separate equations for the current continuity equation in the bulk and quantum well region.

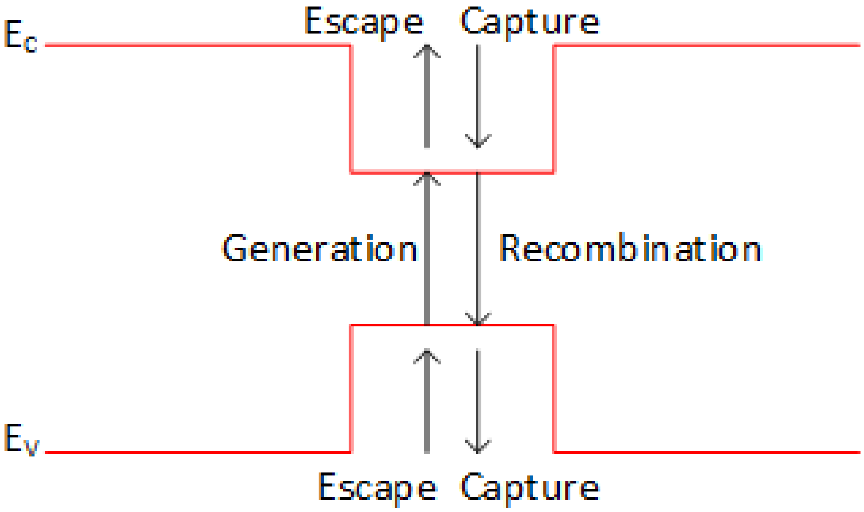

Figure 2.4: Schematic diagram for different carrier actions in the quantum well.

2.4.1 Current Continuity Equation in the Bulk

The current continuity equation for electrons and holes in the bulk states can be derived from Maxwell equation given by

$$\vec{\nabla} \times H = \vec{\nabla} \cdot J + \frac{\partial D}{\partial t} \tag{2.29}$$

By taking the divergence $(\vec{\nabla}\cdot)$ of both side, (2.29) can be written as

$$\vec{\nabla} \cdot (\vec{\nabla} \times H) = \vec{\nabla} \cdot \vec{\nabla} \cdot J + \vec{\nabla} \cdot \frac{\partial D}{\partial t} \tag{2.30}$$

Since, the divergence of the curl of any vector field is equal to zero, splitting current density into electron and hole current density, $J = J_n + J_h$ and using (2.1) and (2.2), equation (2.30) can be written as

$$\nabla \cdot J_n + \nabla \cdot J_h + q_e \left(\frac{\partial p}{\partial t} - \frac{\partial n}{\partial t} - \frac{\partial N_A^+}{\partial t} + \frac{\partial N_D^-}{\partial t} \right) = 0 \tag{2.31}$$

Since, the ionized charge densities N_D^+ and N_A- are time invariant, their time derivative is zero. Equation (2.31) can be split into two independent equations for electrons and holes as given below

$$\nabla \cdot J_n - q_e \frac{\partial n}{\partial t} = q_e R \tag{2.32}$$

$$\nabla \cdot J_h + q_e \frac{\partial p}{\partial t} = -q_e R \tag{2.33}$$

where, R is the total recombination rate for electrons and holes. By rearranging equation (2.33), it can be written in more popular form as [52]

$$\frac{\partial n}{\partial t} = +\frac{1}{q_e} \nabla \cdot J_n - R \tag{2.34}$$

$$\frac{\partial p}{\partial t} = -\frac{1}{q_e} \nabla \cdot J_h - R \tag{2.35}$$

2.4.2 Current Continuity Equation in the Quantum Well (Continuum States)

The current continuity equation for electron and holes in the QW continuum states can be written as [50]

$$\frac{\partial n}{\partial t} = +\frac{1}{q_e}\left(\nabla \cdot J_n + J_{n,QW}^{3D}\right) - R \tag{2.36}$$

$$\frac{\partial p}{\partial t} = -\frac{1}{q_e}\left(\nabla \cdot J_h + J_{h,QW}^{3D}\right) - R \tag{2.37}$$

where, $J_{n,QW}^{3D}$ and $J_{h,QW}^{3D}$ are calculated from the net current density between the the continuum and bound states of the quantum well as

$$J_{n(h),QW}^{3D} = \begin{cases} \dfrac{J_{n(h),QW}}{L_{QW}} & Inside\ QW \\ 0 & Otherwise \end{cases} \tag{2.38}$$

Here, L_{QW} is the width of the quantum well.

2.4.3 Current Continuity Equation in the Quantum Well (Bound States)

The current continuity equations for quantum well includes generation, recombination and carrier exchange between the continuum states and bounded states of the quantum well via capture and escape currents. For electrons and holes, current continuity equations can be written as [50]

$$\frac{\partial n_{QW}}{\partial t} = -\frac{1}{q_e} J_{n,QW} + G_{QW} - R_{QW} \tag{2.39}$$

$$\frac{\partial p_{QW}}{\partial t} = +\frac{1}{q_e} J_{h,QW} + G_{QW} - R_{QW} \tag{2.40}$$

where, n_{QW} and p_{QW} are the two dimensional electron and hole densities, R is the recombination rate and G is the carrier generation rate in the quantum well. $J_{n,QW}$ and $J_{h,QW}$ represent the net current density between the continuum and bound states of the quantum and can be written as

$$J_{n,QW} = J_{n,QW}^{esc} + J_{n,QW}^{cap} \tag{2.41}$$

$$J_{h,QW} = J_{h,QW}^{esc} + J_{h,QW}^{cap} \tag{2.42}$$

2.5 Carrier Concentration in the Bulk at Steady State

At steady state, carrier concentration in the bulk semiconductor is obtained by integrating the product of Density-of-State (DOS) function and equilibrium probability distribution function over the the entire range of conduction or valence band for electrons and holes, respectively. The corresponding equations for carrier concentration during equilibrium is given by [53]

$$n = \int_{E_c}^{\infty} D_n(E) f_n(E) dE \tag{2.43}$$

$$p = \int_{0}^{E_v} D_h(E) f_h(E) dE \tag{2.44}$$

where, $D_n(E)$ and $D_h(E)$ are the Density of States, $f_n(E)$ and $f_n(E)$ are Fermi-Dirac probability distribution functions for electrons and holes, respectively. The Density of States for electrons and holes is given by

$$D_n(E) = \frac{1}{2\pi^2}\left(\frac{2m_e}{\hbar^2}\right)(E - E_c)^{1/2} \tag{2.45}$$

$$D_h(E) = \frac{1}{2\pi^2}\left(\frac{2m_h}{\hbar^2}\right)(E_v - E)^{1/2} \tag{2.46}$$

The Fermi-Dirac probability distribution for electrons $f_n(E)$ and holes $f_h(E) = 1 - f_n(E)$ can be written as

$$f_n(E) = \frac{1}{1 + \exp\left(\frac{E - E_{fn}}{kT}\right)} \tag{2.47}$$

$$f_h(E) = \frac{1}{1 + \exp\left(\frac{E_{fh} - E}{kT}\right)} \tag{2.48}$$

2.6 Carrier Concentration in the Quantum Well in Steady State

In quantum well, the carrier concentration exhibits the effects of confinement. The electrons and holes concentration in the quantum well is given by [54]

$$n_{QW}(x) = \frac{m_e^* k_B T}{\pi \hbar^2} \sum_m |\psi_{e,m}|^2 \ln \left[1 + \exp\left(\frac{E_{fn} - E_{e,m}}{k_B T} \right) \right] \tag{2.49}$$

$$p_{QW}(x) = \frac{m_h^* k_B T}{\pi \hbar^2} \sum_m |\psi_{h,m}|^2 \ln \left[1 + \exp\left(\frac{-E_{h,m} - E_{fh} - E_g}{k_B T} \right) \right] \tag{2.50}$$

where, $\psi_{e(h),m}$ is the m^{th} wavefunction, $E_{e(h),m}$ is the corresponding eigen energy and $E_{fn(h)}$ is the quasi fermi level for electrons and holes, respectively.

CHAPTER 3

TRANSPORT AND MATERIAL PROPERTIES OF III-NITRIDES

Accurate device modeling needs understanding of various material phenomenon and intricate knowledge of its internal physical mechanisms, which are still not completely understood in case of III-Nitride based semiconductor materials. Simulation of these devices require comprehensive knowledge of a number of material parameters and their variation with internal and external physical conditions. In this chapter, we provide analytical models for transport parameters (mobility and diffusion coefficients), polarization (spontaneous and piezoelectric) and recombination processes.

3.1 Transport Properties

In case of GaN and its relevant alloys like AlN and InN, transport parameters like mobility, drift velocity and diffusion coefficient are dependent on a number of factors like lattice temperature, doping concentration and electric field. In this section, we discuss the effect of these factors and provide numerical models for transport parameters, which are used in drift-diffusion model. The models are discussed in detail below.

3.1.1 Field Dependent Mobility Model for Electrons

The drift velocity of electrons in III-N semiconductor materials depends on doping concentration, Lattice temperature and the applied electric field. Numerical models for the electron mobility in III-N semiconductors are developed based on experimental data and Monte Carlo simulations [55, 56, 57, 58]. The model for electron mobility used in this thesis is taken from [59]. The expression used in drift-diffusion equation for low field electron mobility is given as

$$\mu_0(T,N) = \mu_{min}\left(\frac{T}{300}\right)^{\beta_1} + \frac{(\mu_{max}-\mu_{min})\left(\frac{T}{300}\right)^{\beta_2}}{1+\left[\dfrac{N}{N_{ref}\left(\frac{T}{300}\right)^{\beta_3}}\right]^{\alpha\left(\frac{T}{300}\right)^{\beta_4}}} \tag{3.1}$$

In (3.1), N is the doping concentration, T is the temperature and α, β_1, β_2, β_3, β_4, μ_{min}, μ_{max} and N_{ref} are the fitting parameters given in Table

3.1.

Table 3.1: Parameters for low field electron mobility at reference density, $N_{ref} = 10^{17} cm^{-3}$ [59].

	$\boldsymbol{\mu_{min}}$ $(cm^2/V.s)$	$\boldsymbol{\mu_{max}}$ $(cm^2/V.s)$	$\boldsymbol{\alpha}$	$\boldsymbol{\beta_1}$	$\boldsymbol{\beta_2}$	$\boldsymbol{\beta_3}$	$\boldsymbol{\beta_4}$
InN	774.0	3138.4	0.68	-6.39	-1.81	8.05	-0.94
GaN	295.0	1460.7	0.66	-1.02	-3.84	3.02	0.81
AlN	297.8	683.8	1.16	-1.82	-3.43	3.78	0.86

The high field mobility for III-nitride materials is given by

$$\mu_e(E) = \frac{\mu_0(T,N) + v_{e,sat}\dfrac{E^{n_1-1}}{E_c^{n_1}}}{1 + a\left(\dfrac{E}{E_c}\right)^{n_2} + \left(\dfrac{E}{E_c}\right)^{n_1}} \tag{3.2}$$

where $\mu_0(T,N)$ is the electron temperature and doping dependent low field mobility as given in (3.1). $v_{e,sat}$ is the saturation velocity and E_c is the critical field. a, n_1 and n_2 are the fitting parameters given in Table 3.2

Table 3.2: Parameters for high field electron mobility[59].

	$\boldsymbol{v_{e,sat}}$ $(10^7 cm/s)$	$\boldsymbol{E_c}$ (kV/cm)	$\boldsymbol{n_1}$	$\boldsymbol{n_2}$	$\boldsymbol{a}$
InN	1.3595	52.4242	3.8501	0.6078	2.2623
GaN	1.9064	220.8936	7.2044	0.7857	6.1973
AlN	2.1670	447.0339	17.3681	0.8554	8.7253

Field dependent mobility and drift velocity for GaN, AlN and InN as a function of electric field are shown in Fig. 3.1. As can be seen from Fig. 3.1b, drift velocity reaches a maximum at $230kV/m$, $60kV/cm$ and $480kV/cm$ for GaN, InN and AlN respectively.

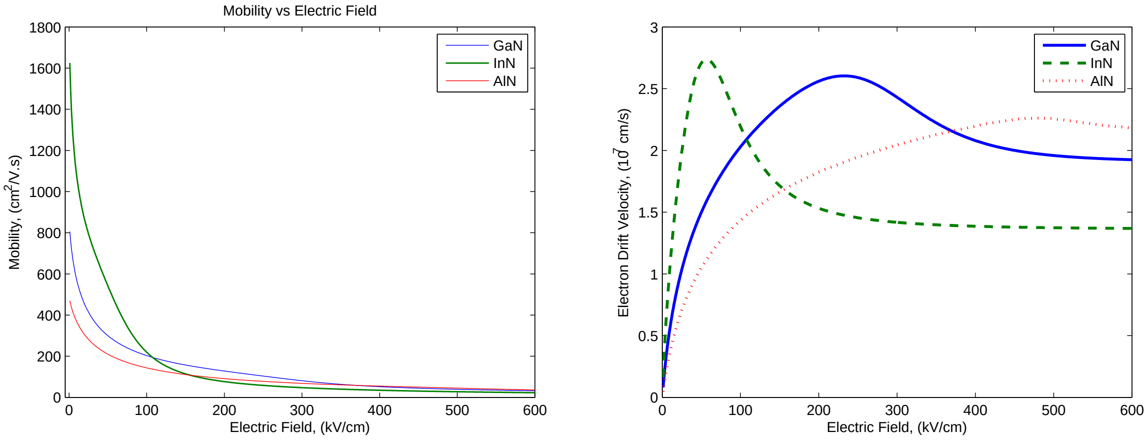

(a) (b)

Figure 3.1: Transport Parameters for GaN, InN and AlN. (a) Electron Mobility (b) Electron Drift Velocity. For this calculation lattice temperature $T = 300$ and $N_{ref} = 10^{17}cm^{-3}$.

3.1.2 Field Dependent Mobility Model for Holes

The analytical expression for high field mobility is derived from the standard Caughey-Thomas formula [60] for drift velocity as given by

$$\mu_h(E) = \frac{\mu_{h0}}{\left[1 + \left(\frac{\mu_{h0}E}{v_{h,sat}}\right)^{\beta}\right]^{1/\beta}} \tag{3.3}$$

where $v_{h,sat}$ is the hole saturation velocity, μ_{h0} is the lattice temperature and doping dependent mobility and β is the fitting parameter. Values of these parameters for GaN, InN and AlN are given in Table 3.3. Electric field dependent hole mobility and drift velocity for GaN, InN and AlN is shown in Fig. 3.2.

Table 3.3: Fitting parameters used in (3.3) for calculation of hole mobility in GaN, InN and AlN. These parameters are valid for lattice temperature of 300 K and electric field less than 800 kV/cm [61].

	$\boldsymbol{u_{h0}}$ $(cm^2/V.s)$	$\boldsymbol{v_{h,sat}}$ $(10^7 cm/s)$	$\boldsymbol{\beta}$
InN	35	1.5	0.75
GaN	70	1.7	0.725
AlN	70	1.25	1.9

The temperature and doping dependent mobility, $\mu_{h0}(T, N)$ is given by the expression

$$\mu_{h0}(T, N) = \frac{\mu_d}{1 + \left(\frac{N_i}{N_0}\right)^{A^*}} \tag{3.4}$$

where

$$N_i = N_a + N_d \tag{3.5}$$

$$\mu_d = A_d \left(\frac{T}{T_0}\right)^{\alpha_d} \tag{3.6}$$

$$N_0 = A_N \left(\frac{T}{T_0}\right)^{\alpha_N} \tag{3.7}$$

$$A^* = A_a \left(\frac{T}{T_0}\right)^{\alpha_a} \tag{3.8}$$

The values of the constant in (3.5)-(3.8) are given in Table 3.4.

Table 3.4: Fitting parameters for calculating temperature and doping dependent low field hole mobility in (3.4).

	$\boldsymbol{A_d}$ $(cm^2/V.s)$	$\boldsymbol{\alpha_d}$	$\boldsymbol{A_N}$ $(1/cm^3)$	$\boldsymbol{\alpha_N}$	$\boldsymbol{A_\alpha}$	$\boldsymbol{\alpha_a}$
GaN	41.7	-2.34	1.97×10^{19}	0.869	0.309	-2.311

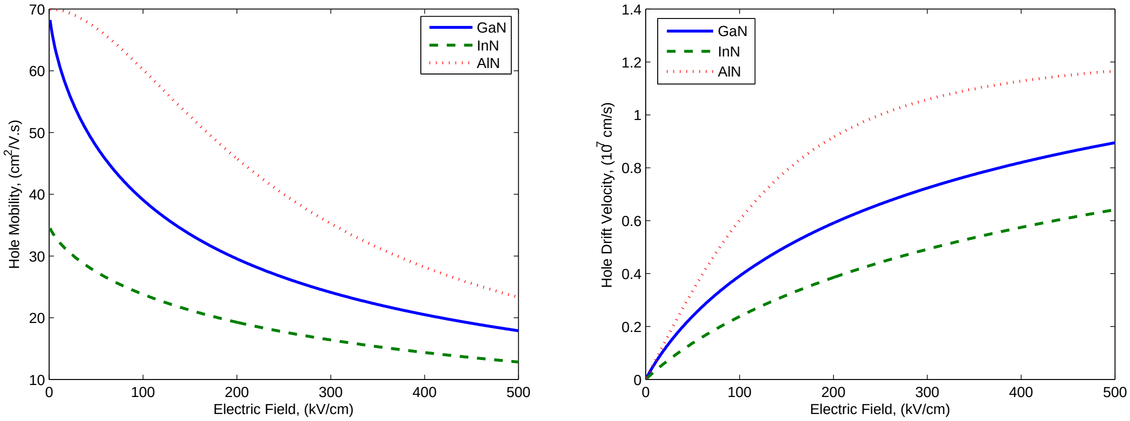

(a) (b)

Figure 3.2: Transport Parameters for GaN, InN and AlN. (a) Hole Mobility (b) Hole Drift Velocity. For this calculation lattice temperature $T = 300$ and doping, $N = 10^{17} cm^{-3}$.

3.1.3 Field Dependent Model for Diffusion Coefficient

Diffusion coefficient, D_n is an important parameter in the model of semiconductor material. The widely used diffusion coefficient is derived from the Einstein equation given by

$$D_n = \frac{K_b T}{q_e} \times \mu(E) \tag{3.9}$$

where, K_b is the Boltzmann Constant, T is lattice temperature and $\mu(E)$ is electric field dependent mobility. Fig. 3.3 shows Diffusion coefficient for electrons plotted as a function of electric field using Einstein equation.

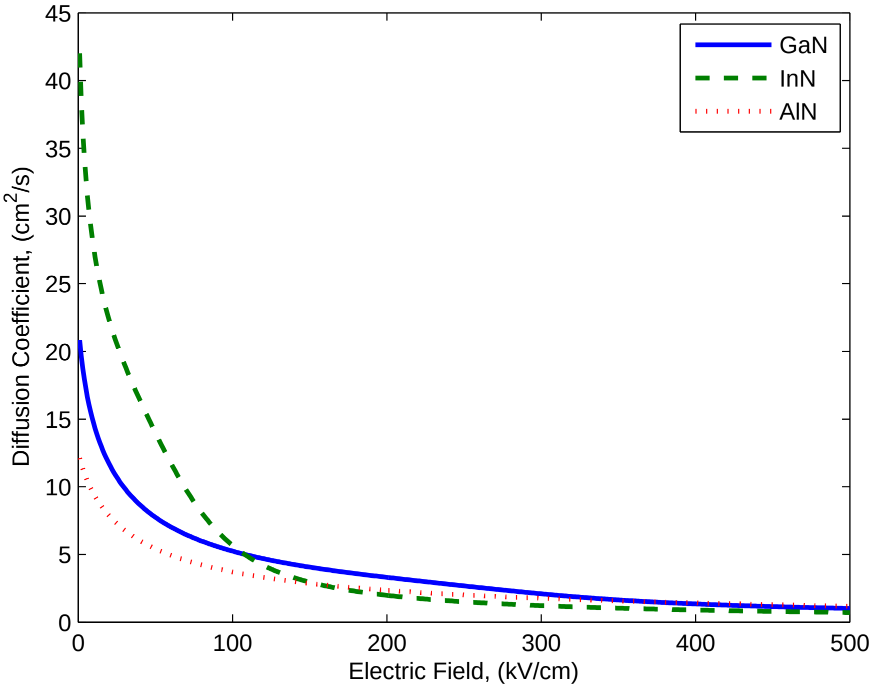

Figure 3.3: Electric field dependent electron diffusion coefficient for GaN, InN and AlN at temperature, T = 300 K and doping $N = 1 \times 10^{17} cm^{-3}$ using Einstein equation.

Einstein equation holds only at low electric field (when Boltzmann distribution is satisfied) [62]. Also, recent experiments have shown anisotropic characteristics for transport parameters in GaN [63, 64]. The diffusion coefficient in $\Gamma - A$ direction (c-direction) is larger than that in $\Gamma - M$ direction (basal plane) [65]. Electron diffusion coefficient for GaN is calculated in [65] using an ensemble Monte Carlo (EMS) method. For this thesis, the diffusion coefficient (in cm^2/s) along c -axis is expressed in a peace-wise polynomial function of electric field (in kV/cm)

using curve fitting as shown in (3.10).

$$D_n^{\Gamma-A}(E) = \begin{cases} P_1E^7 + P_2E^6 + P_3E^5 + P_4E^4 + \cdots & \\ \quad P_5E^3 + P_6E^2 + P_7E + P_8 & E < 500\ kV/cm \\ \quad 4.3 & E > 500\ kV/cm \end{cases} \tag{3.10}$$

Similarly, diffusion coefficient along $\Gamma - M$ direction (basal plane) is given by

$$D_n^{\Gamma-M}(E) = \begin{cases} P_1E^5 + P_2E^4 + P_3E^3 + \cdots & \\ \quad P_4E^2 + P_5E + P_6 & E < 200\ kV/cm \\ P_7E^5 + P_8E^4 + P_9E^3 + \cdots & \\ \quad P_{10}E^2 + P_{11}E + P_{12} & 200\ kV/cm < E < 500\ kV/cm \\ \quad 3.78 & E > 500\ kV/cm \end{cases} \tag{3.11}$$

The values of constant $P_1 - P_{12}$ in (3.10) and (3.11) are given in Table 3.5. Fig. 3.4 shows the field dependent diffusion coefficient (curve-fitted) obtained from (3.10) and (3.11) as well as the reference value [65]. Diffusion coefficient obtained from Einstein relation is also plotted for comparison.

Diffusion coefficient for holes is obtained using the Einstein equation (3.9). Fig. 3.5 shows the diffusion coefficient for holes as a function of electric field. As can be seen from Fig. 3.5, diffusion coefficient for GaN, InN and AlN decreases with increasing electric field.

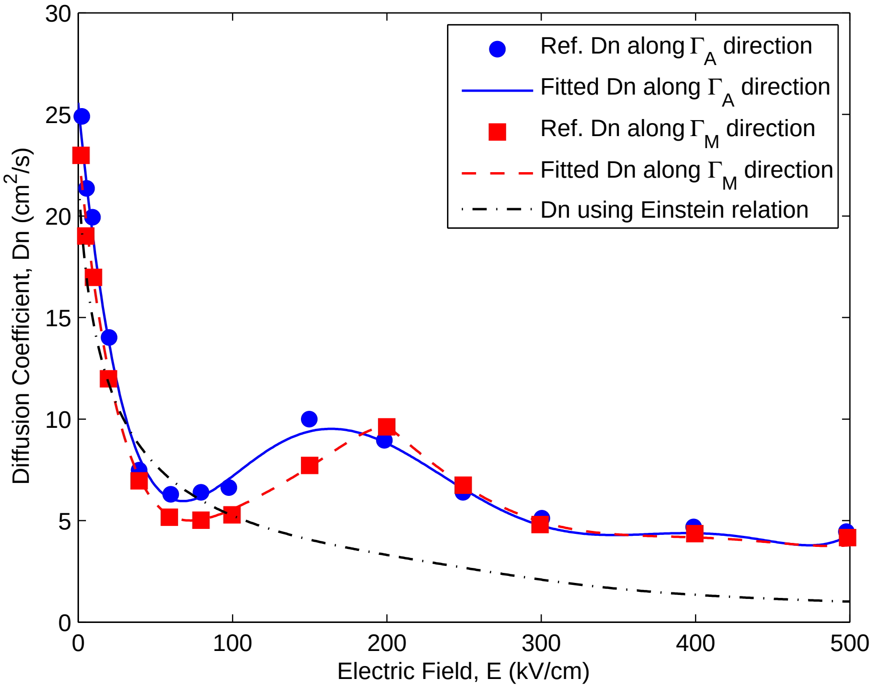

Figure 3.4: Electric field dependent electron diffusion coefficient for GaN at temperature, T = 300 K and doping $N = 1 \times 10^{17} cm^{-3}$.

3.2 Polarization

The polarization fields in III-N nitrides semiconductors are comprised of two components: The spontaneous polarization determined by material composition and piezoelectric polarization which arises due to strain in the material [66, 67]. The influence of crystal polarity on polarization in nitride heterostructures is very important. Fig. 3.6 shows the schematic diagram for wurtzite crystal structure. Due to the lack of inversion symmetry in the (0001) plane, there are two possible polarities of (0001) epitaxial growth. The upper (0001) surface in Fig. 3.6a is called Ga face while the lower $(000\bar{1})$ surface is called N face. The spontaneous polarization in GaN, InN and AlN is in $[000\bar{1}]$ direction (from Ga face to N face).

Table 3.5: Fitting parameters for calculating electric field dependent diffusion coefficient for GaN at temperature, T = 300 K and doping level $1 \times 10^{17} cm^{-3}$.

	Γ_A *Direction*	Γ_M *Direction*
P_1	-9.026×10^{-17}	-5.298×10^{-10}
P_2	3.352×10^{-13}	3.475×10^{-7}
P_3	-4.162×10^{-10}	-9.091×10^{-5}
P_4	2.445×10^{-7}	1.199×10^{-2}
P_5	-7.438×10^{-5}	-7.624×10^{-1}
P_6	1.146×10^{-2}	23.36×10^{0}
P_7	-7.922×10^{-1}	1.942×10^{-11}
P_8	25.57×10^{0}	-3.345×10^{-8}
P_9	$--$	2.196×10^{-5}
P_{10}	$--$	-6.703×10^{-3}
P_{11}	$--$	8.962×10^{-1}
P_{12}	$--$	-29.81×10^{0}

The piezoelectric polarization is such that for (0001) grown films, $\mathbf{P}_{pz}$ is in $[000\bar{1}]$ or [0001] direction for tensile or compressive strain, respectively [68].

High spontaneous and piezoelectric polarization and associated electrostatic charge densities influence carrier distributions, electric fields, and consequently a wide range of electronic and optical characteristics of III-N semiconductor materials and devices. Some of the these effects are summarized below

- Sheet charges at the quantum well interfaces induce very strong electric field, which reduces overlap of electron and hole wave functions resulting in smaller radiative recombination rate and a red shift in the emission spectrum. This effect is also known as Quantum Confined Stark Effect(QCSE) [69].

- Sheet charges at hetero-interfaces lead to significant reduction in carrier dwell time which results in low probability of carrier capture in the quantum well [70].

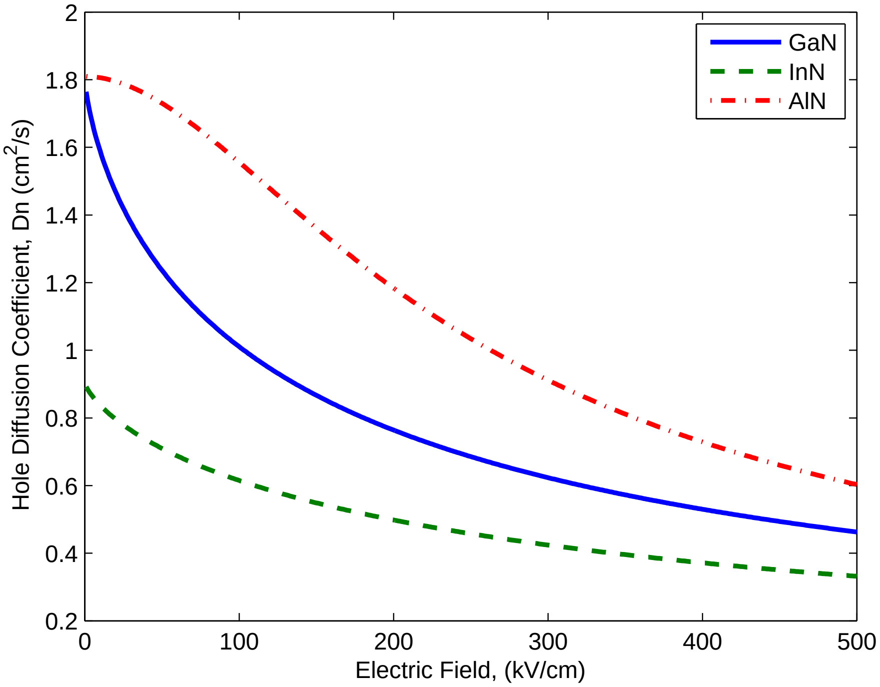

Figure 3.5: Electric field dependent hole diffusion coefficient for GaN, InN and AlN at temperature, T = 300 K and doping $N = 1 \times 10^{17} cm^{-3}$.

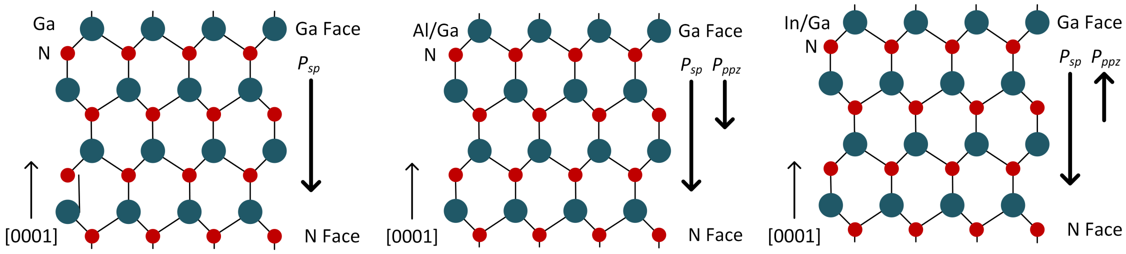

(a) (b) (c)

Figure 3.6: Crystal structure showing spontaneous polarization (P_{sp}) and piezoelectric polarization (P_{pz}) for (a) GaN, (b) $Al_xGa_{1-x}N$ and (c) $In_yGa_{1-y}N$ strained to GaN grown along [0001] axis.

- Due to spontaneous and piezoelectric polarization effects a positive sheet charge exists at the spacer/EBL interface. The resulting electric field in the spacer layer attracts electrons and drives them out of the active region toward the EBL, as a consequence reducing the barrier height of the EBL [71].

- Reducing electron leakage by increasing the Al concentration in the EBL is counteracted by the simultaneous increase in positive sheet charge at the spacer/EBL interface which further promotes electron extraction from the active region [72].

- Interface surface charges due to polarization in comressively strained $\mathrm{In}_x\mathrm{Ga}_{1-x}\mathrm{N}$ deposited on GaN can be used to lower the surface barrier, which results in a reduced turn-on voltage in InGaN/GaN field emitters [73].

The total polarization field **P**, which is the sum of piezoelectric and spontaneous polarization fields is related to polarization charge density, ρ_{pol} by [74].

$$\vec{\nabla} \cdot \mathbf{P} = \vec{\nabla} \cdot (\mathbf{P}_{sp} + \mathbf{P}_{pz}) = -\rho_{pol} \tag{3.12}$$

From (3.12) it is clear that at abrupt heterojucntion interface, a sheet charge density will be present due to the difference in spontaneous polarization and strain in the epitaxial layers. Fig. 3.7 shows the polarity of the polarization sheet charge density in the conduction band profile for GaN/InGaN QW interfaces and GaN/AlGaN EBL interface.

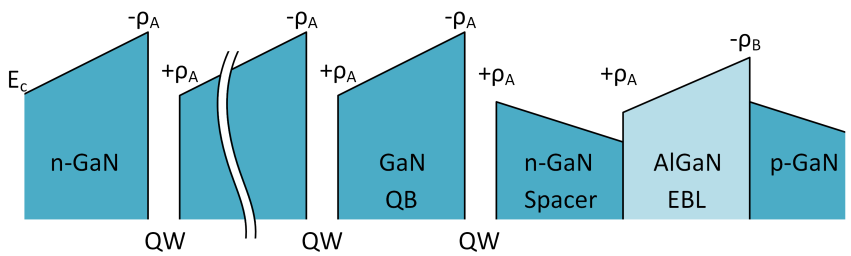

Figure 3.7: Illustration of polarization sheet charge density in the conduction band diagram for GaN/InGaN and GaN/AlGaN interfaces.

3.2.1 Spontaneous Polarization

Spontaneous polarization is by definition the built-in polarization field in free standing state of solid, in the absence of electric fields and surface charges at the boundary [75]. In III-Nitride semiconductors that have a hexagonal or wurtzite crystal structure, the center of electronic charges do not coincide with the nucleus position due to uneven bonding among the atoms leading to built-in electric field causing spontaneous polarization [66]. The spontaneous polarization of ternary nitride alloys,in C/m^2, can be expressed in terms of composition x as [76]

$$\mathrm{P}^{sp}_{Al_xGa_{1-x}N} = -0.090x - 0.034(1-x) + 0.019x(1-x) \tag{3.13}$$

$$\mathrm{P}^{sp}_{In_xGa_{1-x}N} = -0.042x - 0.034(1-x) + 0.038x(1-x) \tag{3.14}$$

$$\mathrm{P}^{sp}_{Al_xIn_{1-x}N} = -0.090x - 0.042(1-x) + 0.071x(1-x) \tag{3.15}$$

3.2.2 Piezoelectric Polarization

The piezoelectric polarization in III-Nitrides occurs at the hetero interfaces due to thermal strain, mechanical stress or lattice mismatch [77]. The peizoelectric polarization P_{pz} is obtained from the diagonal and shear components of the anisotropic atomistic strain fields. The linear dependence of piezoelectric polarization on strain tensor is given by [78]

$$\begin{bmatrix} \mathrm{P}_x \\ \mathrm{P}_y \\ \mathrm{P}_z \end{bmatrix} = \begin{bmatrix} 0 & 0 & 0 & 0 & e_{15} & 0 \\ 0 & 0 & 0 & e_{15} & 0 & 0 \\ e_{31} & e_{31} & e_{33} & 0 & 0 & 0 \end{bmatrix} \begin{bmatrix} \varepsilon_{xx} \\ \varepsilon_{yy} \\ \varepsilon_{zz} \\ \varepsilon_{xy} \\ \varepsilon_{xz} \\ \varepsilon_{yz} \end{bmatrix} \tag{3.16}$$

where e_{ij} are the piezoelectric constants and ε_{ij} are the components of the strain tensor given by

$$\varepsilon = \varepsilon_{xx} = \varepsilon_{yy} = \frac{a_{sub} - a(x)}{a(x)} \tag{3.17}$$

$$\varepsilon_{zz} = -2\varepsilon\frac{C_{13}}{C_{33}} \tag{3.18}$$

where $a(x)$ and a_{sub} are lattice constants of the unstrained alloy with composition x and of the substrate respectively. C_{ij} are the coefficients of the elastic stiffness tensor in Voigt notation [79]. Due to the symmetry of wurtzite crystals, Polarization has only a z-component along [0001] direction. The expression for piezoelectric polarization in (3.16) simplifies to

$$\mathrm{P}_{pz} = 2\varepsilon(e_{31} - e_{33}\frac{C_{13}}{C_{33}}) \tag{3.19}$$

The values of the coefficients used in (3.19) are given in Table 3.6. Piezoelectric polarization is in general a non-linear function of strain. The non-linearity becomes more prominent for large epitaxial strains. A model for second order piezoelectric polarization based on finite difference technique in conjunction with density functional perturbation theory (DFPT) within the local density approximation (LDA) is implemented in [80]. It was found that second order non-linearity in wurtzite crystals can lead to a correction of 15% in QWs and upto 40% for epitaxial QDs. The net piezoelectric polarization along [0001] direction in wurtzite crystals is given by

$$\mathrm{P}_{pz}^{net} = e_{31}(\varepsilon_{xx} + \varepsilon_{yy}) + e_{33}\varepsilon_{zz} + \frac{1}{4}(e_{311} + e_{312})(\varepsilon_{xx} + \varepsilon_{yy})^2 + \frac{1}{2}e_{333}\varepsilon_{zz}^2 + 2e_{313}\varepsilon_{xx}\varepsilon_{z}z \tag{3.20}$$

Piezoelectric polarization in III-Nitrides can be expressed compactly and accurately (in C/m^2) as

$$\mathrm{P}_{AlN}^{pz} = -1.808\varepsilon + 5.624\varepsilon^2 \qquad for \qquad \varepsilon < 0 \tag{3.21}$$

$$\mathrm{P}_{AlN}^{pz} = -1.808\varepsilon - 7.888\varepsilon^2 \qquad for \qquad \varepsilon > 0 \tag{3.22}$$

$$\mathrm{P}_{GaN}^{pz} = -0.918\varepsilon + 9.541\varepsilon^2 \tag{3.23}$$

$$\mathrm{P}_{InN}^{pz} = -1.373\varepsilon + 7.559\varepsilon^2 \tag{3.24}$$

where ε is the basal strain given by (3.17). For ternary alloys, piezoelectric polarization can be expressed as Vegard interpolation given by [81]

$$P_{X_xY_{1-x}N} = xP_{XN}[\varepsilon(x)] + (1-x)P_{YN}[\varepsilon(x)] \tag{3.25}$$

Lattice constant for ternary alloys as a function of concentration can be calculated as given by [76]

$$a_{\mathrm{Al}_x\mathrm{Ga}_{1-x}\mathrm{N}}(x) = 0.31986 - 0.00891x \tag{3.26}$$

$$a_{\mathrm{In}_x\mathrm{Ga}_{1-x}\mathrm{N}}(x) = 0.31986 + 0.03862x \tag{3.27}$$

$$a_{\mathrm{Al}_x\mathrm{In}_{1-x}\mathrm{N}}(x) = 0.35848 - 0.04753x \tag{3.28}$$

Table 3.6: Electro-mechanical properties of GaN, AlN and InN at room temperature [39].

Parameter	**Symbol**	**Unit**	**GaN**	**AlN**	**InN**
Stiffness Constant	C_{11}	GPa	375	395	225
Stiffness Constant	C_{12}	GPa	140	140	110
Stiffness Constant	C_{13}	GPa	115	105	95
Stiffness Constant	C_{33}	GPa	385	395	200
Stiffness Constant	C_{44}	GPa	120	100	45
Dielectric Constant	ϵ	$--$	8.9	8.5	15.3
Piezoelectric Constant	e_{33}	Cm^{-2}	0.65	1.55	0.43
Piezoelectric Constant	e_{31}	Cm^{-2}	-0.33	-0.58	-0.22
Piezoelectric Constant	e_{15}	Cm^{-2}	-0.33	-0.48	-0.22
Spontaneous Polarization	P_{sp}	Cm^{-2}	-0.029	-0.081	-0.032
In-plane Lattice Constant	a	A^o	3.188	3.112	3.540

As can be seen in Table 3.6, GaN has nearly the same spontaneous polarization as InN, but a large mismatch in lattice constant. On the contrary, AlN has a smaller lattice mismatch to GaN, but has spontaneous polarization about three times larger than GaN. So, in InGaN/GaN structure piezoelectric polarization is more dominant, while AlGaN/GaN structures are mostly influenced by spontaneous polarization.

3.3 Recombination

An electron-hole pair is generated when an electron jumps from the valence band to the conduction band. This process is called generation. The inverse of this process is termed as recombination. The recombination processes that occur inside III-Nitride based devices consist of both radiative and non-radiative recombination processes. The non-radiative recombination mechanisms include Shockley-Read-Hall (SRH) and Auger recombination processes. These processes are illustrated in Fig. 3.8 and discussed in detail below.

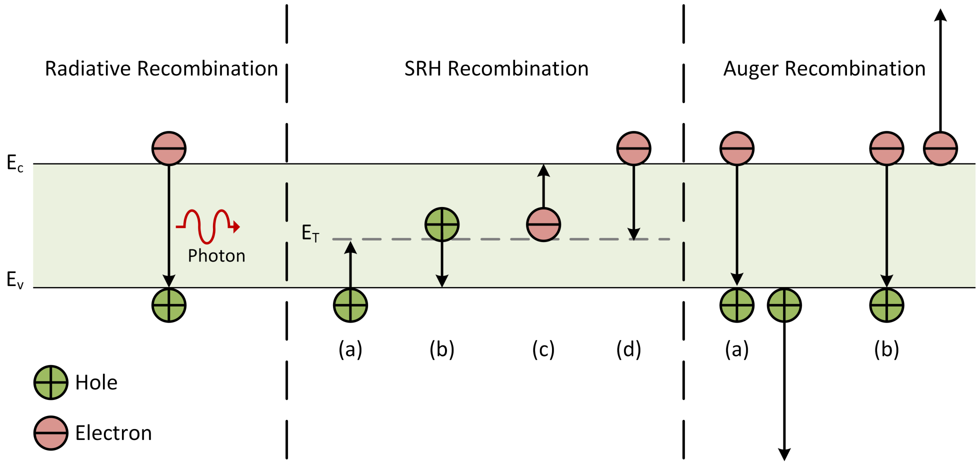

Figure 3.8: Basic Recombination mechanisms in GaN based LED. E_c and E_v are the conduction band and valence band edges and E_T is the trap level.

3.3.1 Radiative Recombination

In radiative recombination process, an electron from the conduction band combines with a hole in the valence band and releases a photon. The emitted photon has similar energy as the band-gap or less (phonon emission) and is therefore weakly absorbed. In direct band-gap materials radiative recombination is the dominant recombination mechanism. The total radiative recombination rate is proportional to the product of the occupied states (electrons) in the conduction band and the vacant states (holes) in the valence band given by

$$R_{rad} = B(np - n_i^2) \tag{3.29}$$

where B is the radiative recombination rate given in Table 3.7.

3.3.2 Shockley-Read-Hall (SRH) Recombination

Shockley-Read-Hall (SRH) model describes the recombination of holes and electrons in semiconductors through trapping mechanism. These traps are introduced due to dislocation or defects in the material. The presence of deep levels in the forbidden band caused by these impurities facilitates the SRH recombination process [82]. There are four different scenarios for SRH recombination process to occur as shown in Fig. 3.8. These processes are

(a) **Hole emission** - An electron jumps the valence band to the trapped level

(b) **Hole caputure** - An electron moves from an occupied trap to the valence band and hole disappears

(c) **Electron emission** - An electron jumps from the trapped level to the conduction band

(d) **Electron capture** - An electron moves from the conduction band to an unoccupied trap.

Threading dislocations form a number of acceptor like levels in GaN with energy E_d within the forbidden band gap [83]. So, the Schockley-Read approach [84] for non equilibrium carrier recombination through dislocation levels can be used. The SRH recombination rate can be expressed as [34]

$$R^{SRH} = \frac{np - n_i^2}{\tau_p(n + n_d) + \tau_n(p + p_d)} \tag{3.30}$$

where, n_i is the intrinsic carrier concentration, τ_n and τ_p are the life times of electrons and holes, respectively. The intrinsic carrier concentration can be found from

$$n_i = (N_c N_v)^{1/2} \exp\left(-\frac{Eg}{2kT}\right) \tag{3.31}$$

Here, N_c and N_v are the electron and holes density of states (DOS) in conduction and valence bands and E_g is the bandgap energy of the semiconductor given in Table 3.7. n_d and p_d in (3.30) are given by

$$n_d = N_c \exp\left(\frac{E_d - E_c}{kT}\right) \tag{3.32}$$

$$p_d = N_v \exp\left(\frac{E_v - E_d}{kT}\right) \tag{3.33}$$

The carrier life-time of electron and holes in (3.30) is given by

$$\tau_n = \frac{1}{4\pi D_n N_D}\left[\frac{2D_n}{aV_nS} - \frac{3}{2} - \ln(\pi a^2 N_D)\right] \tag{3.34}$$

$$\tau_p = \frac{1}{4\pi D_p N_D}\left[\frac{2D_p}{aV_pS} - \frac{3}{2} - \ln(\pi a^2 N_D)\right] \tag{3.35}$$

Here, $D_{n(p)}$ is the diffusion coefficient, N_d is the dislocation density, $S = 0.5$ is the fraction of electrically active sites on the a dislocation core and $V_{n(p)}$ is the thermal velocity of electrons (holes). $V_{n(p)}$ is given by

$$V_{n(p)} = \sqrt{\frac{3kT}{m^{av}_{n(p)}}} \quad , \quad m^{av}_{n(p)} = \left[m^{\perp}_{n(p)}(m^{z}_{n(p)})^{1/2}\right]^{2/3} \tag{3.36}$$

Fig. 3.9 shows the non-radiative carrier life time (τ_n and τ_p) as function of threading dislocation density and carrier mobility for $D_n = 2.6\ cm^2/s$ and $D_p = 0.12\ cm^2/s$ [85], thermal velocities $V_n = 2.6 \times 10^7\ cm/s$ and $V_p = 9.4 \times 10^6\ cm/s$ [86]. The horizontal line in Fig. 3.9a represents the radiative life time, $\tau_{rad} = 1/B\Delta n$ with $\delta n = 10^{18}\ cm^{-3}$. As can be seen from Fig. 3.9a, τ_{rad} becomes greater than non-radiative life time at $N_d \sim 10^7\ cm^{-2}$. For N_d greater than $\sim 10^7\ cm^{-2}$, the threading dislocation starts to affect the internal quantum efficiency (IQE) of the device. Fig. 3.9b shows the carrier life time plotted a function of mobility using 3.34. It is clear that by lowering the carrier mobility in the active region, the internal quantum efficiency can be improved.

3.3.3 Auger Recombination

Auger recombination is a three carrier process. There are two basic mechanism for Auger recombination process to take place as shown in Fig. 3.8.

(a) **Electron-Electron-Hole (EEH)** recombination process in which an electron hole pair recombination excites a second electron to a higher level in the conduction band, which then thermalizes back down to the conduction band

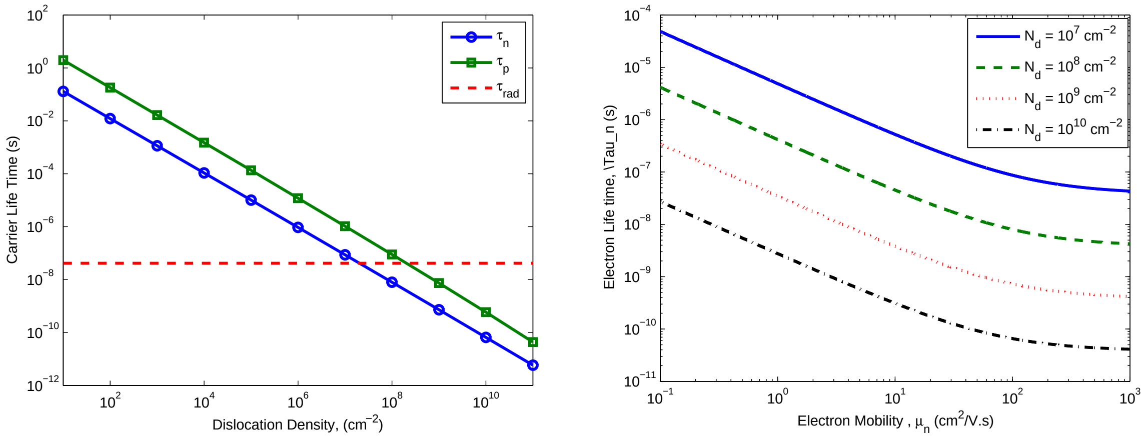

(a) (b)

Figure 3.9: Non radiative life times for electrons τ_n and holes τ_p as a function of (a) Threading Dislocation density (b) Electron Mobility μ_n.

edge.

(b) **Electron-Hole-Hole (EHH)** recombination process in which an electron hole pair recombination excites a hole to a lower level in the valence band.

Auger recombination is usually associated with decrease in quantum efficiency of GaN LEDs at high current density or efficiency droop [87, 88]. The expression for Auger recombination is given by

$$R_{Aug} = \Gamma_n n(np - n_i)^2 + \Gamma_p p(np - n_i)^2 \tag{3.37}$$

where, Γ_n and Γ_p are the Auger Recombination coefficient for electrons and holes, respectively. The value of Auger recombination coefficient for both electrons and holes is taken as 1.0×10^{-30} $cm^6 s^{-1}$ [89].

Table 3.7: Band parameters and impurity properties of GaN, AlN and InN at room temperature [39].

Parameter	**Symbol**	**Unit**	**GaN**	**AlN**	**InN**
Bandgap	E_g	eV	3.40	6.20	0.65
Electron affinity	χ	eV	10.23	7.64	11.1
In-plane electron mass	$m_n^{\perp}$	$--$	0.20	0.26	0.10
Normal electron mass	m_n^z	$--$	0.20	0.26	0.10
In-plane heavy hole mass	$m_{hh}^{\perp}$	$--$	1.65	2.58	1.45
Normal heavy hole mass	m_{hh}^z	$--$	1.10	1.95	1.35
In-plane light hole mass	$m_{lh}^{\perp}$	$--$	0.15	0.25	0.10
Normal light hole mass	m_{lh}^z	$--$	1.10	1.95	1.35
In-plane split-off hole mass	$m_{so}^{\perp}$	$--$	1.10	1.93	1.54
Normal split-off hole mass	m_{so}^z	$--$	0.15	0.23	0.09
Recombination Constant	B	$\times 10^{-11} cm^3 s^{-1}$	2.4	2.0	0.66
Effective electron DOS	N_c	$\times 10^{18} cm^{-3}$	2.234	6.2354	0.91452
Effective holes DOS	N_v	$\times 10^{19} cm^{-3}$	4.6246	48.844	5.1962

CHAPTER 4

THE Q-FDTD ALGORITHM

The proposed Quantum Finite Difference Time Domain (Q-FDTD) simulation model is presented in this chapter. This Q-FDTD model consists of solving Schrödinger equation coupled to the conventional Drift-Diffusion model in time domain. In this chapter, we discuss the leapfrog discretization scheme used for the discretization of Poisson, Schrödinger, drift-diffusion current and Continuity equations. We provide the discretized form of all the relevant equations. The simulation algorithm to implement the Q-FDTD solver is also discussed.

4.1 Overview of the Q-FDTD Scheme

The finite difference time domain (FDTD) is a robust numerical technique used to solve partial differential equations in time domain. This technique uses finite difference approximations to time and spacial derivatives. Finite difference approximation of the the first order is given by

$$\begin{aligned}\frac{\partial f(i,j)}{\partial x} &\approx \frac{f(i,j)-f(i-1,j)}{\Delta x}\\ \frac{\partial f(i,j)}{\partial y} &\approx \frac{f(i,j)-f(i,j-1)}{\Delta y}\end{aligned}\tag{4.1}$$

Similarly, finite difference approximation of the second order can be written as

$$\begin{aligned}\frac{\partial^2 f(i,j)}{\partial x^2} &\approx \frac{f(i+1,j)-2f(i,j)+f(i-1,j}{(\Delta x)^2}\\ \frac{\partial^2 f(i,j)}{\partial y^2} &\approx \frac{f(i,j+1)-2f(i,j)+f(i,j-1}{(\Delta y)^2}\end{aligned}\tag{4.2}$$

For the Q-FDTD method, we use the leapfrog scheme to discretize Poisson, Schródinger, drift-diffusion current and Continuity equations. In this scheme, electrostatic potential V, wave function ψ_{re} and ψ_{im} and electron and hole concentration n and p are placed at the exact grid points, while electric field E_x and E_y, and current densities J_{nx}, J_{ny}, J_{hx} and J_{hy} are placed at half grid points as shown in Fig. 4.1. Similarly, in time domain V, n, p, ψ_{re} are placed at integer time steps, while J_{nx}, J_{ny}, J_{hx}, J_{hy} and ψ_{im} are placed half a time step apart.

4.2 Numerical Solution of Poisson Equation

Poisson equation in (2.3) can be written in two dimensions as

$$\left(\frac{\partial}{\partial x}\hat{a}_x+\frac{\partial}{\partial y}\hat{a}_y\right)\cdot\left(\varepsilon_x(x,y)\frac{\partial V(x,y)}{\partial x}\hat{a}_x+\varepsilon_y(x,y)\frac{\partial V(x,y)}{\partial y}\hat{a}_y\right)=-\rho_t(x,y)\tag{4.3}$$

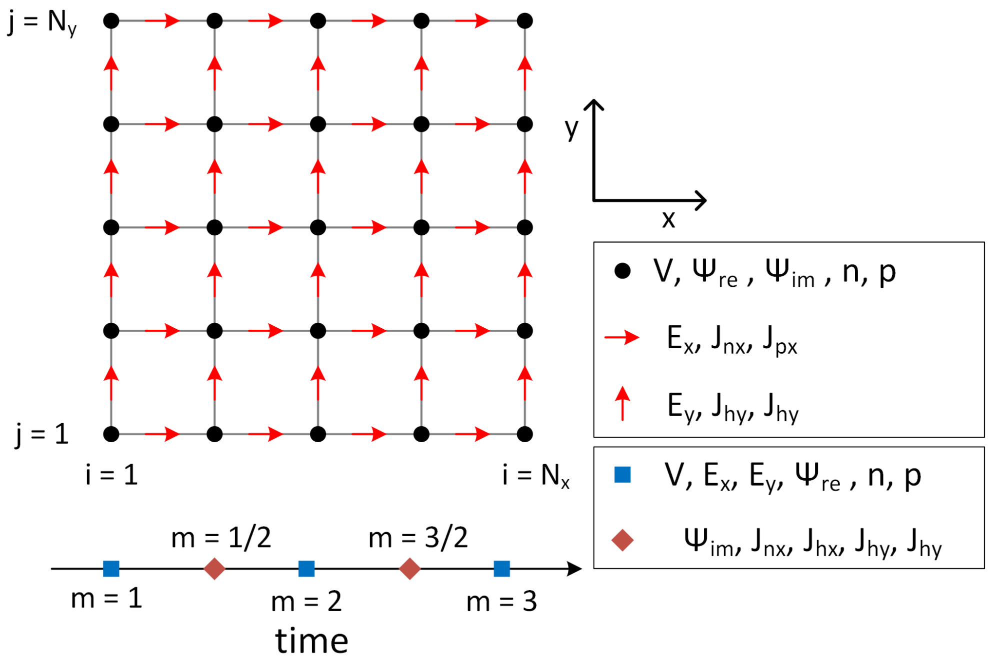

Figure 4.1: Illustrates the placement of variables and field quantities on the finite difference grid in time and space domain.

where, $\rho_t(x, y)$ is the net charge density given by

$$\rho_t(x, y) = \rho(x, y) + \left(\frac{\partial P_x^{tot}(x, y)}{\partial x} + \frac{\partial P_y^{tot}(x, y)}{\partial y} \right) \tag{4.4}$$

By using the chain rule for differentiation and dropping the argument (x, y), (4.3) can be written as

$$\varepsilon_x \frac{\partial V^2}{\partial x^2} + \frac{\partial \varepsilon_x}{\partial x}\frac{\partial V}{\partial x} + \varepsilon_y \frac{\partial V^2}{\partial y^2} + \frac{\partial \varepsilon_y}{\partial y}\frac{\partial V}{\partial y} = -\rho_t \tag{4.5}$$

4.2.1 Discretization

Equation (4.3) is discretized using (4.1) and (4.2) as shown below

$$\varepsilon_x(i,j)\frac{V(i+1,j)-2V(i,j)+V(i-1,j)}{\Delta x^2}+\frac{\varepsilon_x(i,j)-\varepsilon_x(i-1,j)}{\Delta x}\cdot\frac{V(i,j)-V(i-1,j)}{\Delta x}+$$
$$\varepsilon_y(i,j)\frac{V(i,j+1)-2V(i,j)+V(i,j-1)}{\Delta y^2}+\frac{\varepsilon_y(i,j)-\varepsilon_y(i,j-1)}{\Delta y}\cdot\frac{V(i,j)-V(i,j-1)}{\Delta y}$$
$$=-\rho_t(i,j) \tag{4.6}$$

Equation (4.6) is solved for electrostatic potential $V(i,j)$ as given by

$$\begin{aligned} V(i,j) = {} & C_1(i,j)\rho_t(i,j)+C_2(i,j)V(i+1,j)+C_3(i,j)V(i-1,j) \\ & +C_4(i,j)V(i,j+1)+C_5(i,j)V(i,j-1) \end{aligned} \tag{4.7}$$

where,

$$C_1(i,j)=\frac{\Delta x^2\Delta y^2}{\Delta y^2\big[\varepsilon_x(i,j)+\varepsilon_x(i-1,j)\big]+\Delta x^2\big[\varepsilon_y(i,j)+\varepsilon_y(i,j-1)\big]}$$
$$C_2(i,j)=\frac{\varepsilon_x(i,j)\Delta y^2}{\Delta y^2\big[\varepsilon_x(i,j)+\varepsilon_x(i-1,j)\big]+\Delta x^2\big[\varepsilon_y(i,j)+\varepsilon_y(i,j-1)\big]}$$
$$C_3(i,j)=\frac{\varepsilon_x(i-1,j)\Delta y^2}{\Delta y^2\big[\varepsilon_x(i,j)+\varepsilon_x(i-1,j)\big]+\Delta x^2\big[\varepsilon_y(i,j)+\varepsilon_y(i,j-1)\big]}$$
$$C_4(i,j)=\frac{\varepsilon_y(i,j)\Delta x^2}{\Delta y^2\big[\varepsilon_x(i,j)+\varepsilon_x(i-1,j)\big]+\Delta x^2\big[\varepsilon_y(i,j)+\varepsilon_y(i,j-1)\big]}$$
$$C_5(i,j)=\frac{\varepsilon_y(i-1,j)\Delta x^2}{\Delta y^2\big[\varepsilon_x(i,j)+\varepsilon_x(i-1,j)\big]+\Delta x^2\big[\varepsilon_y(i,j)+\varepsilon_y(i,j-1)\big]}$$

4.2.2 Successive Over Relexation (SOR) Method

Poisson equation in (4.7) is solved using Successive Over Relaxation method (SOR). Successive Over Relaxation method is an iterative method which moves slowly towards the solution. This method involves two kinds of errors

1. Errors that are introduced due to finite differences used in the discretization process
2. Errors caused by the SOR method, since the given solution never approaches the exact solution

In SOR method, the residue $R(i, j)$ is calculated from (4.7) using the recent values of potential V as given by

$$\begin{aligned} R(i,j) = C_1(i,j)\rho_t(i,j) + C_2(i,j)V(i+1,j) + C_3(i,j)V(i-1,j) \\ + C_4(i,j)V(i,j+1) + C_5(i,j)V(i,j-1) - V(i,j) \end{aligned} \tag{4.8}$$

Then a correction factor is added to the potential $V(i, j)$ at each iteration as shown below

$$V^k(i,j) = V^{k-1}(i,j) + \omega R^{k-1}(i,j) \tag{4.9}$$

Equation (4.8) and (4.9) are solved iteratively till convergence is achieved. Flowchart for the SOR method is shown in Fig. 4.2. The factor ω in (4.9) is called the relaxation parameter. For $\omega < 1$, the system is under relaxed and $\omega > 1$ produces over relaxation. The optimum value of the relaxation parameter for this case can

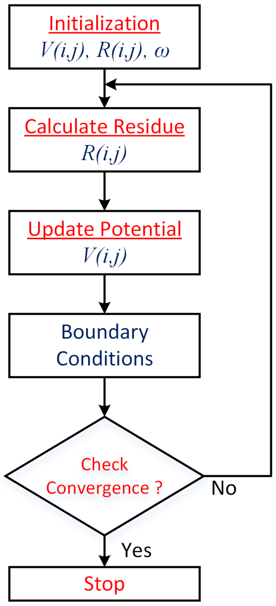

Figure 4.2: Flowchart illustrating the Successive Over Relaxation (SOR) method for solving Poisson equation.

be found from

$$\omega = 2\left[\cos\left(\frac{\pi}{N_x}\right) + \cos\left(\frac{\pi}{N_y}\right)\right] \quad , \quad 0 < \omega < 2 \tag{4.10}$$

where, N_x and N_y are the total grid points in x and y direction, respectively.

Convergence Criteria

The convergence criteria for SOR method is defined as

$$\sum_{i=1}^{N_x}\sum_{j=1}^{N_y}|R(i,j)| < Tol \tag{4.11}$$

Convergence is achieved when the residue $R(i,j)$ calculated in 4.8 is less than a preset tolerance value.

4.2.3 Boundary Conditions

Neuman boudary conditions are used at the boundaries of the simulation domain for potential V, which means that the gradient of the normal component of potential at the boundaries is zero

$$V(1,j) = V(2,j) \quad , \quad V(i_b,j) = V(i_b-1,j) \tag{4.12}$$

$$V(i,1) = V(2,j) \quad , \quad V(i,j_b) = V(i,j_b-1) \tag{4.13}$$

At the metal contacts, Dirchilet boundary conditions are used. A reference value of electrostatic potential is assigned to either the n or p contact, with the other being directly related to the external applied voltage V_{ext} and Built-in potential V_{bi} as [90]

$$V_p - V_n = V_{ext} - V_{bi} \tag{4.14}$$

where, V_p and V_n are the values of the potential assigned as Dirchilet Boundaries to the p and n electrode, respectively. In this thesis, we take the reference potential at the n-contact equal to zero. Thus the boundary conditions at the contacts can be written as

$$V_n = 0 \quad , \quad V_p = V_{ext} - V_{bi} \tag{4.15}$$

4.2.4 Stability

Discritization of drift-diffusion model imposes limitations on the the time step and mesh size of the grid as

1. The time step Δt is restricted by dielectric relaxation time τ_r.

2. The mesh size Δx is limited by the Debye length L_D.

Dielectric relaxation time is defined as the characteristic time for charge fluctuations to decay under the influence of the field that they produce. The dielectric relaxation time is calculated using

$$\tau_r = \frac{\varepsilon}{q_e N \mu} \tag{4.16}$$

where, ε is the dielectric constant, μ is the mobility and N is the doping concentration. For stability Δt must be smaller than the dielectric relaxation time, τ_r in the drift-diffusion model.

Debye length is defined as the distance in a semiconductor over which local electric fields affect distribution of free charge carriers. Debye Length is given by

$$L_D = \sqrt{\frac{\varepsilon k_B T}{q_e^2 N}} \tag{4.17}$$

Debye Length decreases with the doping concentration N. For GaN with $N \approx 10^{18}\ cm^{-3}$, Debye length is about 3.5 nm

4.3 Electric Field

Electric field vector can be found by the gradient of electrostatic potential as shown below.

$$\vec{E}(x,y) = -\left(\frac{\partial V(x,y)}{\partial x}\hat{a}_x + \frac{\partial V(x,y)}{\partial y}\hat{a}_y\right) \tag{4.18}$$

The discretized time update equations for electric field components along x and y directions are given by

$$E_x^m(i+1/2,j) = -\left(\frac{V^m(i+1,j) - V^m(i,j)}{\Delta x}\right) \tag{4.19}$$

$$E_y^m(i,j+1/2) = -\left(\frac{V^m(i,j+1) - V^m(i,j)}{\Delta y}\right) \tag{4.20}$$

4.4 Numerical Solution of Schrödinger Equation

The Schrödinger equation is solved in one dimension because the confinement in our structure is only along the c-axis. Schrödinger equation in (2.11) and (2.12) can be written for one dimensional problem as

$$\frac{\partial \psi_{re}(x,t)}{\partial t} = -\frac{\hbar}{2m}\frac{\partial^2 \psi_{im}(x,t)}{\partial x^2} + \frac{1}{\hbar}U(x)\psi_{im}(x,t) \tag{4.21}$$

$$\frac{\partial \psi_{im}(x,t)}{\partial t} = +\frac{\hbar}{2m}\frac{\partial^2 \psi_{re}(x,t)}{\partial x^2} - \frac{1}{\hbar}U(x)\psi_{re}(x,t) \tag{4.22}$$

4.4.1 Discretization

The real and imaginary components of wave function ψ in (4.21) and (4.22) are discretized both in space and time. In space, both real ψ_{re} and imaginary ψ_{im}

components of wavefunction are placed at the grid point. In time, the ψ_{im} is half a time step delayed than the ψ_{re}. Discretized equations for ψ_{re} and ψ_{im} are given by

$$\begin{aligned}\frac{\psi_{re}^{m+1}(i)-\psi_{re}^{m}(i)}{\Delta t} =& -\frac{\hbar}{2m}\frac{\psi_{im}^{m+1/2}(i+1)-2\psi_{im}^{m+1/2}(i)+\psi_{im}^{m+1/2}(i-1)}{(\Delta x)^2}\\ &+\frac{1}{\hbar}U(i)\psi_{im}^{m+1/2}(i)\end{aligned} \tag{4.23}$$

$$\begin{aligned}\frac{\psi_{im}^{m+3/2}(i)-\psi_{im}^{m+1/2}(i)}{\Delta t} =& +\frac{\hbar}{2m}\frac{\psi_{re}^{m+1}(i+1)-2\psi_{re}^{m+1}(i)+\psi_{re}^{m+1}(i-1)}{(\Delta x)^2}\\ &-\frac{1}{\hbar}U(i)\psi_{re}^{m+1}(i)\end{aligned} \tag{4.24}$$

After some algebraic manipulations, (4.23) can be written as

$$\begin{aligned}\psi_{re}^{m+1}(i) =& \psi_{re}^{m}(i)+\frac{\Delta t}{\hbar}U(i)\psi_{im}^{m+1/2}(i)\\ &-\frac{\hbar}{2m}\frac{\Delta t}{(\Delta x)^2}\left[\psi_{im}^{m+1/2}(i+1)-2\psi_{im}^{m+1/2}(i)+\psi_{im}^{m+1/2}(i-1)\right]\end{aligned} \tag{4.25}$$

Similarly, the equation for ψ_{im} is given by

$$\begin{aligned}\psi_{im}^{m+3/2}(i) =& \psi_{im}^{m+1/2}(i)+\frac{\Delta t}{\hbar}U(i)\psi_{re}^{m+1}(i)\\ &+\frac{\hbar}{2m}\frac{\Delta t}{(\Delta x)^2}\left[\psi_{re}^{m+1}(i+1)-2\psi_{re}^{m+1}(i)+\psi_{re}^{m+1}(i-1)\right]\end{aligned} \tag{4.26}$$

4.4.2 Stability Criteria

For stability of Schrödinger equation, the term ra is defined as [91].

$$ra \equiv min\left(\frac{\hbar}{2m}\frac{\Delta t}{(\Delta x)^2}, \frac{\Delta}{\hbar}U(i)\right) \tag{4.27}$$

The relation in (4.27) provides a general guideline for selecting mesh size Δx and time step Δt. To maintain stability, ra must not be greater than about 0.15.

4.4.3 Absorbing Boundaries

To prevent the outgoing waves from being reflected from the ends of the problem space, a perfectly matched layer (PML) is added along the confining direction at the outer boundaries of the simulation domain. To introduce the fictitious absorbing material at the boundaries as shown in Fig. 4.3, a stretching coordinate $\gamma(x)$ is added to the Schrödinger equation [92]

$$\frac{\partial\psi(x,t)}{\partial t} = i\frac{\hbar}{2m}\left(\gamma(x)\frac{\partial^2\psi(x,t)}{\partial x^2}\right) - i\frac{1}{\hbar}U(x)\psi(x,t) \tag{4.28}$$

The stretching coordinate $\gamma(x)$ is a complex function of distance written as

$$\gamma(x) = \left(\frac{1}{1+\mathrm{e}^{i\pi/4}\sigma(x)}\right) \tag{4.29}$$

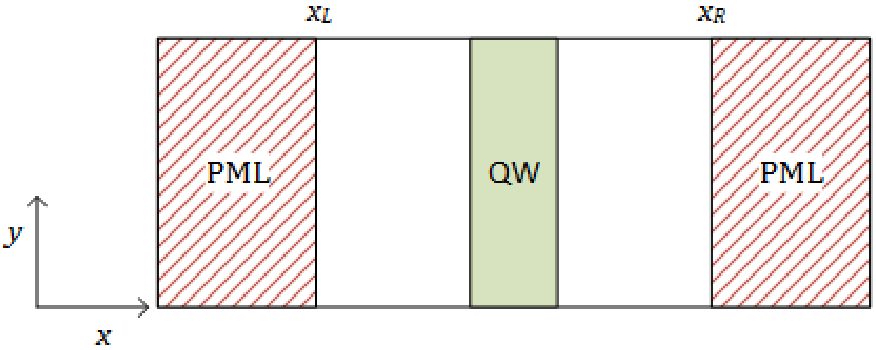

Figure 4.3: Schematic diagram for perfectly matched layer (PML) on the edges of the domain.

where, $\sigma(x)$ is given by

$$\sigma(x) = \begin{cases} 0.0005(x - x_L)^2 & x < x_L \\ 0 & x_L \le x \le x_R \\ 0.0005(x - x_R)^2 & x > x_R \end{cases} \tag{4.30}$$

Afer incorporating PML boundaries in Schrödinger equation, (4.25) and (4.26) can be written as

$$\Delta_{im} = \psi_{im}^{m+1/2}(i+1) - 2\psi_{im}^{m+1/2}(i) + \psi_{im}^{m+1/2}(i-1) \tag{4.31}$$

$$\psi_{re}^{m+1}(i) = \psi_{re}^{m}(i) + \frac{\Delta t}{\hbar}V(i)\psi_{im}^{m+1/2}(i) - \frac{\hbar\Delta t}{2m(\Delta x)^2}\Big[\gamma_{re}(i)\Delta_{im} + \gamma_{im}(i)\Delta_{re}\Big] \tag{4.32}$$

$$\Delta_{re} = \psi_{re}^{m+1}(i+1) - 2\psi_{re}^{m+1}(i) + \psi_{re}^{m+1}(i-1) \tag{4.33}$$

$$\psi_{im}^{m+3/2}(i) = \psi_{im}^{m+1/2}(i) - \frac{\Delta t}{\hbar}U(i)\psi_{re}^{m+1}(i) + \frac{\hbar\Delta t}{2m(\Delta x)^2}\Big[\gamma_{re}(i)\Delta_{re} - \gamma_{im}(i)\Delta_{im}\Big] \tag{4.34}$$

4.4.4 Eigen Energies and Eigen Functions

The procedure for finding the eigen energies and eigen functions using the simulation is given by [93].

1. To start the time domain solution, a test function ψ_{re} is initialized in the structure. This test function must be orthogonal to any previously determined eigen functions as shown in Fig. 4.4.

2. As the simulation proceeds time domain data is stored at a specific point (x_0, y_0).

3. At the end of the simulation, Fourier transform of the stored time domain data is taken to find the corresponding eigen energy.

4. To find the corresponding eigen function, repeat the simulation with the same test function and a running Fourier transform is taken at all the points in the simulation domain at the corresponding eigen frequency.

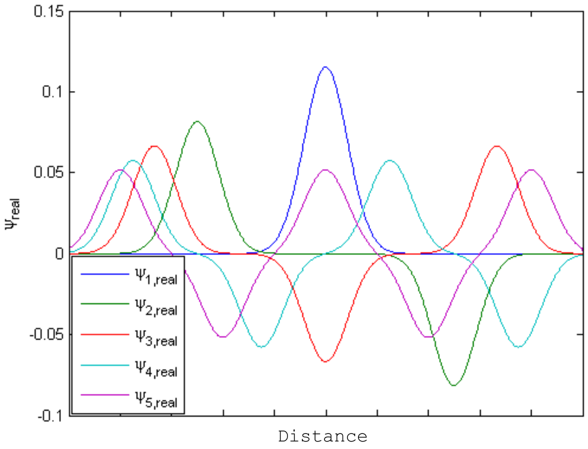

Figure 4.4: Sample initialization functions used for finding the first first 5 eigen energies and eigen functions.

4.5 Drift-Diffusion Current Equations

The drift-diffusion current equations for electrons and holes given in 2.19 and 2.20 can be written in vector form as

$$\vec{J}_n(x,y) = q_e\mu_n(x,y)n(x,y)\vec{E}(x,y) + q_eD_n(x,y)\left(\frac{\partial n(x,y)}{\partial x}\hat{a}_x + \frac{\partial n(x,y)}{\partial y}\hat{a}_y\right) \quad (4.35)$$

$$\vec{J}_h(x,y) = q_e\mu_h(x,y)p(x,y)\vec{E}(x,y) - q_eD_h(x,y)\left(\frac{\partial p(x,y)}{\partial x}\hat{a}_x + \frac{\partial p(x,y)}{\partial y}\hat{a}_y\right) \quad (4.36)$$

Here, $\vec{J}_n(x,y)$ and $\vec{J}_h(x,y)$ are vectors with components in x and y direction. Equation (4.35) and (4.36) are split into x and y components. These new scalar equations for electron current J_n can be written as

$$J_{n,x}(x,y) = q_e\mu_n(x,y)n(x,y)E_x(x,y) + q_eD_n(x,y)\frac{\partial n(x,y)}{\partial x} \quad (4.37)$$

$$J_{n,y}(x,y) = q_e\mu_n(x,y)n(x,y)E_y(x,y) + q_eD_n(x,y)\frac{\partial n(x,y)}{\partial y} \quad (4.38)$$

Separate equations for x and y components for hole current can be written in a similar fashion.

4.5.1 Discretization

Equations (4.37) and (4.38) are discretized using finite difference as shown below.

$$
\begin{aligned}
J_{n,x}^{m+1/2} &= \frac{q_e}{4}\left[\mu_n(i+1,j)\ +\mu_n(i,j)\ \right]\left[n^m(i+1,j)+n^m(i,j)\ \right]E_x^m(i,j) \\
&+\frac{q_e}{2}\left[D_n(i+1,j)+D_n(i,j)\right]\left[\frac{n^m(i+1,j)-n^m(i,j)}{\Delta x}\right] \qquad (4.39)\\
J_{n,y}^{m+1/2} &= \frac{q_e}{4}\left[\mu_n(i,j+1)\ +\mu_n(i,j)\ \right]\left[n^m(i,j+1)+n^m(i,j)\ \right]E_y^m(i,j) \\
&+\frac{q_e}{2}\left[D_n(i,j+1)+D_n(i,j)\right]\left[\frac{n^m(i,j+1)-n^m(i,j)}{\Delta y}\right] \qquad (4.40)
\end{aligned}
$$

Similarly, the final discretized version for hole current in x and y direction can be written as

$$
\begin{aligned}
J_{h,x}^{m+1/2} &= \frac{q_e}{4}\left[\mu_h(i+1,j)\ +\mu_h(i,j)\ \right]\left[p^m(i+1,j)+p^m(i,j)\ \right]E_x^m(i,j) \\
&-\frac{q_e}{2}\left[D_h(i+1,j)+D_h(i,j)\right]\left[\frac{p^m(i+1,j)-p^m(i,j)}{\Delta x}\right] \qquad (4.41)\\
J_{h,y}^{m+1/2} &= \frac{q_e}{4}\left[\mu_h(i,j+1)\ +\mu_h(i,j)\ \right]\left[p^m(i,j+1)+p^m(i,j)\ \right]E_y^m(i,j) \\
&-\frac{q_e}{2}\left[D_h(i,j+1)+D_h(i,j)\right]\left[\frac{p^m(i,j+1)-p^m(i,j)}{\Delta y}\right] \qquad (4.42)
\end{aligned}
$$

4.5.2 Boundary Conditions

At the boundaries between the quantum well and the bulk, thermionic emission boundary conditions given by (2.21) and (2.23) are used for electrons and holes, respectively.

4.6 Current Continuity Equations Bulk States

The current continuity equations for electrons and holes in (2.36) and (2.37) can be written as

$$\frac{\partial n(x,y)}{\partial t} = +\frac{1}{q_e}\left(\frac{\partial J_n(x,y)}{\partial x} + \frac{\partial J_n(x,y)}{\partial y} + J_{n,QW}^{3D}(x,y)\right) - R(x,y) \tag{4.43}$$

$$\frac{\partial p(x,y)}{\partial t} = -\frac{1}{q_e}\left(\frac{\partial J_h(x,y)}{\partial x} + \frac{\partial J_h(x,y)}{\partial y} + J_{h,QW}^{3D}(x,y)\right) - R(x,y) \tag{4.44}$$

4.6.1 Discretization

Equation (4.43) and (4.44) are discretized in time and space as shown below

$$\begin{aligned}\frac{n^{m+1}(i,j) - n^m(i,j)}{\Delta t} &= +\frac{1}{q_e}\Bigg(\frac{J_{n,x}^{m+1/2}(i+1/2,j) - J_{n,x}^{m+1/2}(i-1/2,j)}{\Delta x} \\ &\quad + \frac{J_{n,y}^{m+1/2}(i,j+1/2) - J_{n,y}^{m+1/2}(i,j-1/2)}{\Delta y} \\ &\quad + J_{n,QW}^{3D,m}(i,j)\Bigg) - R^m(i,j) \qquad (4.45) \\ \frac{p^{m+1}(i,j) - p^m(i,j)}{\Delta t} &= -\frac{1}{q_e}\Bigg(\frac{J_{h,x}^{m+1/2}(i+1/2,j) - J_{h,x}^{m+1/2}(i-1/2,j)}{\Delta x} \\ &\quad + \frac{J_{h,y}^{m+1/2}(i,j+1/2) - J_{h,y}^{m+1/2}(i,j-1/2)}{\Delta y} \\ &\quad + J_{h,QW}^{3D,m}(i,j)\Bigg) - R^m(i,j) \qquad (4.46)\end{aligned}$$

The final time update equations for electron and hole concentrations can be obtained from (4.45) and (4.46) as

$$\begin{aligned} n^{m+1}(i,j) = n^m(i,j) + \frac{\Delta t}{q_e}\Bigg(& \frac{J_{n,x}^{m+1/2}(i+1/2,j) - J_{n,x}^{m+1/2}(i-1/2,j)}{\Delta x} \\ & + \frac{J_{n,y}^{m+1/2}(i,j+1/2) - J_{n,y}^{m+1/2}(i,j-1/2)}{\Delta y} \\ & + J_{n,QW}^{3D,m}(i,j)\Bigg) - \Delta t R^m(i,j) \end{aligned} \tag{4.47}$$

$$\begin{aligned} p^{m+1}(i,j) = p^m(i,j) - \frac{\Delta t}{q_e}\Bigg(& \frac{J_{h,x}^{m+1/2}(i+1/2,j) - J_{h,x}^{m+1/2}(i-1/2,j)}{\Delta x} \\ & + \frac{J_{h,y}^{m+1/2}(i,j+1/2) - J_{h,y}^{m+1/2}(i,j-1/2)}{\Delta y} \\ & + J_{h,QW}^{3D,m}(i,j)\Bigg) - \Delta t R^m(i,j) \end{aligned} \tag{4.48}$$

4.6.2 Boundary Conditions

Neuman boudary conditions are used at the boundaries of the simulation domain for carrier concentration as given by

$$\nabla_\perp n = 0 \qquad , \qquad \nabla_\perp p = 0 \tag{4.49}$$

At the metal contacts, Dirchilet boundary conditions are used for n and p

$$n = N_D \qquad , \qquad p = N_A \tag{4.50}$$

4.6.3 Stability Criteria

For stability of the drift-diffusion model the time step Δt must be less than [94]

$$\Delta t < min\left(\frac{\Delta x^2 \Delta y^2}{2D\left(\Delta x^2 + \Delta y^2\right)}, \frac{2D}{v_\infty^2}\right) \tag{4.51}$$

where, D is diffusivity and v_∞ is the high field saturation velocity.

4.7 Current Continuity Equations Bound States

The current continuity equations for the bound states in quantum well as given in (2.39) and (2.40) can be written in discretized form as

$$n^m_{QW}(i,j) = n^{m-1}_{QW}(i,j) - \frac{\Delta t}{q_e} J^m_{n,QW}(i,j) + \Delta t \left(G^m_{n,QW}(i,j) - R^m_{n,QW}(i,j)\right) \tag{4.52}$$

$$p^m_{QW}(i,j) = p^{m-1}_{QW}(i,j) - \frac{\Delta t}{q_e} J^m_{h,QW}(i,j) + \Delta t \left(G^m_{h,QW}(i,j) - R^m_{h,QW}(i,j)\right) \tag{4.53}$$

where, $J_{n,QW}(i,j)$ and $J_{h,QW}(i,j)$ are the net capture or escape current for electrons and holes given by

$$J_{n,QW}(i,j) = J^{esc}_{n,QW}(i,j) + J^{cap}_{n,QW}(i,j) \tag{4.54}$$

$$J_{h,QW}(i,j) = J^{esc}_{h,QW}(i,j) + J^{cap}_{h,QW}(i,j) \tag{4.55}$$

The indexes i and j are defined only in the quantum well region.

4.8 The Q-FDTD Algorithm

The flow chart for Q-FDTD algorithm used in this thesis is shown in Fig. 4.5.

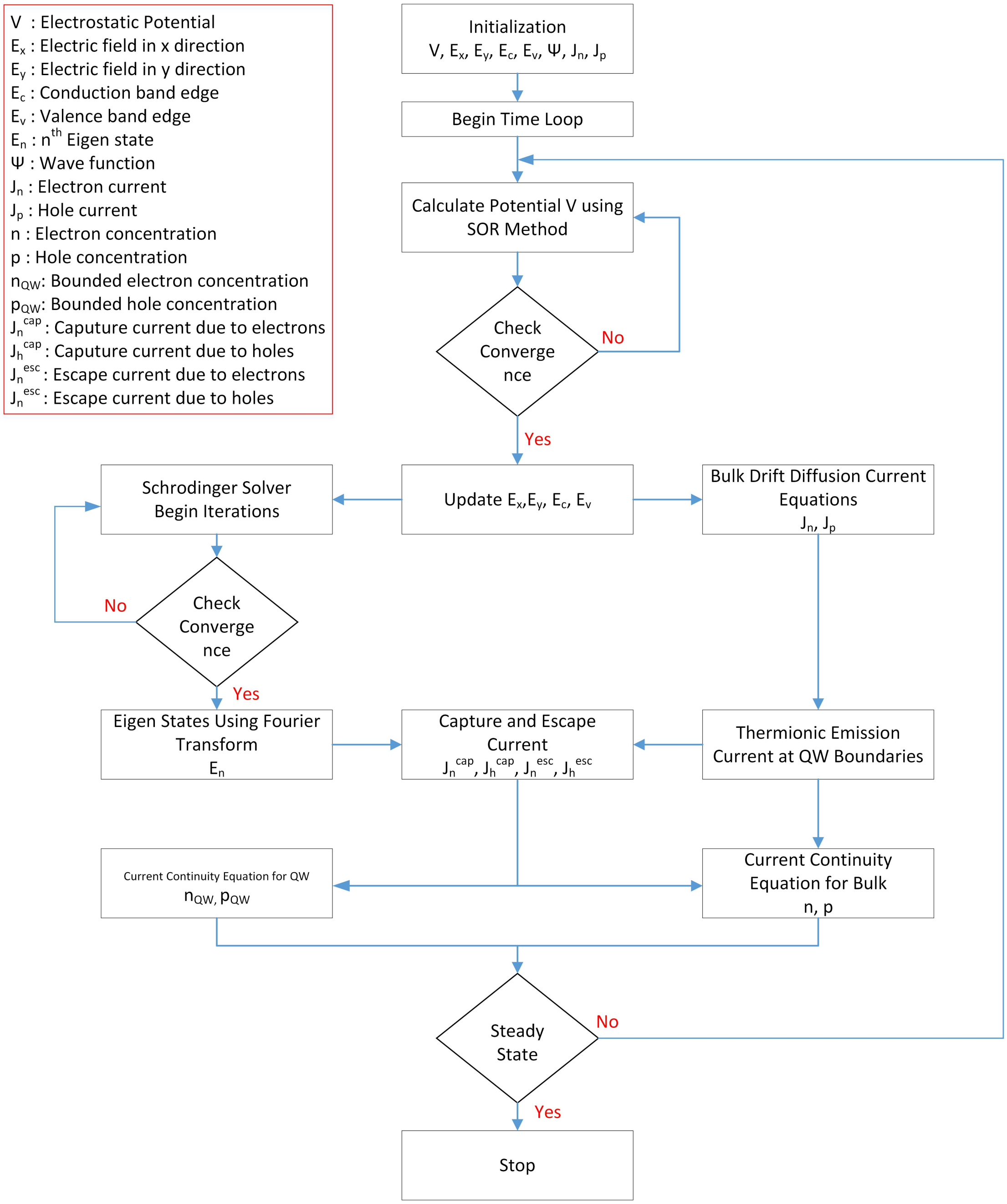

Figure 4.5: Flowchart illustrating the Q-FDTD algorithm used for the simulation of Quantum coupled Drift-Diffusion model.

CHAPTER 5

SIMULATION OF 1D GAN/INGAN SQW BASED LED

Simulation results for one-dimensional InGaN/GaN SQW LED structure are presented in this chapter. The 1D Q-FDTD solver is used to perform different parametric studies. Parametric studies about the effects of crystal polarity, QW thickness, Indium concentration in the well, the effects of electron blocking layer and asymmetric quantum well are performed.

5.1 Verification of the Drift-Diffusion Solver

The verification of 1D Drift-Diffusion solver is performed by simulating a simple GaN based p-n junction diode and comparing the analytical and simulated values of different parameters. Analytical expressions for p-n junction are

$$\text{Built in Potential} \ : \quad V_{bi} = \frac{k_B T}{q_e} \log\left(\frac{N_A N_D}{n_i^2}\right)$$

Width of depletion region :

$$W_p = \sqrt{\frac{2\varepsilon(V_{bi} - V_{app})N_D}{q_e N_A(N_A + N_D)}} \quad , \quad W_n = \sqrt{\frac{2\varepsilon(V_{bi} - V_{app})N_A}{(q_e N_D(N_A + N_D)}}$$

$$\text{Peak Electric Field :} \quad \vec{E}_p = \frac{-q_e N_A}{W_n}$$

The peak electric field calculated from the analytical expression is $-0.24690 \ MV/cm$ which is very close to the field calculated from the simulation as shown in Fig. 5.1.

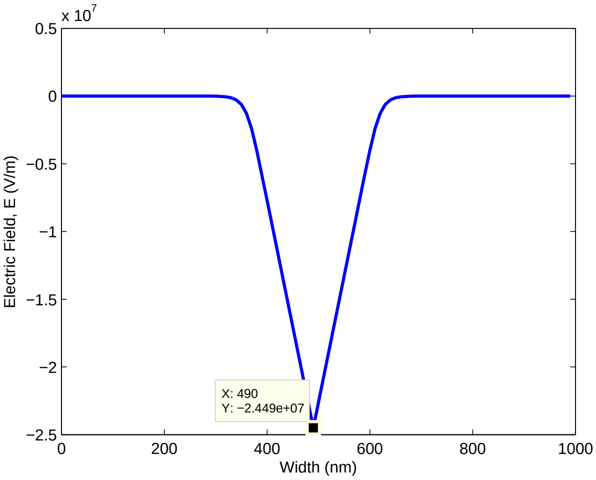

Figure 5.1: Electric field calculated by Drift Duffusion solver. As can be seen from the figure peak electric field is $-0.2449 \ MV/cm$

5.2 Verification of Schrödinger Equation Solver

Verification of Schrödinger solver is performed by comparing it with analytical solutions. Two different problems for which analytical solution is available are simulated with the Schrödinger solver.

5.2.1 Quantum Well with Inifinte Boundaries

An infinite one dimensional quantum well in vacuum with length, $L = 10\ nm$ is simulated with the Q-FDTD solver. The energy diagram of the 1D quantum well sturcture is shown in Fig. 5.2. $U(z)$ represents the potential energy of the system as a function of distance z

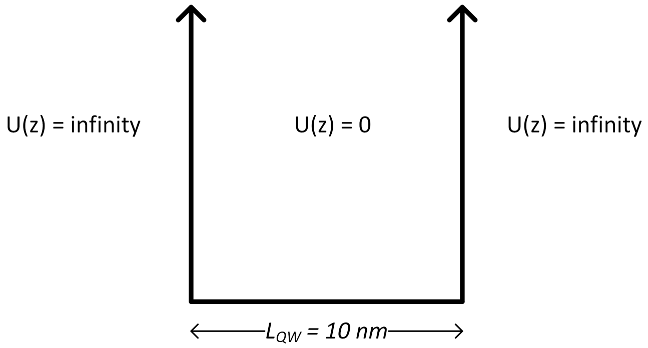

Figure 5.2: Schematic of potential energy profile for the infinite quantum well structure

Eigen energies for this system are given analytically by

$$E_n = \frac{\hbar^2\pi^2}{2m_eL^2}n^2 \qquad , \qquad n = 1, 2, 3\cdots \tag{5.1}$$

Table 5.1 shows the comparison of the first five eigen energies calculated by the Q-FDTD solver with the analytical values calculated using (5.1). The simulation results agree with analytical values with error of less than 0.55 percent.

Table 5.1: Comparison of analytical and simulated values of eigen energies for 10 *nm* infinite QW .

Level	Eigen Energy		Error	Units
	Analytical	Simulation		
E_1	3.76	3.78	0.02	meV
E_2	15.04	15.78	0.74	meV
E_3	33.84	35.34	1.5	meV
E_4	60.16	62.48	2.32	meV
E_5	94.01	97.19	3.18	meV

5.2.2 Quantum Well with Finite Boundaries

Next a finite one dimensional GaN/InGaN quantum well with length, $L = 5\ nm$ is simulated with the Schródinger solver. Material parameters for GaN and InGaN are taken from [95]. Schematic of the structure is shown in Fig. 5.3 below.

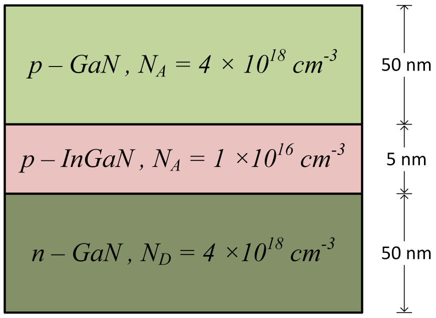

Figure 5.3: Schematic of the GaN/InGaN finite quantum well structure.

The potential energy profile of the system as shown in 5.4a is considered relative to the conduction band energy of the quantum well. We solve the system for eigen energies and eigen functions using the Schrödinger solver described in section 4.4.4. The corresponding eigen functions are shown in Fig. 5.4b.

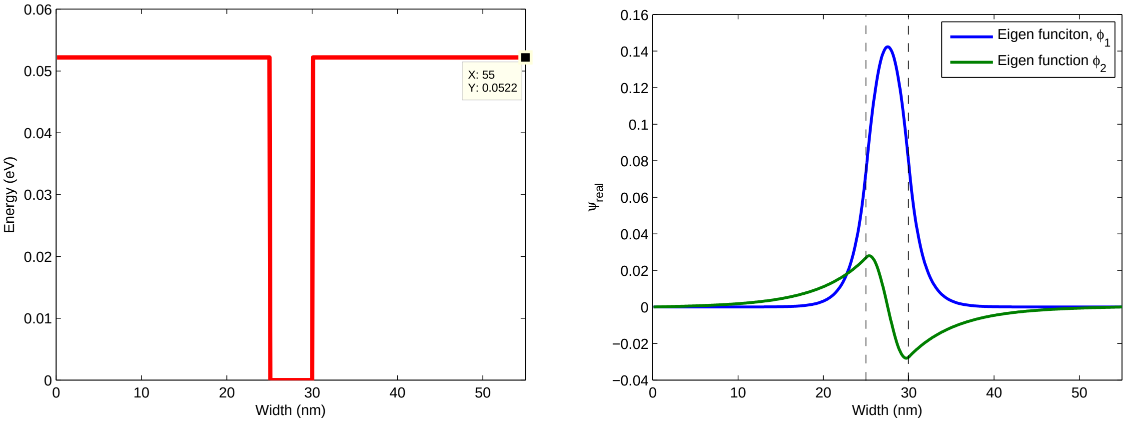

(a) (b)

Figure 5.4: GaN/InGaN structure. (a) Profile of the conduction band, (b) First two eigen functions Φ_n.

A comparison between the analytical and simulation results is shown in Table 5.2. The results from simulation agree well with the analytical values with error less than 0.75 percent

Table 5.2: Comparison of analytical and simulated values of eigen energies for 5 nm GaN/InGaN finite QW.

Level	Eigen Energy		Error	Units
	Analytical	Simulation		
E_1	15.1016	14.9875	0.1141	meV
E_2	49.2452	48.9065	0.3387	meV

5.3 Analysis of GaN/$In_{0.2}Ga_{0.8}N$/GaN SQW Structure

The device simulated in this sections consists of a 300 nm n-doped ($N_D = 5 \times 10^{17}\ cm^{-3}$) GaN layer, a 2 nm undoped GaN/$In_{0.2}Ga_{0.8}N$/GaN quantum well followed by a 300 nm p-doped ($1 \times 10^{18}\ cm^{-3}$) GaN layer. The total device dimension is 602 nm. The schematic of the device is shown in Fig. 5.5.

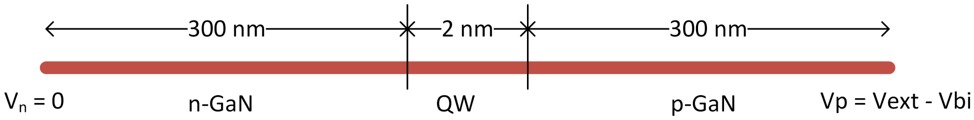

Figure 5.5: Schematic of GaN/$In_{0.2}Ga_{0.8}N$/GaN structure.

The FDTD simulation size is 2408 points with $\Delta x = 0.25\ nm$ and $\Delta t = 5.0 \times 10^{-18}\ s$. The device is biased at $V_p = V_{ext} - V_{bi}$ at p-contact and $V_n = 0$ at the n-contact. The material parameters used of this device are presented in Table 5.3.

Table 5.3: Parameters used in the simulation of GaN/$In_{0.2}Ga_{0.8}N$/GaN device.

Parameter Name	Value	Units
Carrier concentration in n-GaN layer	5×10^{17}	cm^{-3}
Carrier concentration in p-GaN layer	1×10^{18}	cm^{-3}
Bandgap of GaN	3.4	eV
Bandgap of $In_{0.2}Ga_{0.8}N$	2.85	eV
Relative dielectric constant of GaN	8.9	–
Relative dielectric constant of $In_{0.2}Ga_{0.8}N$	10.12	–
Low field electron mobility, μ_{n0}	1460	$cm^{-2}V^{-1}s^{-1}$
Low field hole mobility, μ_{h0}	30	$cm^{-2}V^{-1}s^{-1}$
Effective DOS of electrons in GaN, N_c	2.23×10^{18}	cm^{-3}
Effective DOS of holes in GaN, N_v	4.62×10^{19}	cm^{-3}
Effective DOS of electrons in $In_{0.2}Ga_{0.8}N$, N_c	1.97×10^{18}	cm^{-3}
Effective DOS of holes in $In_{0.2}Ga_{0.8}N$, N_v	4.74×10^{19}	cm^{-3}

The simulation is run for a total time of 100 *ps*. Electronic characteristics obtained for this device from the simulation are presented below.

5.3.1 I-V Curve and Electric Field

Fig. 5.6 shows the I-V characteristics of the GaN/$In_{0.2}Ga_{0.8}N$/GaN single quantum well device. The I-V curve is obtained from steady state values of injection current density and applied bias. The turn on voltage is 3.15 V. The injection current increases exponentially with the applied voltage. The built-in voltage of this structure is calculated as 3.26 V.

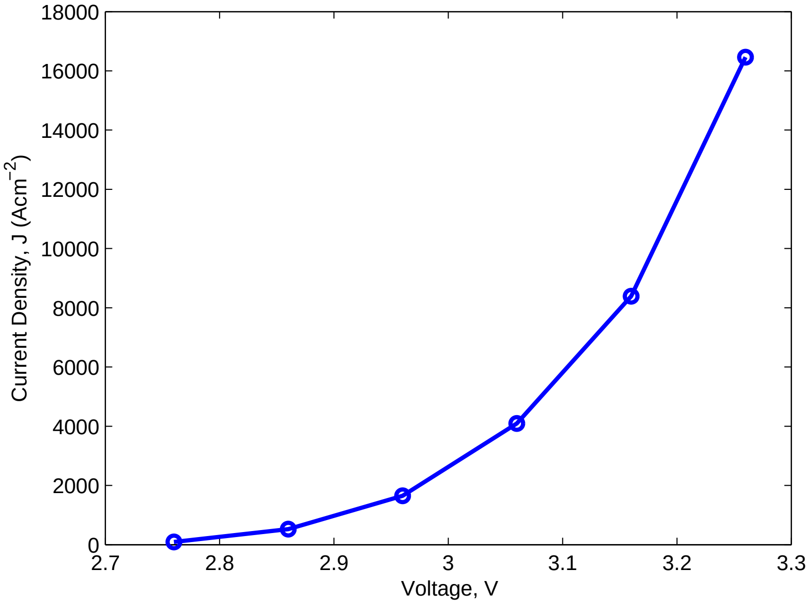

Figure 5.6: Current-Voltage (I-V) characteristics of GaN/In$_{0.2}$Ga$_{0.8}$N/GaN single QW structure.

The distribution of electric field for different injection current in the device is shown in Fig. 5.7. The electric field inside the quantum well is negative , while outside is positive. This can be explained by the fact that the $p-n$ junction field is oppositely directed to the polarization field induced in the quantum well.

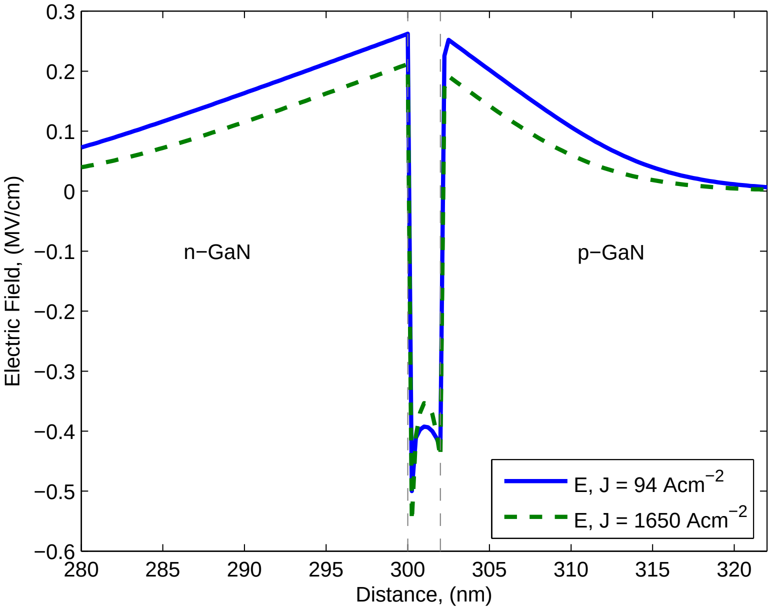

Figure 5.7: Electric field profile of GaN/In$_{0.2}$Ga$_{0.8}$N/GaN single QW structure.

Since the applied bias/current density changes the magnitude of $p-n$ junction field, the electric field across the device changes with the injection current. By increasing the injection current the $p-n$ junction field decreases which results in the decrease in the magnitude of electric field. The non-uniform electric field profile inside the quantum well is the result of partial screening with non-equilibrium carriers [39].

5.3.2 Band Diagrams and Partial Current Density

Conduction Band and valence band profile for the quantum well structure is obtained from the steady state electrostatic potential profile by

$$E_c = -q_e V + U_c \tag{5.2}$$

$$E_v = -q_e V + U_v \tag{5.3}$$

where, $U_{c(v)}$ is the band profile obtained from the electron affinity rule. The steady state band profile is shown in Fig. 5.8.

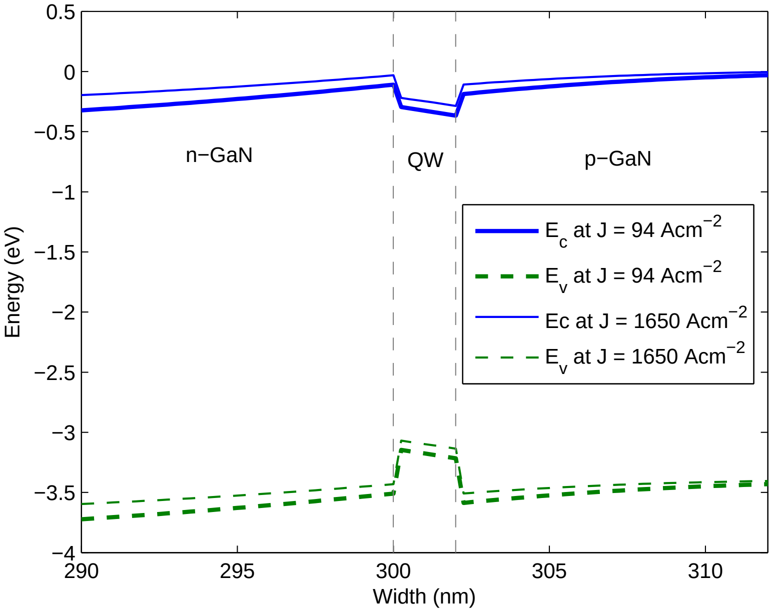

Figure 5.8: Conduction and valence band profile of GaN/In$_{0.2}$Ga$_{0.8}$N/GaN single QW structure at $J = 94\ Acm^{-2}$ and $J = 1650\ Acm^{-2}$ during steady state

The direction of the slope of band in the quantum well is decided by the sign of polarization charges at the quantum well interfaces, which is determined by the crystal polarity. The effects of crystal polarity on band diagram will be discussed in section 5.6.

The partial current density of electrons and holes in the structure is shown in Fig. 5.9. The current in n-GaN region is mainly due to electrons and in p-region is due to holes. The total current in the device is always the same. It is observed from the simulations, that steady state is achieved faster at high injection current density. This reduces the simulation time considerably.

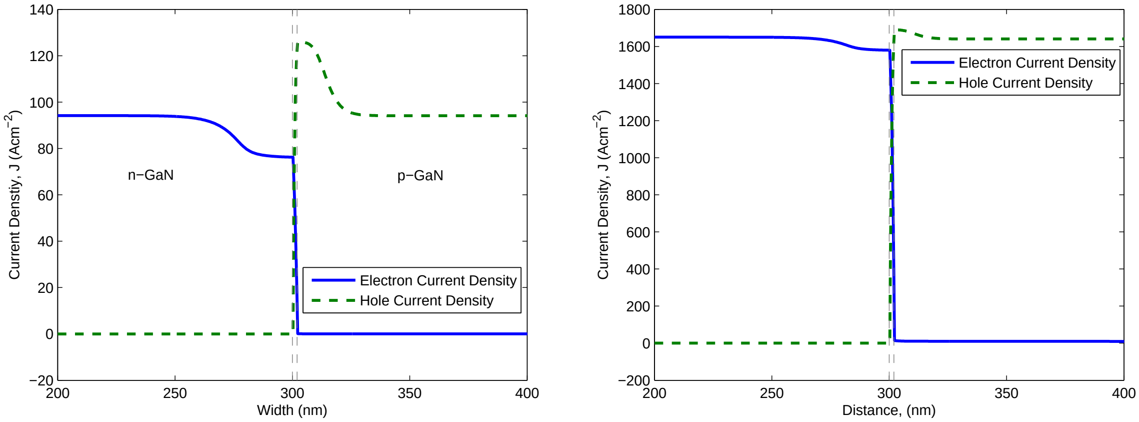

(a) (b)

Figure 5.9: Partial current density for GaN/In$_{0.2}$Ga$_{0.8}$N/GaN single QW structure. (a) $J = 94\ Acm^{-2}$, (b) $J = 1650\ Acm^{-2}$.

5.4 Eigen States and Emission Wavelength

The emission wavelength of the device is calculated from the difference between the first eigen state of electrons and holes as

$$\lambda = \frac{2\pi\hbar c}{q_e(E_{e,1} - E_{h,1})} \tag{5.4}$$

where, $E_{e,1}$ and $E_{h,1}$ are the first eigen states for electron and holes in electron volts (eV). The emission wavelength of the InGaN/GaN structure is calculated as 409.1737 nm.

5.5 Electron and Hole Wavefunction Overlap

The overlap of electron and hole wavefunction is one of the most important characteristic in designing of LED structure. It directly affects the radiative recombination rate and therefore the internal quantum efficiency. The electron and hole envelop function calculated from Schrödinger equation is shown in Fig. 5.10.

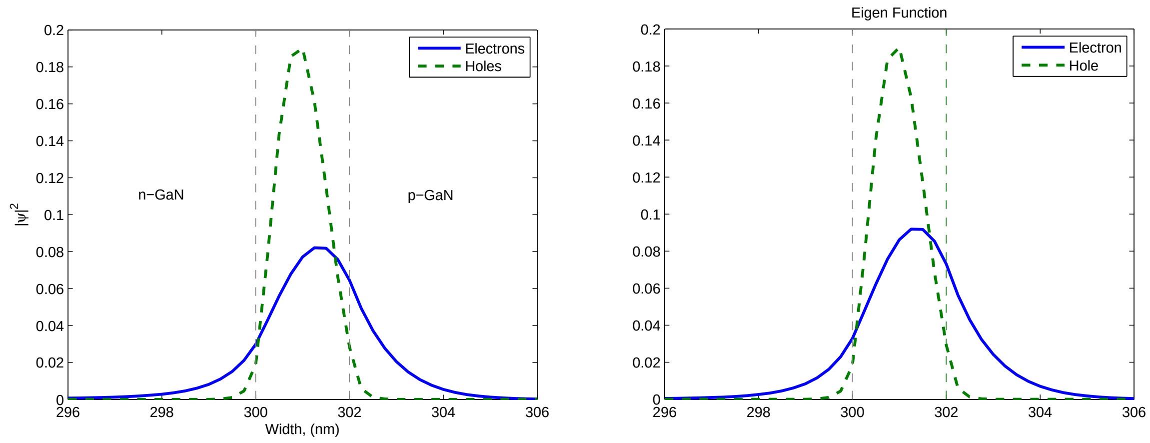

(a) At $J = 94\ Acm^{-2}$

(b) At $J = 1650\ Acm^{-2}$

Figure 5.10: Electron and hole wavefunction overlap

As shown in the figure above, the peak of the envelop function for electrons and holes are not aligned, this mismatch arises due to the polarization charges at the interfaces. The envelop function for electrons is tilted toward the p-GaN interface and the hole envelop function is shifted toward the n-GaN interface. The envelop function overlap can be increased by reducing the polarization charges at the interfaces of the quantum well. Also it can be seen from the figure, that the envelop function of the electron is broader than the envelop function of holes. This is due to the fact that the effective mass of the electron is much smaller than the effective mass of the hole. The shape of the envelop function is determined mainly by the effective mass of the carrier and the polarization charges at the interface. Injection current does not show any significant effect on electron and hole wavefunction overlap.

5.5.1 Carrier Concentration

Electron and hole concentration at two different injection current densities are shown in Fig. 5.11. The figure shows a non-uniform carrier concentration in the the quantum well. Holes tend to accumulate at the n-GaN interface and electrons accumulate at p-GaN interface of the quantum well. This phenomenon occurs due to the presence of polarization sheet charges at the interfaces of the quantum well. The well provides good carrier confinement. The total carrier concentration in the quantum well is of orders of magnitude higher than that in the contact layers. This is due to the super-injection effect in double heterostructures with a quantum well active region [39]. Electron concentration in the p-GaN region decays much slower than the decay of hole concentration in the n-GaN region because of higher electron mobility than hole mobility.

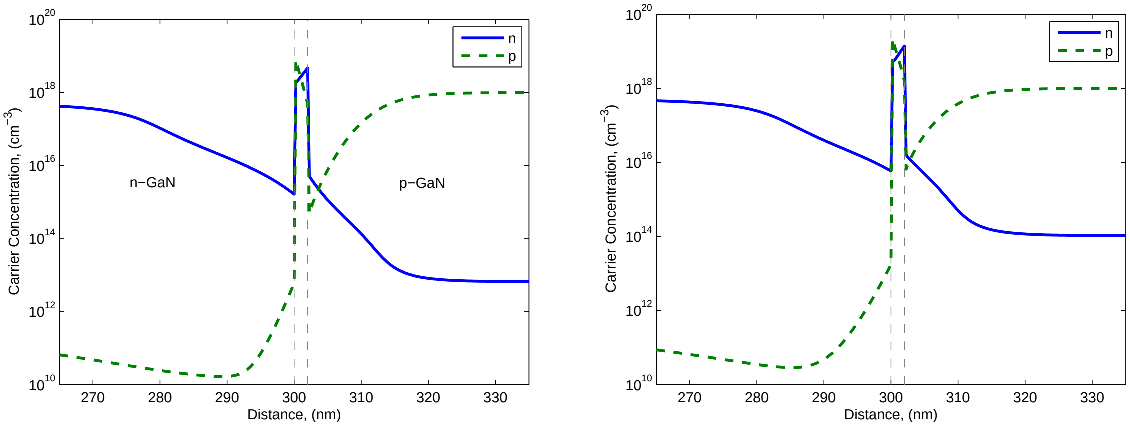

(a)

(b)

Figure 5.11: Carrier concentration for GaN/In$_{0.2}$Ga$_{0.8}$N/GaN single QW structure. (a) n and p at $J = 94\ Acm^{-2}$, (b) n and p at $J = 1650\ Acm^{-2}$.

The carrier concentration in the quantum well increases at high injection current. The peak electrons concentration in the QW at $J = 94\ Acm^{-2}$ is $4.7 \times 10^{18}\ cm^{-3}$ and is $1.38 \times 10^{19}\ cm^{-3}$ at $J = 1650\ Acm^{-2}$. Similarly, holes concentration increases from $7.89 \times 10^{18}\ cm^{-3}$ to $2.18 \times 10^{19}\ cm^{-3}$ with injection current of 94 and 1650 Acm^{-2}, respectively.

5.5.2 Recombination Rates and Internal Quantum Efficiency

Radiative recombination rate is shown in Fig. 5.12. The radiative recombination rate in the quantum well area is much higher as compared to the bulk region due to carrier confinement in the well region. The radiative recombination rate increases with increasing injection current both in the quantum well and the bulk region.

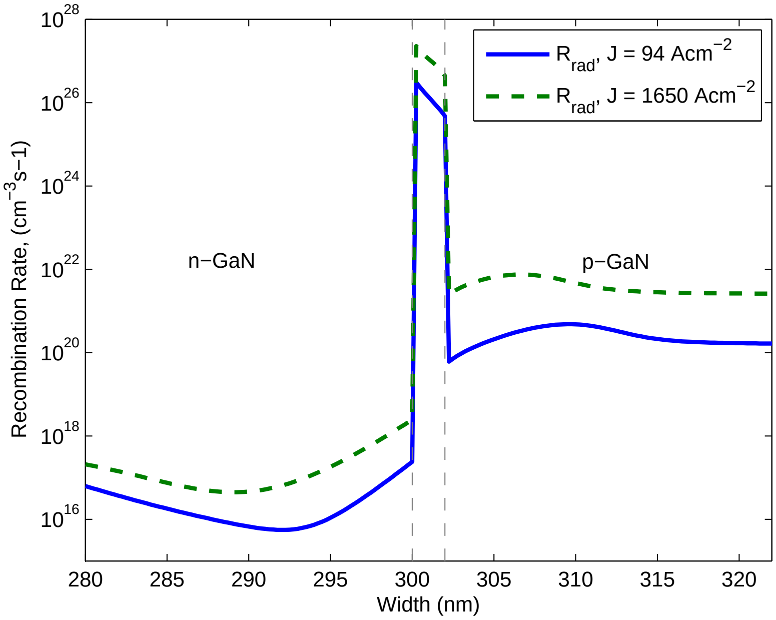

Figure 5.12: Radiative recombination rate at $J = 94\ Acm^{-2}$ and $J = 1650\ Acm^{-2}$ during steady state

Fig. 5.13 shows the non-radiative recombination rates of the device. Both SRH and Auger non-radiative recombiination processes are considered for this simulation. As can be seen from the figures below, at low injection current both SRH and Auger recombination rates are of the same order. As the current density increases, Auger recombination begins to dominate. At $J = 94\ Acm^{-2}$, the magnitudes of SRH and Auger recombination rate are 9.9×10^{25} and $7.2 \times 10^{25}\ cm^{-3}s^{-1}$, while at $J = 1650\ Acm^{-2}$ they increase to 2.7×10^{26} and $1.5 \times 10^{27}\ cm^{-3}s^{-1}$, respectively.

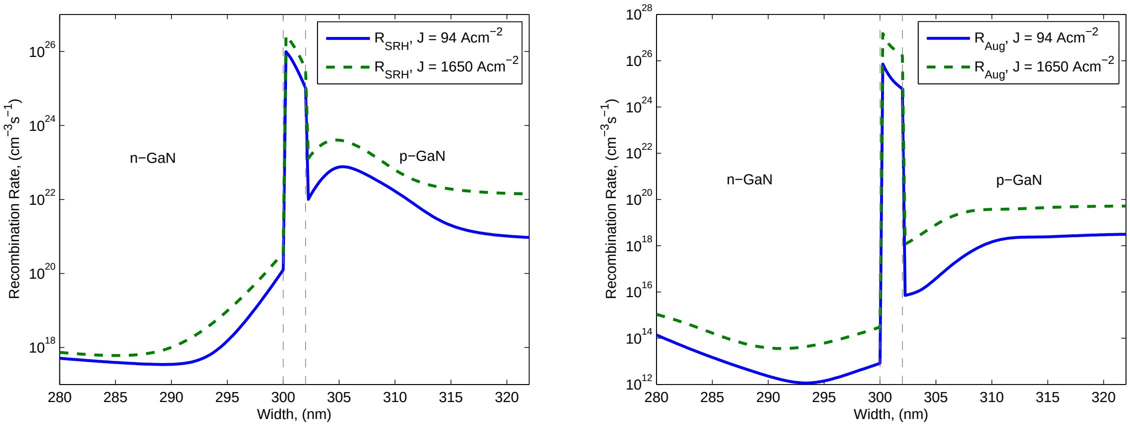

(a)

(b)

Figure 5.13: Non-radiative recombination processes. (a) SRH recombination rate, (b) Auger non-radiative recombination rate.

Internal quantum efficiency is determined by both the radiative and non-radiative mechanisms, which in turn are decided by the threading dislocation density (TDD), N_D. For our simulation we use a TDD of $10^8 cm^{-2}$. The calculated internal quantum efficiency of the device is shown in Fig. 5.14. As can be seen from the figure with SRH recombination only, IQE increases with injection current density and reaches almost unity of this level to TDD. With both SRH and Auger recombination cosidered, IQE reaches a peak at lower injection current and then starts to reduce sharply with injection current.

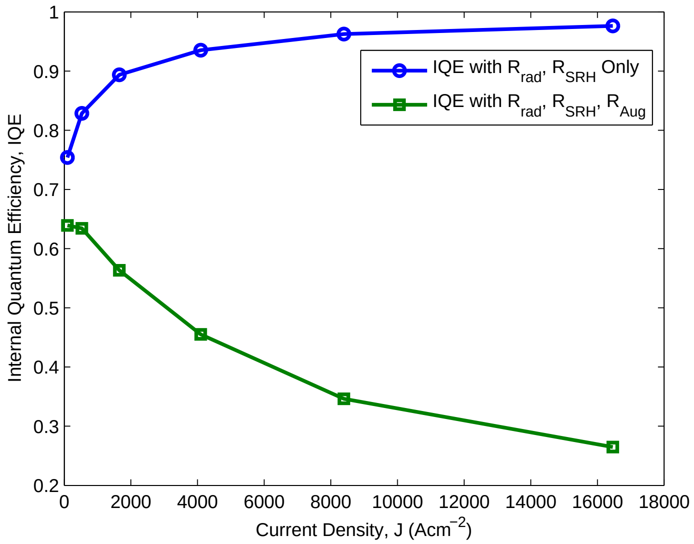

Figure 5.14: Internal Quantum efficiency at Dislocation density, $N_d = 10^8\ cm^{-2}$.

5.6 Polarity Effects

The charge distribution in the III-Nitride based LED heterostructure is largely determined by crystal polarity. The GaN crystal can be grown with either Ga or N-polarity. For Ga polarity the growth direction corresponds to the positive direction [0001] of the wurtzite crystal, while N-polarity corresponds to the negative $[000\bar{1}]$ direction.

To study the effects of polarity on the electronic properties, we simulate the device described in section 5.3 with both Ga and N polarity with same current density. The results for both Ga-polar and N-polar are shown side by side in Fig. 5.15 and Fig. 5.16 for comparison.

The band diagrams for both Ga and N polar device as shown in Figs. 5.15a and 5.15b suggests that N polar device offers higher potential barriers to electrons and holes as compared to Ga-polar. These barriers help in carrier confinement in the QW active region. The direction of the bands are reversed due to the reversal of polarization sheet charge densities at the QW interfaces. In case of Ga-polar structure, the polarization field is opposite to the p-n junction field while for N-polar structure the polarization field is always aligned with the p-n junction field. To illustrate this point, the partial current densities are shown in Fig. 5.15e and 5.15f for Ga-polar and N-polar structure, respectively. N polar structure has the same current density as Ga polar structure for smaller external bias.

The reversed polarization field in the N-polar structure also results in more overlap in the electron and hole envelop functions as shown in Figs. 5.15c and 5.15d. In case of Ga-polar structure the envelop functions are shifted in opposite directions. Also the envelop functions in Ga-polar structure are wider and spell into the bulk region, while in N-polar structure, they are more aligned on top of each other and confined to the QW.

The peak electron and holes concentration and recombination rates in the N-polar structure is also reversed. Due to opposite direction of electric field in the QW, holes accumulate at the p-interface while electrons accumulate at the n-interface of the QW in N-polar structure. These accumulated electrons and holes block extra carriers from entering into the active region and also attract the opposite carriers out of the quantum well. That is why despite deeper wells, N-polar structures have comparable carrier concentration and recombination rates to Ga-polar structure as shown in Fig. 5.16.

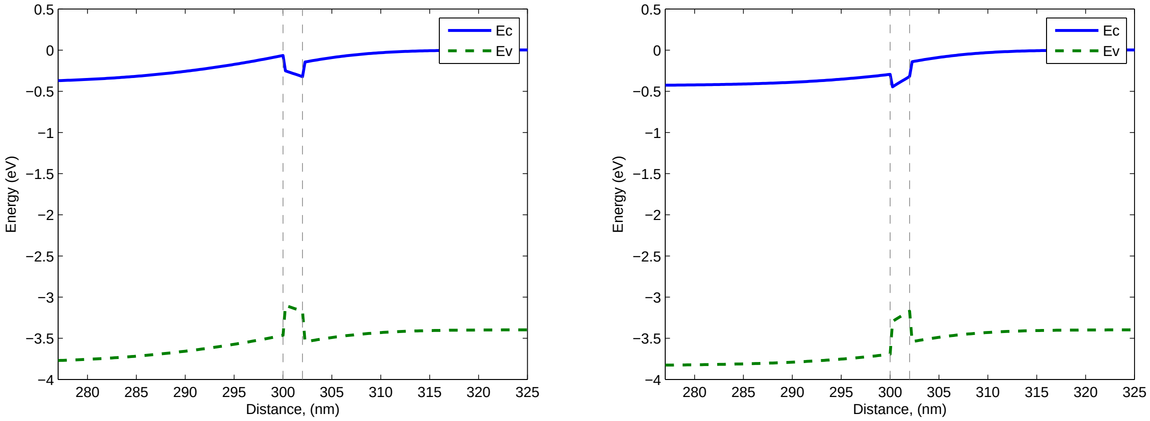

(a) Ga polar (b) N polar

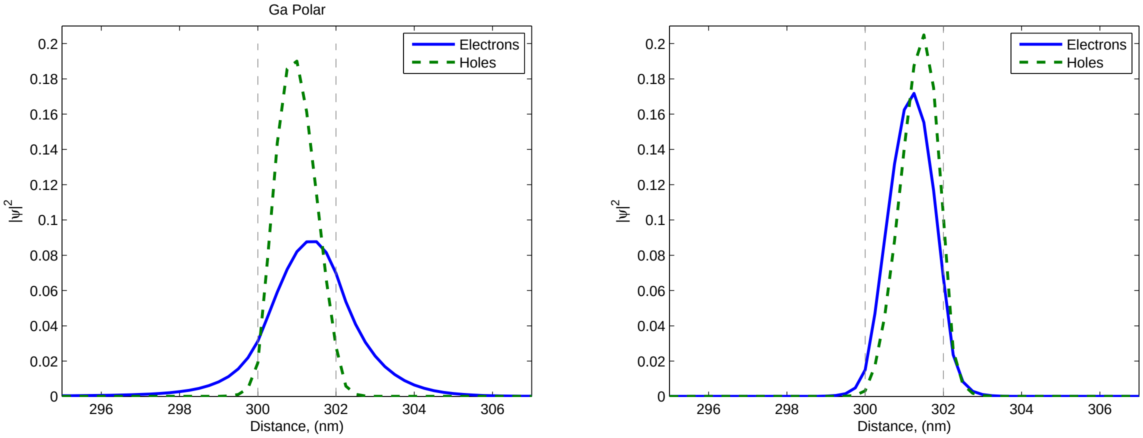

(c) Ga polar (d) N polar

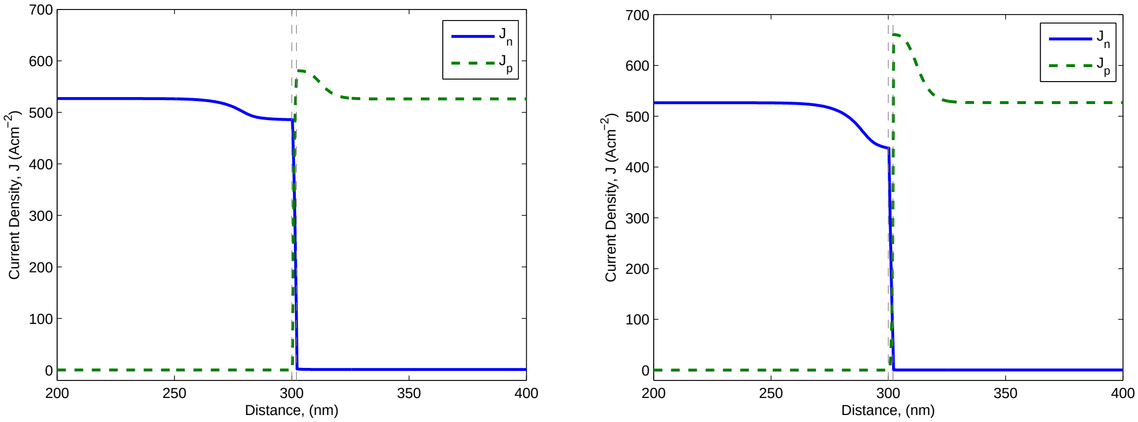

(e) Ga polar (f) N polar

Figure 5.15: Study of polarity effects on electronic properties. (a,b) Band diagrams, (c,d) Electron and hole envelop function overlap, (e,f) Partial electron and hole current density.

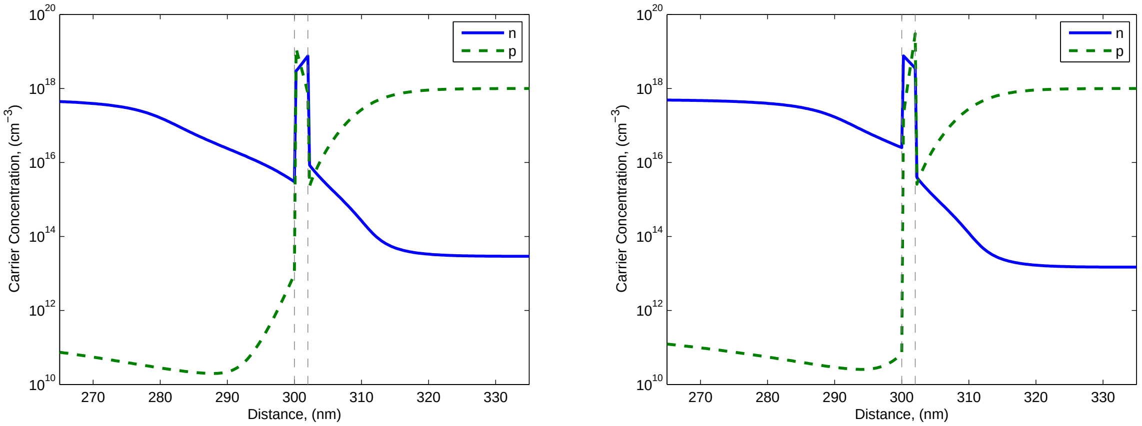

(a) Ga polar (b) N polar

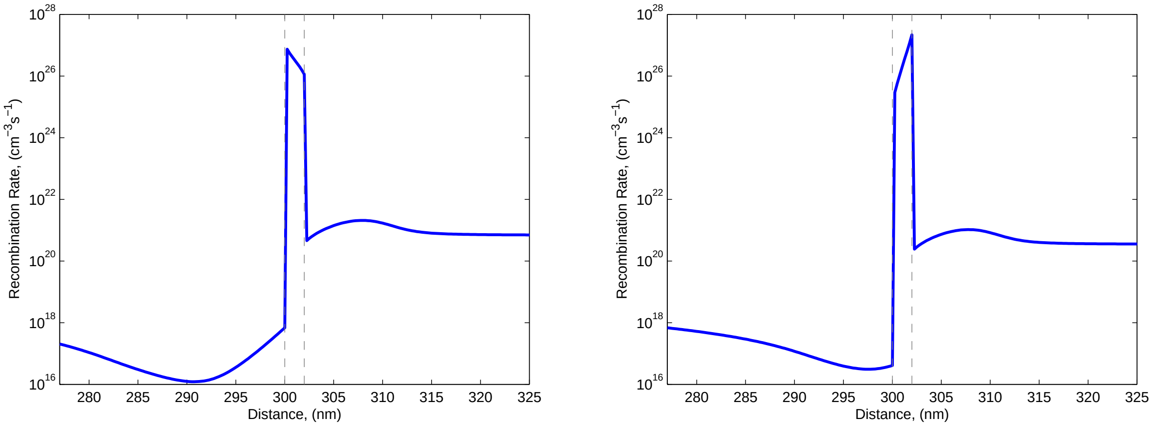

(c) Ga polar (d) N polar

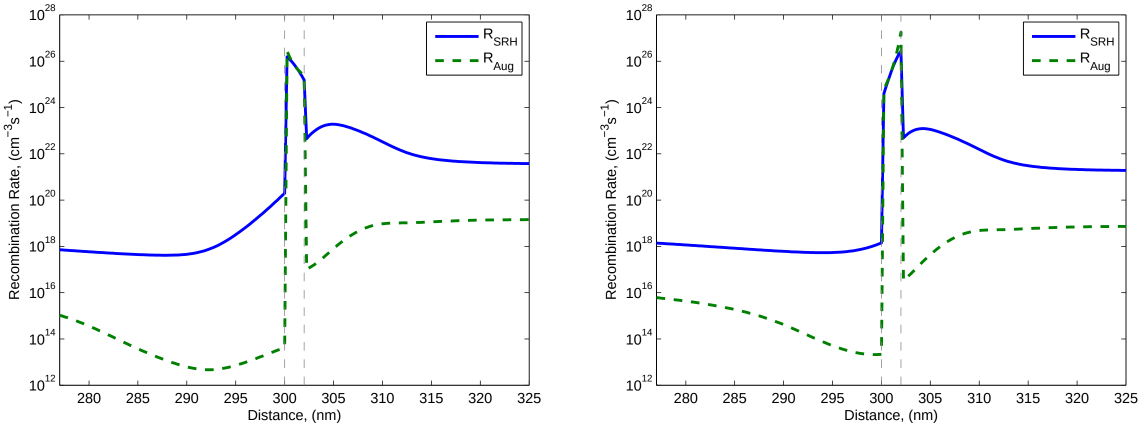

(e) Ga polar (f) N polar

Figure 5.16: Study of polarity effects on electronic properties. (a,b) Carrier concentrations, (c,d) Radiative recombination rate, (e,f) Non-radiative SRH and Auger recombination rates.

5.6.1 Quantum Well Thickness

To study the effects of quantum well thickness on the emission properties the structure in section 5.3 is simulated with varying quantum well thicknesses for same external bias. The thickness of the quantum well is varied from $1-5\ nm$. Fig. 5.17 shows the injection current density for different quantum well thicknesses. As the quantum well thickness is increased, current density increases with the QW thickness up until 3 nm and then it starts to reduce. The overlap of electron and hole wavefunction is shown in Fig. 5.19 for different QW thickness. The overlap between the electron and hole wave functions in the QW reduces with increasing the size of the QW. For wider QW's, higher order modes of envelop function also start to appear. Fig. 5.19d shows the second envelop function for 5 nm wide quantum well.

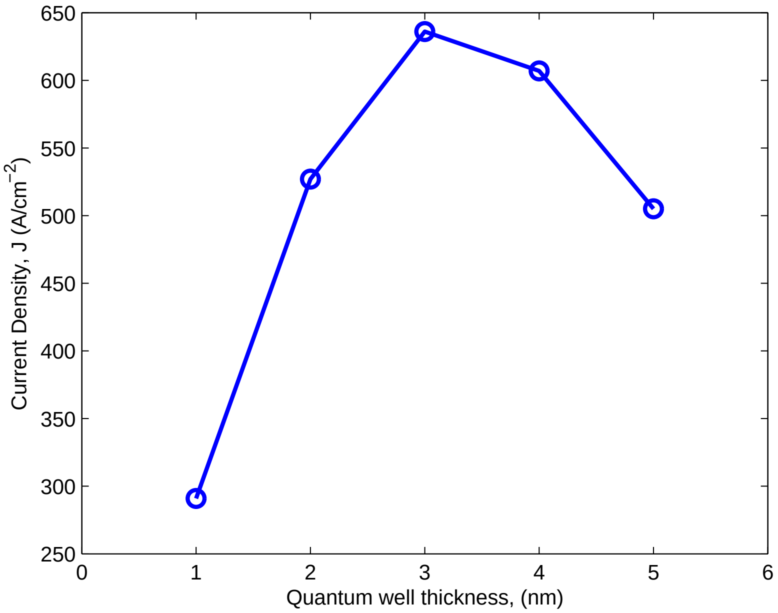

Figure 5.17: Current Desity as a function quantum well thickness in GaN/$\mathrm{In_yGa_{1-y}N}$/GaN structure.

The relation between quantum well thickness and emission wavelength is shown in Fig. 5.18. As the QW thickness increases, a red-shift in emission wavelength is observed.

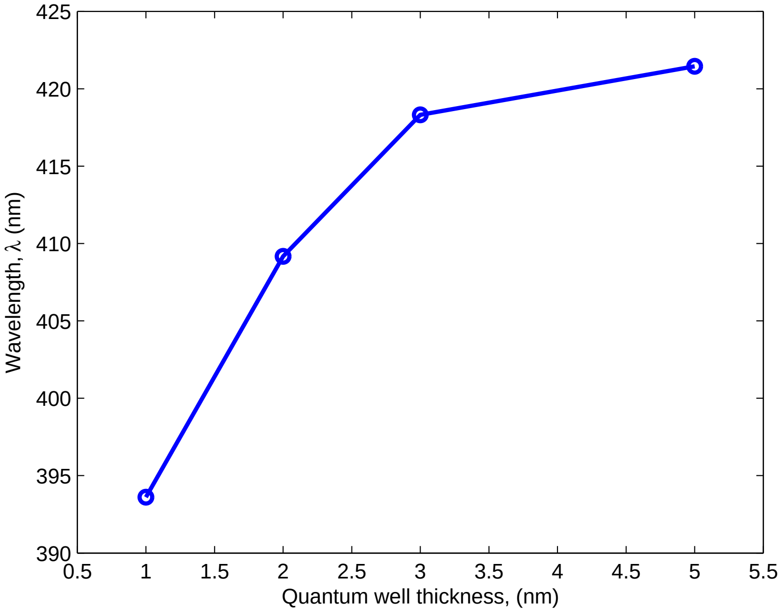

Figure 5.18: Emission wavelength as a function quantum well thickness in $\mathrm{GaN/In_yGa_{1-y}N/GaN}$ structure.

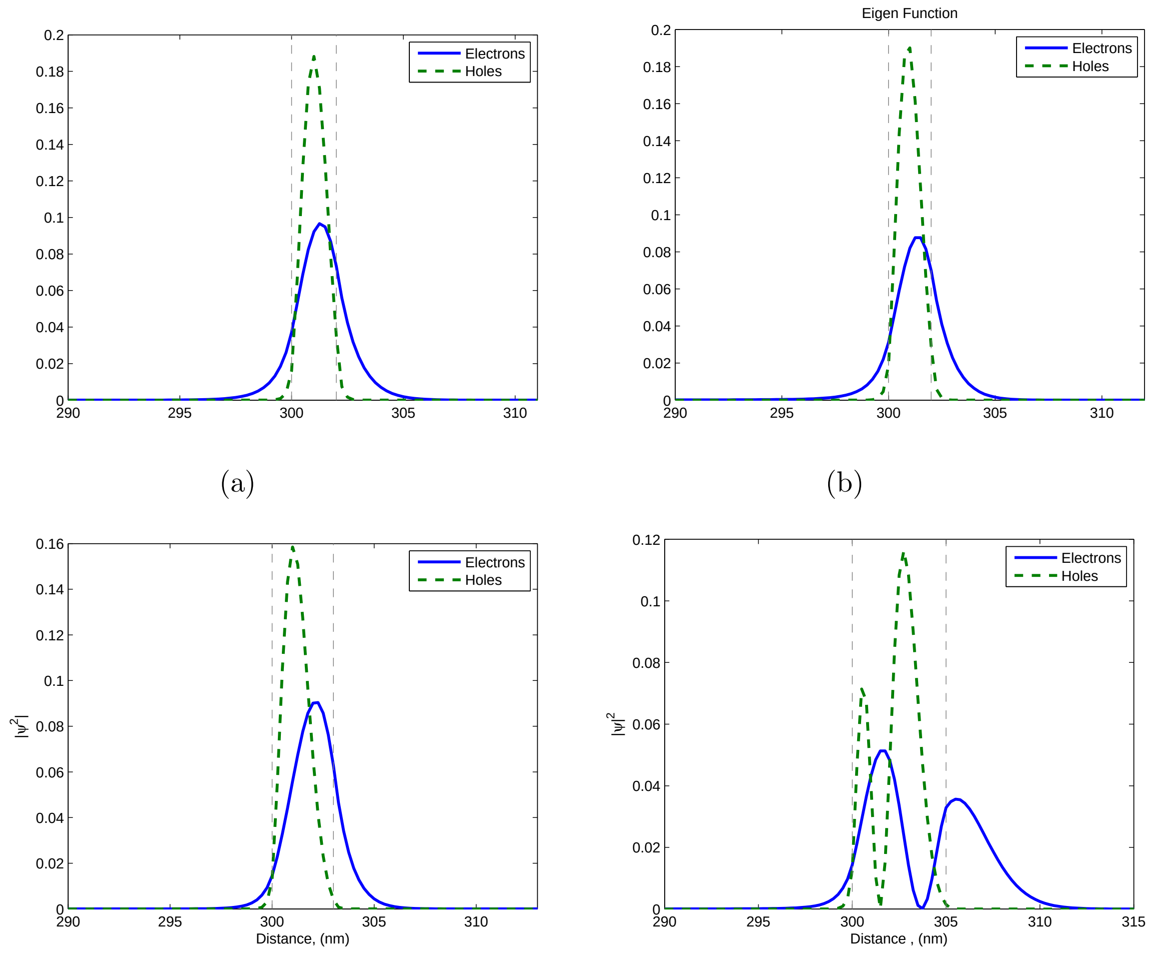

(a) (b)

(c) (d)

Figure 5.19: Electron and hole wavefunction envelop for different quantum well thicknesses W_{QW}. (a) $W_{QW} = 1\ nm$ (b) $W_{QW} = 2\ nm$ (c) $W_{QW} = 3\ nm$ (d) $W_{QW} = 5\ nm$

5.7 Effects of Indium (In) Concentration

Indium concentration in the quantum well determines the bandgap of the active region and hence the emission wavelength of the device. Increasing indium concentration in the quantum well, results in lower bandgap energy and higher emission wavelength. In this section, we study the effects of varying indium concentration on injection current density, band structures and electrons and holes wavefunction overlap.

The device described in section 5.3, is simulated with indium concentration y is increased from 0.15 to 0.45 in the $In_yGa_{1-y}N$ QW. The resulting bandgap and band offsets are shown in Table 5.4 below.

Table 5.4: Band parameters for different Indium (In) concentration in GaN/In$_y Ga_{1-y}N/GaN$ structure.

Parameter	Fractional Indium Concentration						
	0.15	0.20	0.25	0.30	0.35	0.40	0.45
Bandgap (eV)	2.987	2.850	2.712	2.575	2.437	2.30	2.162
Conduction Band Offset (eV)	0.130	0.174	0.217	0.261	0.304	0.348	0.391
Valence Band offset (eV)	0.281	0.376	0.470	0.564	0.658	0.752	0.846

Fig. 5.20 shows the effect of increasing In concentration on the injection current density for fixed bias. The current density increases up to $y = 0.25$ and then starts decreasing with In concentration.

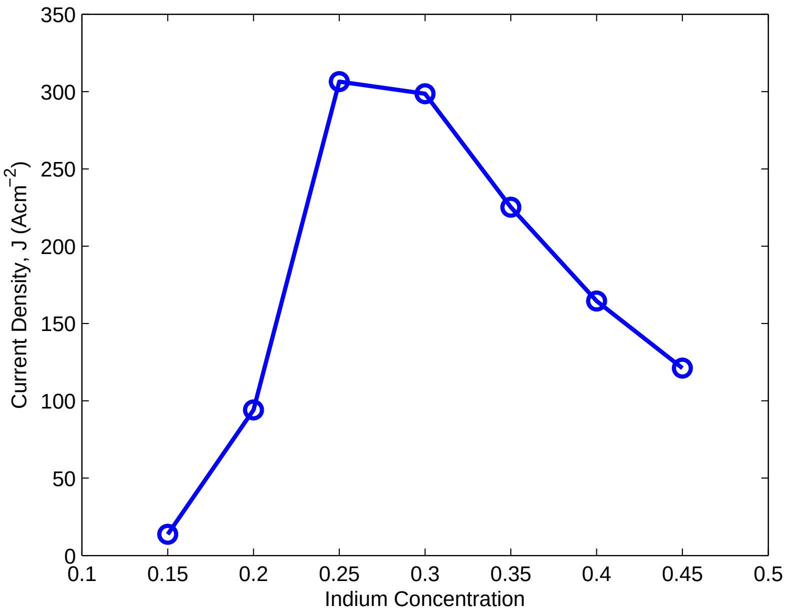

Figure 5.20: Current Desity as a function of In concentration in $GaN/In_yGa_{1-y}N/GaN$ structure.

Fig. 5.21 shows the behavior of emission wavelength with In concentration. There is a red shift in emission wavelength with increasing In concentration. This is due to the fact that the bandgap of the device decreases with increasing In concentration.

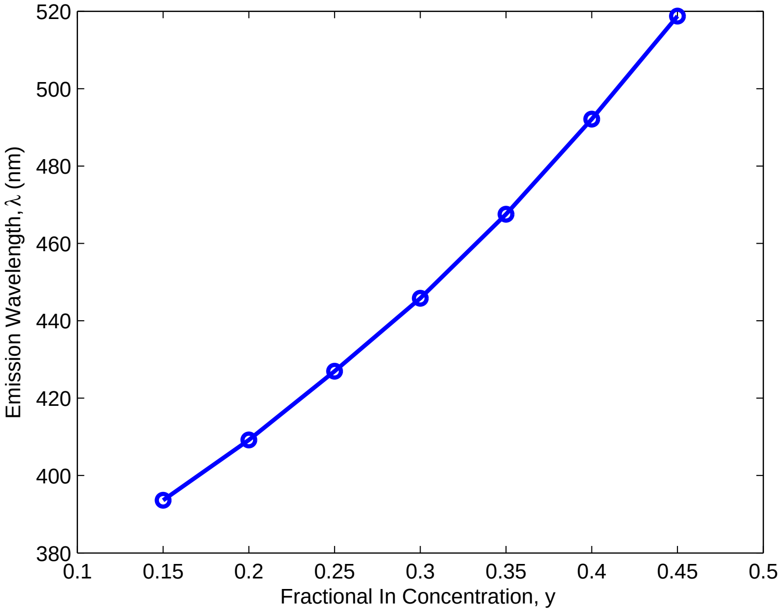

Figure 5.21: Emission wavelength as a function of In concentration in GaN/$In_yGa_{1-y}N$/GaN structure.

Fig. 5.22 shows the band diagram at In concentration of 0.20 and 0.35. It can be seen from the figure that the bands are more slanted for higher indium concentration. This is due to the extra polarization charges introduced at the interface of the QW because of the increased lattice mismatch between the contact layers and the QW region. These polarization charges also reduce the electron and hole wavefunction overlap. As shown in Fig. 5.23a and 5.23b, by increasing the indium concentration the electron wave function is shifted toward the p-interface and the hole wavefunction moves towards the n-interface of the quantum well.

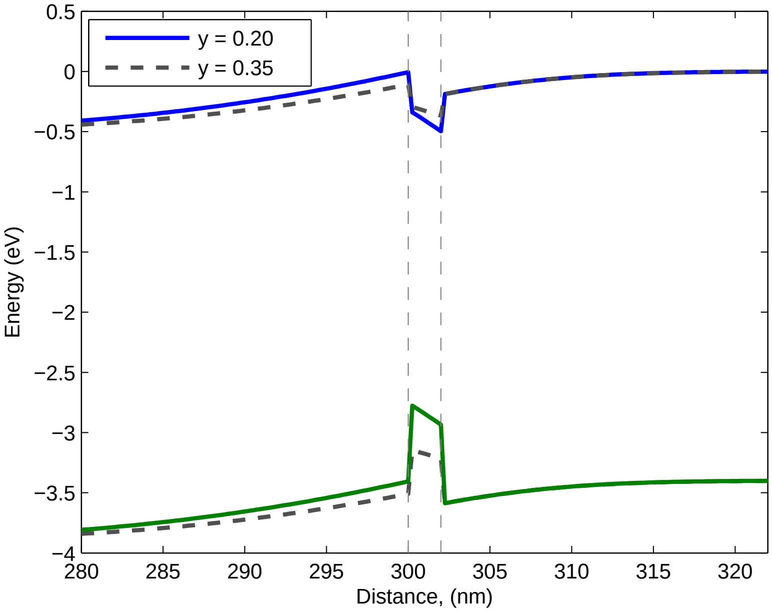

Figure 5.22: Conduction and valence band profile at In concentration, y = 0.2 and 0.3.

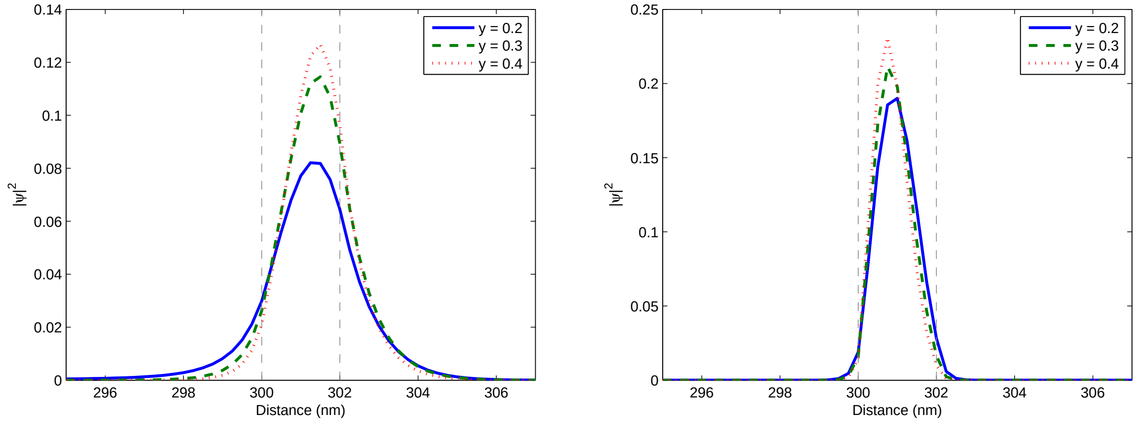

(a)

(b)

Figure 5.23: Wave function envelop for different In concentrations. (a) Electrons, (b) Holes.

5.8 Analysis of Asymmetric GaN/$In_yGa_{1-y}N$ Graded SQW Structure

In this section, we study an asymmetric quantum well. The asymmetry is introduced by gradually changing In concentration within QW thickness. This results in a monotonically increasing or decreasing bandgap. Here, we simulate two different devices referred as device A and device B from now on. In device A, In concentration is reduced from 0.3 to 0.1 as a linear function of QW thickness from n-GaN interface to p-GaN interface. This results in an increasing bandgap with distance. In case of device B, In concentration is increased from 0.1 to 0.3 from n-GaN to p-GaN interface resulting in a linear decrease in bandgap. Both the devices are simulated under similar conditions. The results for both devices are presented side by side in Fig. 5.24 and 5.25 below.

As can be seen from Fig. 5.24a and Fig. 5.24b, the bands in structure B are graded in the opposite direction. The emission wavelength for sturcture A and B is 389 and 414 *nm*, respectively. Structure B also has lower electric field in the quantum well and a smaller current density for the same external bias. This suggests that structure A will have smaller turn on voltage as compared to structure B. As can be seen from Fig. 5.25a and Fig. 5.25b, structure B provides better carrier confinement. Electron concentration in the p-GaN layer is 5 times smaller in structure B than structure A. Also, in structure B, the recombination rates are more uniform in the whole QW, where as in structure A, most of recombination processes occur at the n-GaN interface.

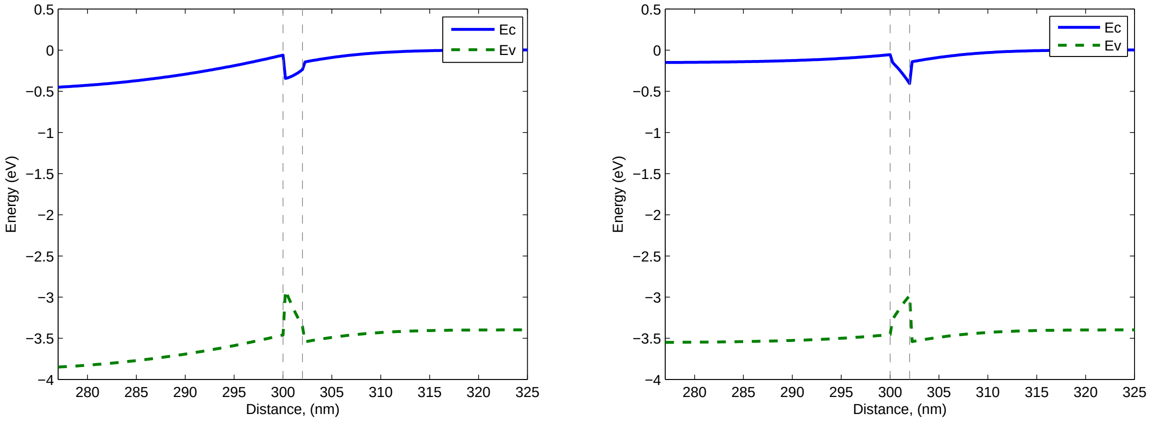

(a) Device A (b) Device B

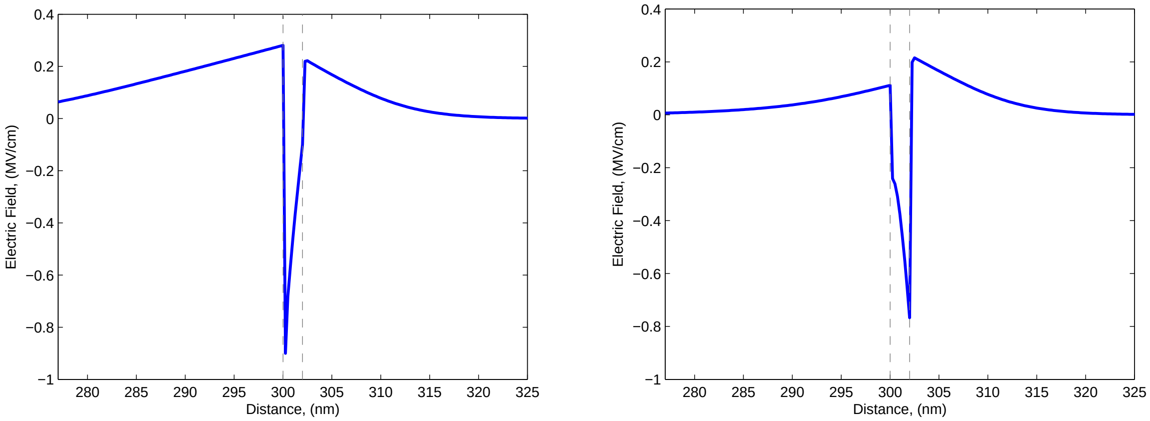

(c) Device A (d) Device B

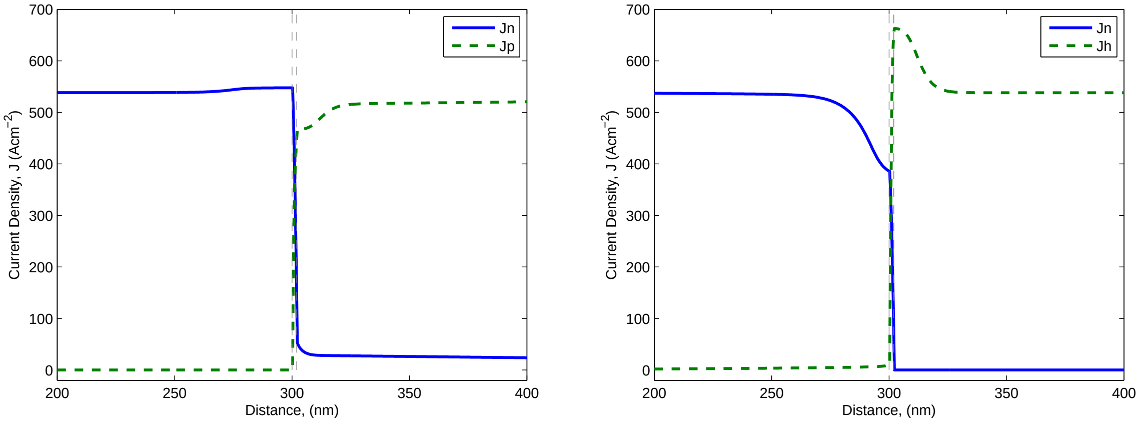

(e) Device A (f) Device B

Figure 5.24: Graded QW structures. (a,b) Energy bands diagram, (c,d) Electric field, (e,f) Partial electron and hole current density.

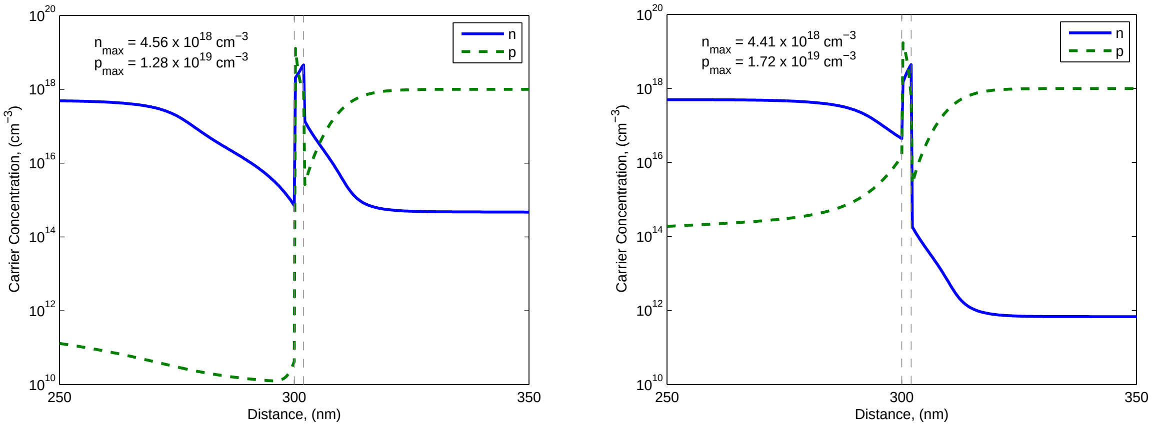

(a) Device A (b) Device B

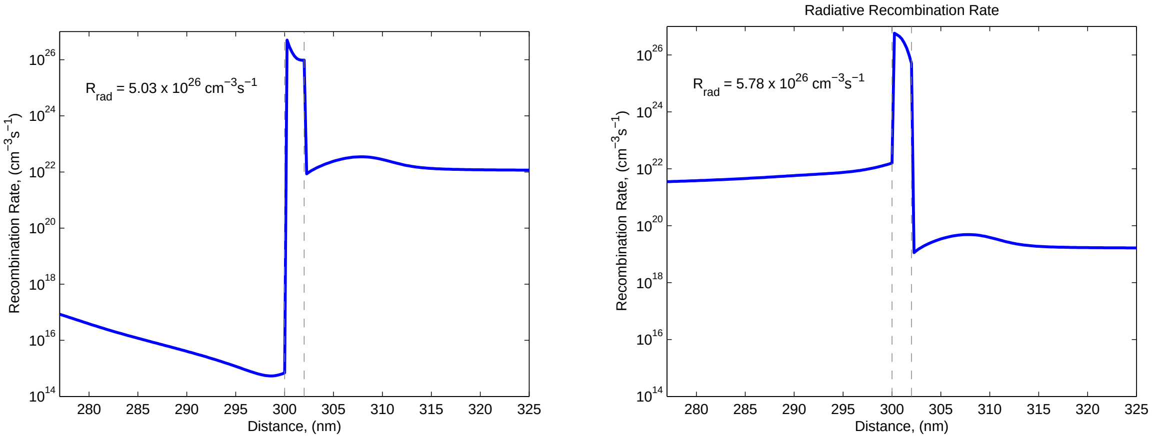

(c) Device A (d) Device B

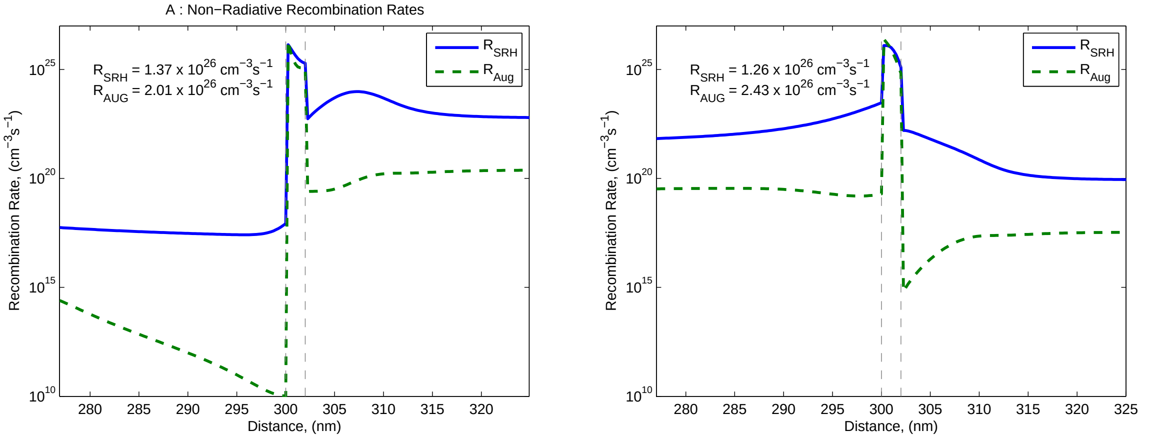

(e) Device A (f) Device B

Figure 5.25: Graded QW structures (a,b) Carrier concentration, (c,d) Radiative recombination rate, (e,f) Non-radiative SRH and Auger recombination rates.

Fig. 5.26a and Fig. 5.26a show the electrons and holes wavefunction overlap. In case of structure A, the electrons and holes wavefunction shifts in the opposite direction. This mis-alignment increases with the gradient of the conduction and valence bands profile. In structure B, the electrons and holes wavefunctions are more aligned with each other. Fig. 5.27 shows the overlap of second order envelop function in structure A.

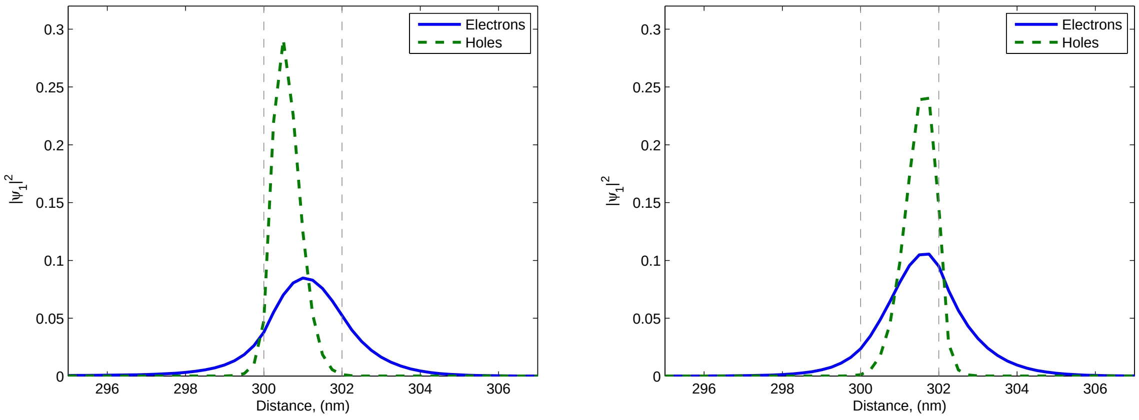

(a)

(b)

Figure 5.26: Electron and hole envelop function overlap for graded quantum well structure.

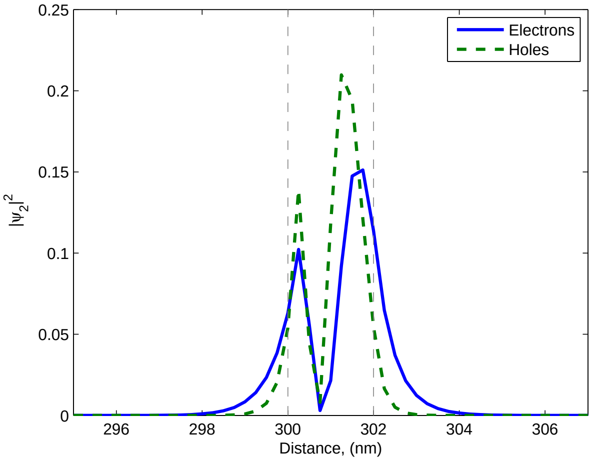

Figure 5.27: Electron and hole 2^{nd} envelop function overlap for graded quantum well structure.

5.9 Analysis of GaN/In$_{0.2}$Ga$_{0.8}$N SQW Structure with Al$_{0.2}$Ga$_{0.8}$N Electron Blocking Layer

The device simulated in this section consists of a 300 nm n-doped ($N_D = 5 \times 10^{17}\ cm^{-3}$) GaN layer, a 2 nm undoped quantum well followed by a 100 nm p-doped $Al_{0.2}Ga_{0.8}N$ electron blocking layer, followed by a 200 nm p-doped ($1 \times 10^{18}\ cm^{-3}$) GaN layer. The schematic of the device is shown in Fig. 5.28 below.

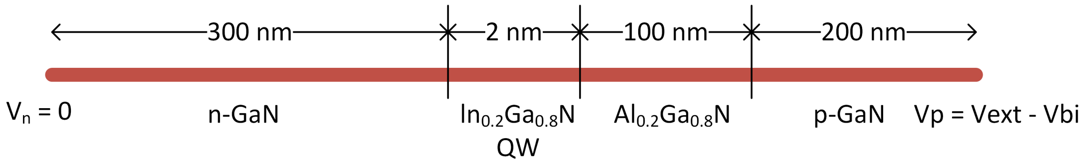

Figure 5.28: Schematic of the GaN/In$_{0.2}$Ga$_{0.8}$N/Al$_{0.2}$Ga$_{0.8}$N/GaN SQW structure.

The FDTD simulation size is 2408 points with $\Delta x = 0.25\ nm$ and $\Delta t = 5.0 \times 10^{-18}\ s$. The device is biased at to $V_p = V_{ext} - V_{bi}$ at p-contact and $V_n = 0$ at the n-contact. The material parameters used for EBL layer in this device are presented in Table 5.5.

Table 5.5: Parameters used for $\mathrm{Al}_{0.2}\mathrm{Ga}_{0.8}\mathrm{N}$ EBL layer.

Parameter Name	Value	Units
Electron concentration in n-GaN layer	5×10^{17}	cm^{-3}
Hole concentration in EBL layer	1×10^{18}	cm^{-3}
Hole concentration in p-GaN layer	1×10^{18}	cm^{-3}
Bandgap of $\mathrm{Al}_{0.2}\mathrm{Ga}_{0.8}\mathrm{N}$	3.96	eV
Relative dielectric constant of $\mathrm{Al}_{0.2}\mathrm{Ga}_{0.8}\mathrm{N}$	8.82	–
Effective DOS of electrons in $\mathrm{Al}_{0.2}\mathrm{Ga}_{0.8}\mathrm{N}$, N_c	3.03×10^{18}	cm^{-3}
Effective DOS of holes in $\mathrm{Al}_{0.2}\mathrm{Ga}_{0.8}\mathrm{N}$, N_v	1.35×10^{20}	cm^{-3}

An external bias of 2.86 V is applied on the p-contact. The simulation is run for a total time of 100 ps. Electronic characteristics obtained for this device from the simulation are presented in Fig. 5.29.

Due to high band gap of $Al_{0.2}Ga_{0.8}N$ layer, there is a large increase in the the conduction band offset of the quantum well on the right side as shown in Fig. 5.29a. This offset reduces electron leakage from the active region into the bulk. The electron concentration in the p-GaN is reduced by a factor of 10 as compared to the structure without the EBL layer in Fig. 5.11. This also results in an increase in the total electron concentration in the QW. As a result, the electron density in the QW is higher than the holes in the QW as shown in Fig. 5.29d, which is not the case in the structure without the EBL layer. The radiatve recombination rate for the EBL structure is shown in Fig. 5.29e. The recombination process occurs mainly in the quantum well. For the non-radiative SRH recombination rate, a noticeable recombination occurs in the n-GaN layer, but it is still insignificant as compared to the recombination in the QW despite the thickness of the n-GaN layer. The emission wavelength is found to be 402 nm, which is lower as compared to 409 nm for the structure with out the EBL layer.

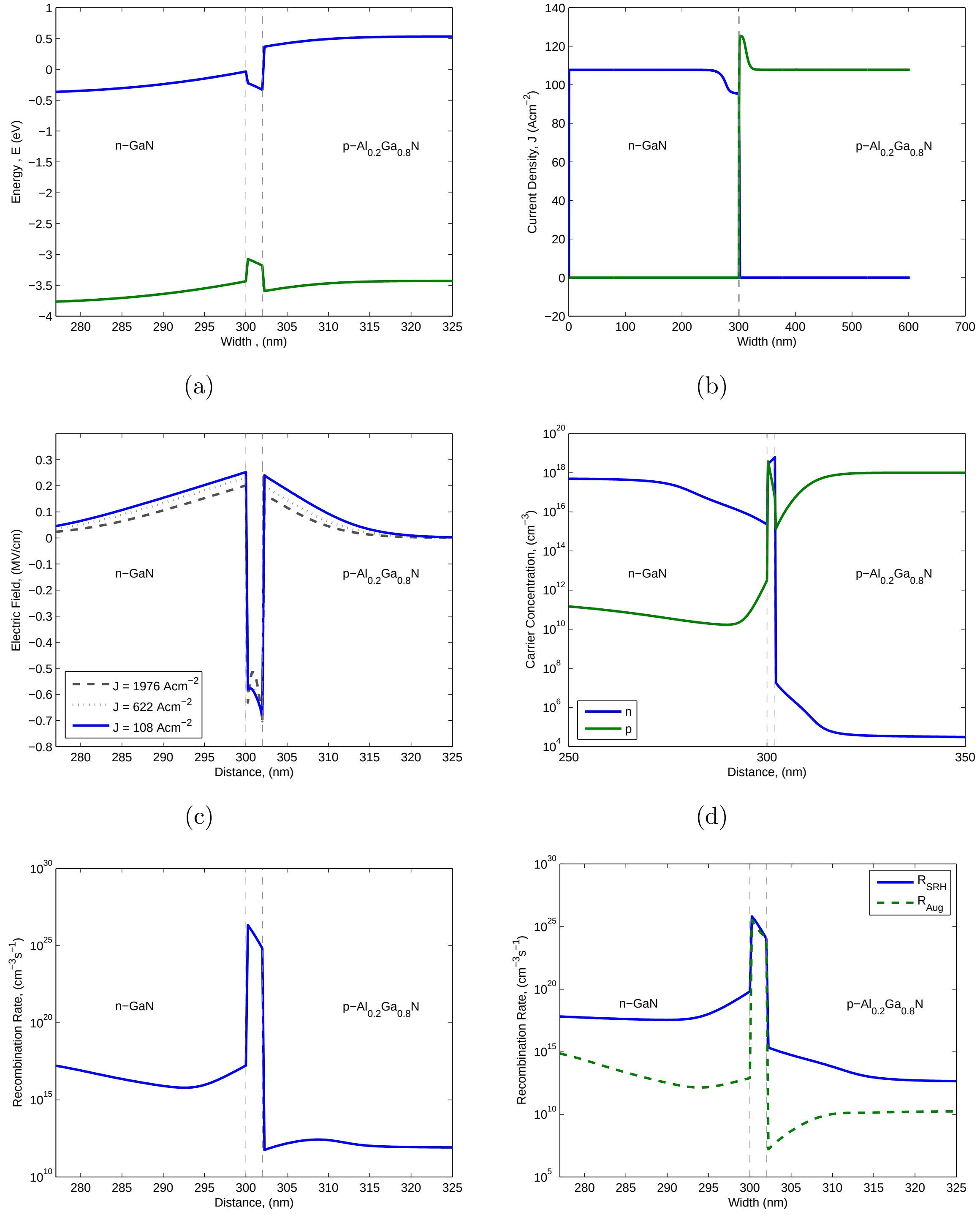

(a) (b)

(c) (d)

(e) (f)

Figure 5.29: GaN/$In_{0.2}Ga_{0.8}N$ SQW structure with $Al_{0.2}Ga_{0.8}N$ electron blocking layer. (a) Band diagram, (b) Partial current denstiy, (c) Electric field, (d) Carrier concentration, (e) Radiative recombination rate, (f) Non-radiative SRH and Auger recombination rates.

CHAPTER 6

SIMULATION OF A TWO DIMENSIONAL GAN/INGAN/GAN BASED DISK-IN-NANOWIRE LED

Two dimensional carrier transport simulations are performed in this chapter using the Q-FDTD solver. A 2D cross section of the disk-in-nanowire device is simulated. Numerical simulations are carried out in order to analyze the effect of the thickness of the disk-in-nanowire structure. Electronic characteristics including distribution of electrostatic potential, current density, recombination processes and electron hole wavefunctions are studied in this chapter.

6.1 Analysis of GaN/In$_{0.2}$Ga$_{0.8}$N/GaN QD-NW Structure

A two dimensional GaN/In$_{0.2}$Ga$_{0.8}$N/GaN QD-NW with radius R is simulated using the two dimensional QFDTD solver. The simulated structure consists of a 150 nm n-GaN layer ($N_D = 5 \times 10^{17}\ cm^{-3}$), an undoped 3 nm In$_{0.2}Ga_{0.8}$N quantum disk and 150 nm p-GaN layer ($N_A = 1 \times 10^{18}\ cm^{-3}$). Schematic of the structure is shown in Fig. 6.1.

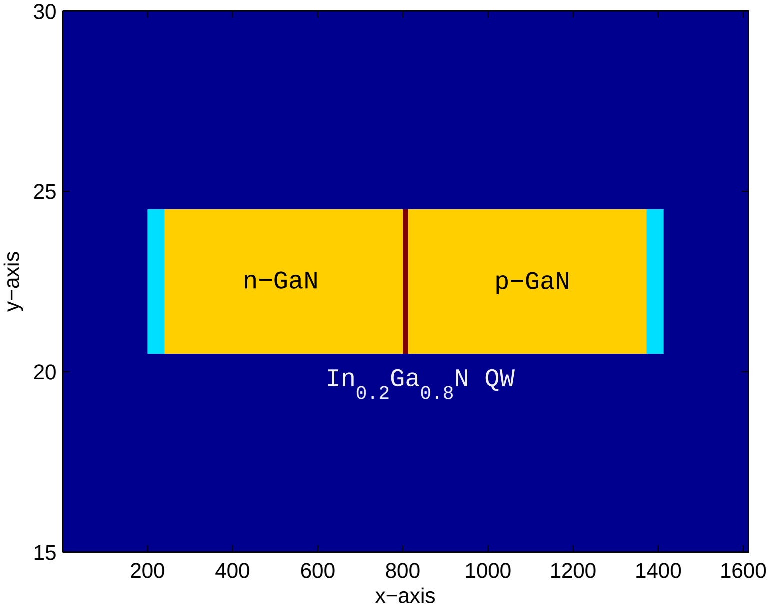

Figure 6.1: Schematic of the two dimensional GaN/In$_{0.2}$Ga$_{0.8}$N/GaN QD-NW structure

The FDTD simulation size is 1612×44 points with $\Delta x = 0.25\ nm$ and $\Delta y = 2.5\ nm$ with time step of $\Delta t = 5.0 \times 10^{-18}\ s$. The device is biased at $V_{ext} = 3.16\ V$ at p-contact and $V_n = 0$ at the n-contact. The material parameters used of this device are presented in Table 5.3.

6.2 Electrostatic Potential

The potential profile as a function of device radii is shown in Fig. 6.2. It can be seen from the figure, that most of the voltage drop is across the quantum well. The equi-potential lines go out from the nanowire into the air, where they can couple to the neighbouring nanowires. Also the curvature of the equi-potential lines increases with the radius of the nanowire.

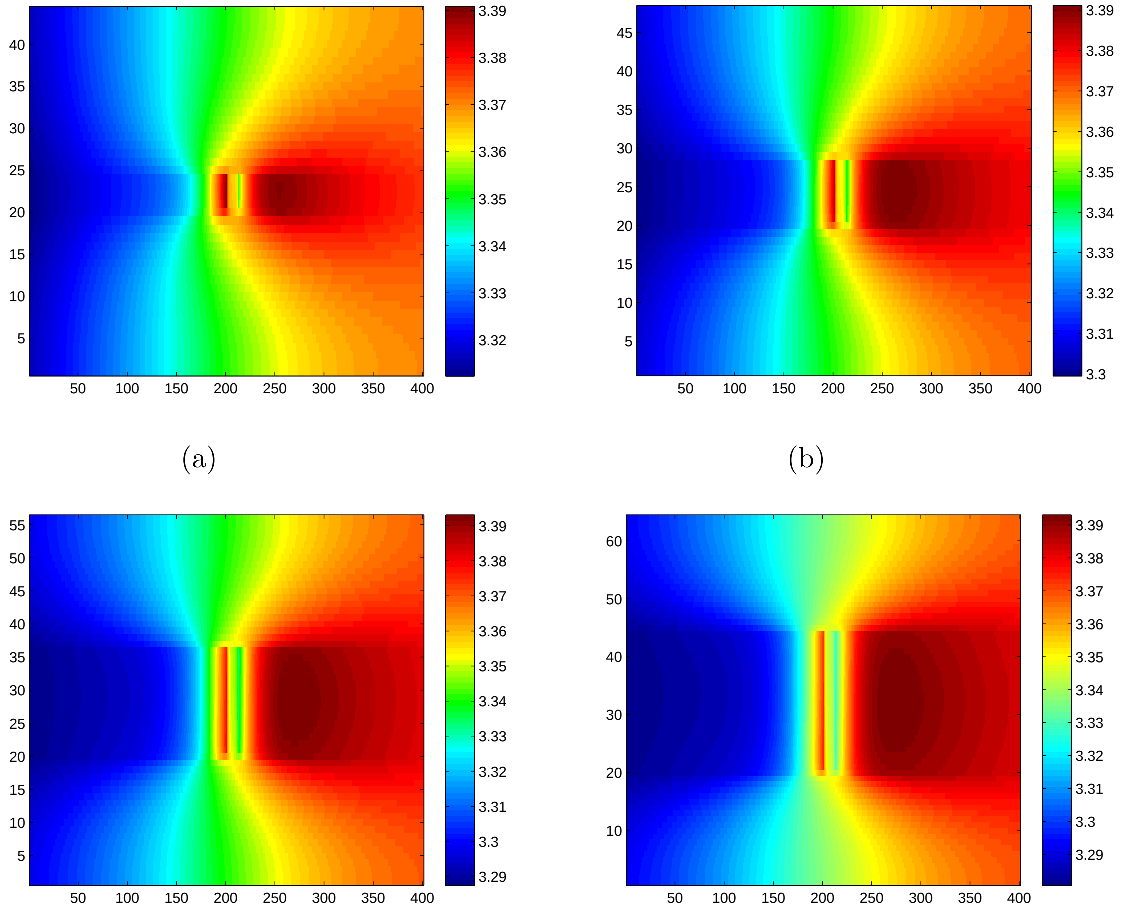

(a)

(b)

(c)

(d)

Figure 6.2: Electrostatic potential distribution in two dimensional GaN/In$_{0.2}$Ga$_{0.8}$N/GaN QD-NW structure (a) Radius = 5 nm, (b) Radius = 10 nm, (c) Radius = 20 nm, (d) Radius = 30 nm.

6.3 Time Dependent Current Density

Fig. 6.3a shows the current density for different radius of the device. As can be seen from the figure, as the radius of the nanowire increases, the current density also increases with it. For radius change from 5 nm to 30 nm, the current density increases from 2592 Acm^{-2} to 3900 Acm^{-2}. As the radius of the nanowire is increased, the rate of change in the current density decreases. The total current for the device is shown in Fig. 6.3b.

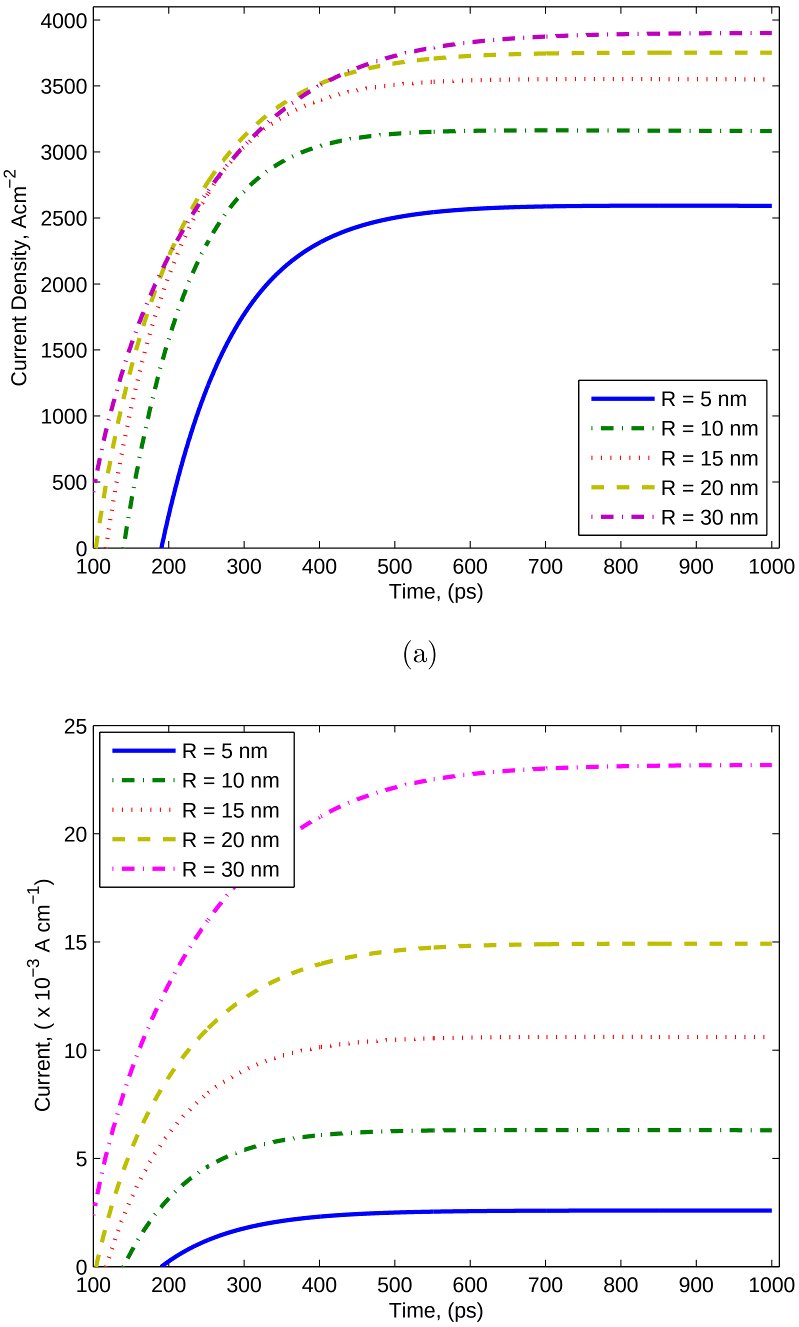

(a)

(b)

Figure 6.3: Current density and current for 5, 10, 15, 20 and 30 *nm* radius for GaN/In$_{0.2}$Ga$_{0.8}$N/GaN QD-NW structure. (a) Current density, (b) Current.

6.4 Recombination Rates

The dependence of radiative and non-radiative recombination rates on the radius of the nanowire is shown in Fig. 6.4. The radiative recombination is higher in the structure with smaller radius. As the radius of the device is increased, radiative recombination decreases. The non-radiative recombination (especially Auger processes) shows a much stronger dependence on radius than the radiative recombination rate. From Fig. 6.4 it can be observed that by decreasing the radius of the device the internal quantum efficiency is reduced dramatically. It can be seen from the figure below that at around 27 *nm* radius the radiative and non-radiative recombination rates become equal.

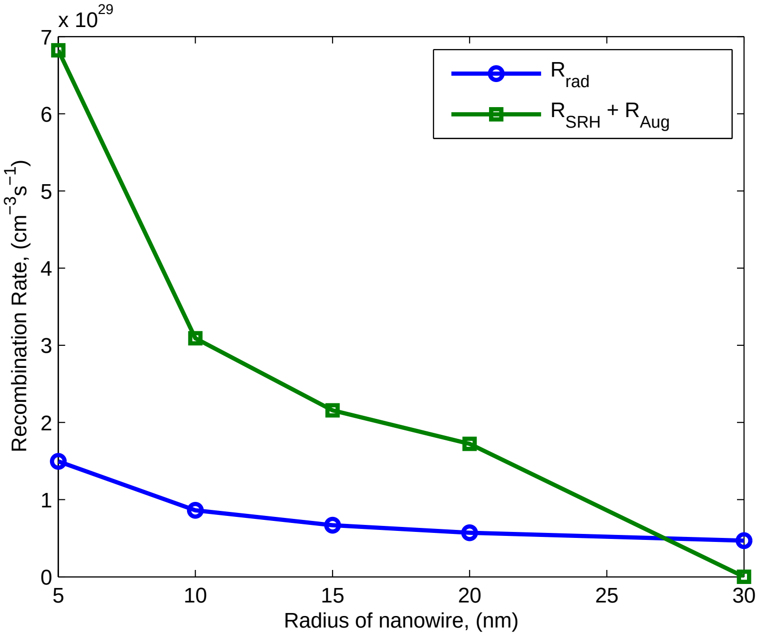

Figure 6.4: Radiative and non-radiative recombination rates for different radii of nanowire.

6.5 Emission Wavelength and Electron and Hole wavefunction

The emission wavelength for this device is calculated as 435 nm. Fig. 6.5a shows the effects of radius on the electron wavefunction. As the radius is increased, the electron wavefunction is shifted to the p-GaN QW interface. Similarly, hole wavefunction shifts to the n-GaN QW interface as shown in Fig. 6.5b.

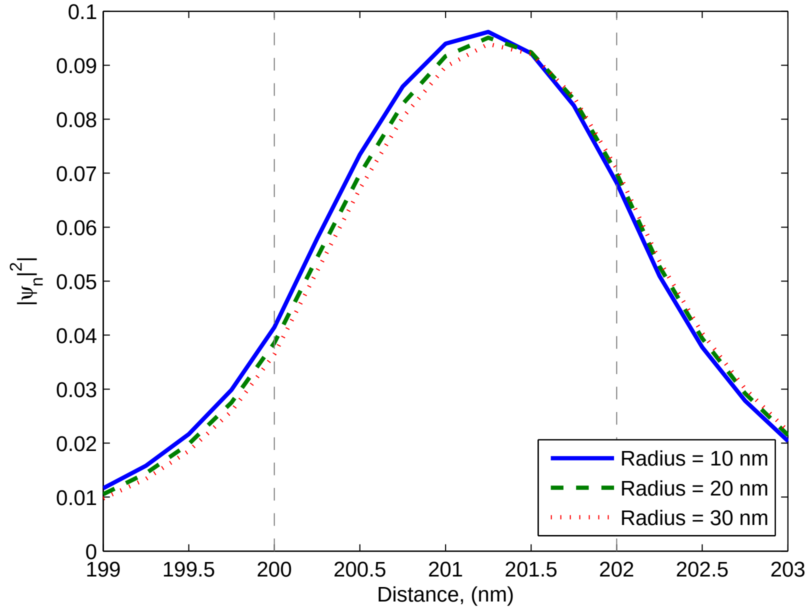

(a)

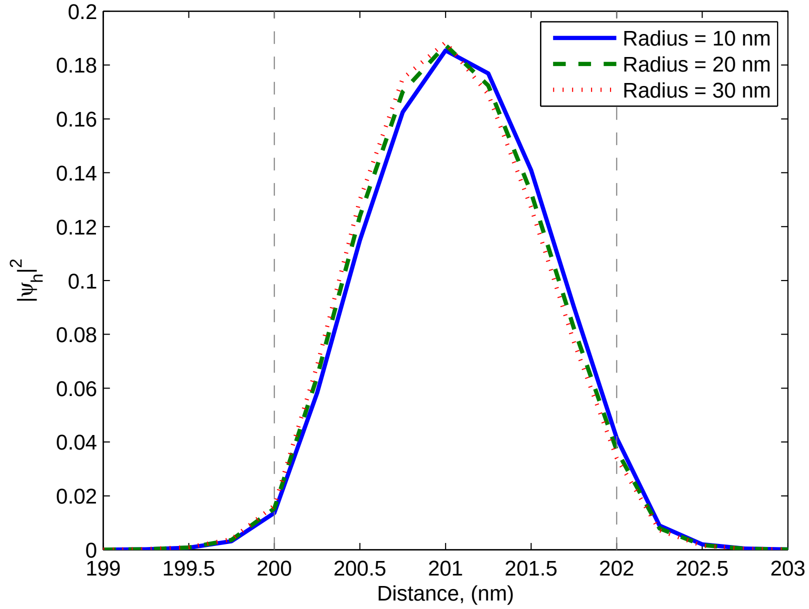

(b)

Figure 6.5: Electron and hole wavefunction for 10, 20 and 30 nm radius for GaN/In$_{0.2}$Ga$_{0.8}$N/GaN QD-NW structure. (a) Electron wavefunction, (b) Hole wavefunction.

CHAPTER 7

7.1 Summary

In this thesis, a Quantum Finite Difference Time Domain (Q-FDTD) solver is developed to simulate a two dimensional disk in nanowire structure (QD-NW) for solid state lighting applications. The Q-FDTD solver developed in this thesis is based on coupled Drift-Diffusion model with Schrödinger equation. The Q-FDTD solver is used to simulate and analyze the emission properties of an InGaN/GaN SQW based LED structure. The work done in this thesis is summarized below.

- A time domain Q-FDTD solver is developed for the simulation of quantum-disk-in-nanowire structure. The proposed solver is based on a self-consistent solution of Schrödinger equation with the classical Drift-Diffusion model which consists of Poisson equation, current continuity equations and drift-diffusion current equations.

- Various physical properties of III-nitride materials such as spontaneous and piezoelectric polarization, electric field and doping dependence of mobility and diffusion coefficients are included in the Q-FDTD solver for GaN, InN and AlN.

- Models for radiative recombination rate, Shockley-Read-Hall recombination (SRH) and Auger recombination are incorporated in the solver.
- A one-dimensional GaN/$\mathrm{In_yGa_{1-y}N}$/GaN device is simulated with the Q-FDTD solver. Various electronic device properties such as band diagrams, carrier concentration, electric field profile, recombination rates, I-V curves, internal quantum efficiency, emission wavelength and electron hole wavefunction overlap are studied.
- The effects on emission wavelength, injection current density and electron and hole wavefunction overlap are studied for different parameters like crystal polarity, quantum well width and variation of In concentration in the quantum well.
- An $\mathrm{Al_xGa_{1-x}N}$ electron blocking layer is added to the GaN/InGaN structure and its effects on emission wavelength, carrier concentration, current density, band diagrams, recombination rates and electron hole wavefunction overlap are studied and compared to the device without the EBL layer.
- The Q-FDTD solver is extended to two dimensional simulation of devices. A two-dimensional GaN/$\mathrm{In_yGa_{1-y}N}$/GaN disk-in-nanowire structure is simulated to study the effects of nano-wire radius on current density, voltage distribution, recombination rates and electron hole wavefunction are studied.

7.2 Conclusions

The following points can be concluded from the simulations performed in this thesis

- Injection current density and radiative recombination rates in quantum well structures are affected by different parameters. These include the recombination coefficients, dislocation densities, the overlap of electron and hole wave functions and the radius of the nanowire.
- The envelop wave function of holes is more confined to the quantum well than electrons. This is due to the fact that the effective mass of holes is larger compared to the effective mass of electrons in III-nitride materials.
- Crystal polarity plays an important role in determining the electronic device properties. It was found that N polar structures provide more electron hole wave function overlap and high current density for the same external bias than Ga polar structure.
- The thickness of quantum well effects injection current density, emission wavelength and electron-hole wave function overlap. It was found that injection current density increases with increasing quantum well thickness up to 3 nm, after which current density decreases with the increase in quantum well thickness. Emission wavelength also increases with quantum well thickness. The overlap of electron and hole wave functions decreases with increasing the quantum well thickness.

- Indium concentration in the quantum well determines the bandgap and polarization sheet charge density which affects emission wavelength, current density and electron-hole wave function overlap. Emission wavelength increases with increasing In concentration. Also, increasing indium concentration increases the polarization charges on the quantum well interfaces which results in less overlap of electron-hole wave function. Current density starts to increases with increasing In concentration up 0.25, after which it start to decrease.

- In the case of asymmetrical quantum wells it was found that graded quantum well can be used to tune band profile, emission wavelength, recombination rates, carrier concentration and electron-hole overlap function.

- The inclusion of electron blocking layer (EBL) in the device, significantly improves electrons density in the quantum well and hence improve its radiative recombination rate. Also, the inclusion of EBL layer results in a decrease in the emission wavelength and increases the turn-on voltage of the device.

- In the case of two dimensional simulation, the effects of radial confinement in the Disk-in-Nanowire are demonstrated. It is shown that for fixed bias, the current density in the device increases with increasing radius of the nanowire.

- The radiative recombination rate increases with decreasing the radius of the nanowire.

- The non-radiative recombination rates increases faster than the radiative recombination rate with decreasing radius of the nanowire.
- With increasing the radius of the nanowire, the overlap between electron and hole wave functions decreases.

7.3 Future Work

Improvements can be made in the modeling of material parameters, Q-FDTD model and numerical solving techniques. Some suggestions for future extensions of this work are given below.

- Extending the solver to three dimensions, so that confinement in the quantum well due to small radius of the nanowire can be analyzed more accurately.

- Extension of the Schrödinger solver in order to simulate multiple quantum well structures.

- Incorporation of full electronic band structure for GaN and its alloys in the model using $k.p$ method to find the emission spectrum of the light emitting device.

- Including self-heating effects in the solver.

- The drift-diffusion model used for carrier transport is an approximation of Boltzmann equation. The accuracy of the solver can be improved by using more exact and better model for electronic transport.

- In this thesis, the Drift-Diffusion and Schrödiger solver run on the same grid, so they both use the same grid discretization size. This makes the grid size unnecessarily large, and requires more computational resources and simulation run time. This situation can be solved by running the Schrödinger and DD solver on separate grids.

REFERENCES

[1] Navigant Consulting, Inc., Radcliffe Advisors, and SSLS, Inc., "Solid-State Lighting Research and Development, Multi-Year Program Plan FY09-FY14," Lighting Research and Development Building Technologies Program; Office of Energy Efficiency and Renewable Energy, U.S. Department of Energy, Tech. Rep., March 2008.

[2] M. Krames, O. Shchekin, R. Mueller-Mach, G. O. Mueller, L. Zhou, G. Harbers, and M. Craford, "Status and Future of High-Power Light-Emitting Diodes for Solid-State Lighting," *Display Technology, Journal of*, vol. 3, no. 2, pp. 160–175, June 2007.

[3] R. V. Steele, "The story of a new light source," *Nature Photonics*, vol. 1, no. 1, pp. 25–26, June 2007.

[4] S. Nakamura, "Current Status of GaN-Based Solid-State Lighting," *MRS Bulletin*, vol. 34, pp. 101–107, 2 2009.

[5] S. Pimputkar, J. S. Speck, S. P. DenBaars and S. Nakamura, "Prospects for LED lighting," *Nature Photonics*, vol. 3, pp. 180–182, April 2009.

[6] L. Rigutti, G. Jacopin, A. D. L. Bugallo, M. Tchernycheva, E. Warde, F. H. Julien, R. Songmuang, E. Galopin, L. Largeau, and J.-C. Harmand, "Investigation of the electronic transport in GaN nanowires containing GaN/AlN quantum discs," *Nanotechnology*, vol. 21, no. 42, p. 425206, 2010.

[7] F. Rmer and B. Witzigmann, "Computational modelling of surface effects in InGaN/GaN quantum disk nano wire LEDs," *Proc. SPIE*, vol. 8619, pp. 86 190F–86 190F–9, 2013. [Online]. Available: http://dx.doi.org/10.1117/12.2006182

[8] A. F. Jarjour, R. A. Taylor, R. A. Oliver, M. J. Kappers, C. J. Humphreys, and A. Tahraoui, "Electrically driven single InGaN/GaN quantum dot emission," *Appl. Phys. Lett.*, vol. 93, no. 23, pp. 233 103–233 103, 2008.

[9] J. Kalden, C. Tessarek, K. Sebald, S. Figge, C. Kruse, D. Hommel, and J. Gutowski, "Electroluminescence from a single InGaN quantum dot in the green spectral region up to 150 K," *Nanotechnology*, vol. 21, no. 1, p. 015204, 2010. [Online]. Available: http://stacks.iop.org/0957-4484/21/i=1/a=015204

[10] W. C. Ke, C. P. Fu, C. Y. Chen, L. Lee, C. S. Ku, W. C. Chou, W.-H. Chang, M. C. Lee, W. K. Chen, W. J. Lin, and Y. C. Cheng, "Photoluminescence properties of self-assembled InN dots embedded in GaN grown by metal organic vapor phase epitaxy,"

Appl. Phys. Lett., vol. 88, no. 19, pp. –, 2006. [Online]. Available: http://scitation.aip.org/content/aip/journal/apl/88/19/10.1063/1.2203510

[11] Q. Li, K. R. Westlake, M. H. Crawford, S. R. Lee, D. D. Koleske, J. J. Figiel, K. C. Cross, S. Fathololoumi, Z. Mi, and G. T. Wang, "Optical performance of top-down fabricated InGaN/GaN nanorod light emitting diode arrays," *Opt. Express*, vol. 19, no. 25, pp. 25 528–25 534, Dec 2011. [Online]. Available: http://www.opticsexpress.org/abstract.cfm?URI=oe-19-25-25528

[12] Y. J. Lu, H. W. Lin, H. Y. Chen, Y. C. Yang, and S. Gwo, "Single InGaN nanodisk light emitting diodes as full-color subwavelength light sources," *Appl. Phys. Lett.*, vol. 98, no. 23, pp. –, 2011. [Online]. Available: http://scitation.aip.org/content/aip/journal/apl/98/23/10.1063/1.3597211

[13] S. Nakamura, M. Senoh, N. Iwasa, and S. ichi Nagahama, "High-Brightness InGaN Blue, Green and Yellow Light-Emitting Diodes with Quantum Well Structures," *Japanese Journal of Applied Physics*, vol. 34, no. 7A, p. L797, 1995. [Online]. Available: http://stacks.iop.org/1347-4065/34/i=7A/a=L797

[14] M. Zhang, P. Bhattacharya, and W. Guo, "InGaN/GaN self-organized quantum dot green light emitting diodes with reduced efficiency droop," *Appl. Phys. Lett.*, vol. 97, no. 1, pp. –, 2010. [Online]. Available: http://scitation.aip.org/content/aip/journal/apl/97/1/10.1063/1.3460921

[15] C. Kölper, M. Sabathil, F. Römer, M. Mandl, M. Strassburg, and B. Witzigmann, "Core-shell InGaN nanorod light emitting diodes: Electronic and op-

tical device properties," *Physica Status Solidi Applied Research*, vol. 209, pp. 2304–2312, Nov. 2012.

[16] A. Irrera, P. Artoni, F. Iacona, E. F. Pecora, G. Franz, M. Galli, B. Fazio, S. Boninelli, and F. Priolo, "Quantum confinement and electroluminescence in ultrathin silicon nanowires fabricated by a maskless etching technique," *Nanotechnology*, vol. 23, no. 7, p. 075204, 2012. [Online]. Available: http://stacks.iop.org/0957-4484/23/i=7/a=075204

[17] J. H. Son, J. U. Kim, Y. H. Song, B. J. Kim, C. J. Ryu, and J. L. Lee, "Design Rule of Nanostructures in Light-Emitting Diodes for Complete Elimination of Total Internal Reflection." *Adv. Mater*, vol. 24, no. 17, p. 22592262, 2012.

[18] W. Guo, A. Banerjee, P. Bhattacharya, and B. S. Ooi, "InGaN/GaN disk-in-nanowire white light emitting diodes on (001) silicon," *Appl. Phys. Lett.*, vol. 98, no. 19, pp. –, 2011. [Online]. Available: http://scitation.aip.org/content/aip/journal/apl/98/19/10.1063/1.3588201

[19] F. Glas, "Critical dimensions for the plastic relaxation of strained axial heterostructures in free-standing nanowires ," *Phys. Rev. B*, vol. 74, p. 121302, Sep 2006. [Online]. Available: http://link.aps.org/doi/10.1103/PhysRevB.74.121302

[20] J. Ristić, E. Calleja, A. Trampert, S. Fernández-Garrido, C. Rivera, U. Jahn, and K. H. Ploog, "Columnar AlGaN/GaN Nanocavities with AlN/GaN Bragg Reflectors Grown by Molecular Beam Epitaxy on Si(111),"

Phys. Rev. Lett., vol. 94, p. 146102, Apr 2005. [Online]. Available: http://link.aps.org/doi/10.1103/PhysRevLett.94.146102

[21] B. Damilano, N. Grandjean, C. Pernot, and J. Massies, "Monolithic White Light Emitting Diodes Based on InGaN/GaN Multiple-Quantum Wells," *Japanese Journal of Applied Physics*, vol. 40, no. 9A, p. L918, 2001. [Online]. Available: http://stacks.iop.org/1347-4065/40/i=9A/a=L918

[22] M. Lopez, F. Sacconi, M. A. der Maur, A. Pecchia, and A. Di Carlo, "Atomistic simulation of InGaN/GaN quantum disk LEDs," *Optical and Quantum Electronics*, vol. 44, no. 3-5, pp. 89–94, 2012.

[23] S. Strite and H. Morkoc, "GaN, AlN and InN: A review," *J. Vac. Sci. Technol. B*, vol. 10, no. 4, pp. 1237 – 1266, 1992.

[24] H. Amano, M. Kito, K. Hiramatsu, and I. Akasaki, "P-Type Conduction in Mg-Doped GaN Treated with Low-Energy Electron Beam Irradiation (LEEBI)," *Japanese Journal of Applied Physics*, vol. 28, no. 12A, p. L2112, 1989. [Online]. Available: http://stacks.iop.org/1347-4065/28/i=12A/a=L2112

[25] S. Nakamura, T. Mukai, and M. Senoh, "High-Power GaN P-N Junction Blue-Light-Emitting Diodes, journal=Japanese Journal of Applied Physics," vol. 30, no. 12A, p. L1998, 1991. [Online]. Available: http://stacks.iop.org/1347-4065/30/i=12A/a=L1998

[26] S. Nakamura, M. Senoh, and T. Mukai, "P-GaN/N-InGaN/N-GaN Double-Heterostructure Blue-Light-Emitting Diodes," *Japanese Journal of Applied Physics*, vol. 32, no. 1A, p. L8, 1993. [Online]. Available: http://stacks.iop.org/1347-4065/32/i=1A/a=L8

[27] L. R. Ram-Mohan, K. H. Yoo, and J. Moussa, "The SchrdingerPoisson self-consistency in layered quantum semiconductor structures," *Journal of Applied Physics*, vol. 95, no. 6, 2004.

[28] R.-C. Chen and J.-L. Liu, "A quantum corrected energy-transport model for nanoscale semiconductor devices," *Journal of Computational Physics*, vol. 204, no. 1, pp. 131 – 156, 2005. [Online]. Available: http://www.sciencedirect.com/science/article/pii/S0021999104004115

[29] F. Bertazzi, X. Zhou, M. Goano, G. Ghione, and E. Bellotti, "Auger recombination in InGaN/GaN quantum wells: A full-Brillouin-zone study," *Appl. Phys. Lett.*, vol. 103, no. 8, pp. –, 2013. [Online]. Available: http://scitation.aip.org/content/aip/journal/apl/103/8/10.1063/1.4819129

[30] S. S. Suslov, V. E. Bougrov, M. A. Odnoblyudov, and A. E. Romanov, "Modelling and optimization of electric current spreading in III-nitride LEDs," *physica status solidi (c)*, vol. 9, no. 3-4, pp. 1105–1108, 2012. [Online]. Available: http://dx.doi.org/10.1002/pssc.201100171

[31] K. Bulashevich, V. Mymrin, S. Karpov, I. Zhmakin, and A. Zhmakin, "Simulation of visible and ultra-violet group-III ni-

tride light emitting diodes," *Journal of Computational Physics*, vol. 213, no. 1, pp. 214 – 238, 2006. [Online]. Available: http://www.sciencedirect.com/science/article/pii/S0021999105003785

[32] M. V. Kisin and H. S. El-Ghoroury, "Modeling of injection characteristics of polar and nonpolar III-nitride multiple quantum well structures," *Journal of Applied Physics*, vol. 107, no. 10, pp. –, 2010. [Online]. Available: http://scitation.aip.org/content/aip/journal/jap/107/10/10.1063/1.3427540

[33] G.-B. Lin, D.-Y. Kim, Q. Shan, J. Cho, E. Schubert, H. Shim, C. Sone, and J. K. Kim, "Effect of Quantum Barrier Thickness in the Multiple-Quantum-Well Active Region of GaInN/GaN Light-Emitting Diodes," *Photonics Journal, IEEE*, vol. 5, no. 4, pp. 1 600 207–1 600 207, Aug 2013.

[34] S. Y. Karpov and Y. N. Makarov, "Dislocation effect on light emission efficiency in gallium nitride," *Appl. Phys. Lett.*, vol. 81, no. 25, 2002.

[35] "Effects of the spontaneous polarization and piezoelectric fields on the luminescence spectra of GaN/Al0.15Ga0.85N quantum wells," *Physica E: Low-dimensional Systems and Nanostructures*, vol. 7, no. 34, pp. 929 – 933, 2000. [Online]. Available: http://www.sciencedirect.com/science/article/pii/S1386947700000904

[36] J. Piprek and S. Li, "Electron leakage effects on GaN-based light-emitting diodes," *Optical and Quantum Electronics*, vol. 42, no. 2, pp. 89–95, 2010. [Online]. Available: http://dx.doi.org/10.1007/s11082-011-9437-z

[37] A. Efremov, N. Bochkareva, R. Gorbunov, D. Lavrinovich, Y. Rebane, D. Tarkhin, and Y. Shreter, "Effect of the joule heating on the quantum efficiency and choice of thermal conditions for high-power blue InGaN/GaN LEDs," *Semiconductors*, vol. 40, no. 5, pp. 605–610, 2006. [Online]. Available: http://dx.doi.org/10.1134/S1063782606050162

[38] V. C. K. Yalavarthi and S. Ahmed, "How important is nonlinear piezoelectricity in wurtzite GaN/InN/GaN quantum disk-in-nanowire LED structures?" *Opt Quant Electron*, vol. 46, pp. 925–933, 2014.

[39] S. Y. Karpov, *Nitride Semiconductor Devices: Principles and Simulation*. Ed. Wiley-VCH Verlag GmbH & Co. KGaA, Weinheim, Germany, 2007, ch. Visible Light-Emitting Diodes, pp. 303–325.

[40] B. G. Yacobi, *Semiconductor Materials: An Introduction to Basic Principles. Mircrodevices:Physics and Fabrication Technologies.* Kluwer Academic/Plenum Publishers, New York, 2003.

[41] S. Borowitz, *Fundamentals of Quantum Mechanics*, W. A. Benjamin, Ed. New York, 1969.

[42] D. M. Sullivan and D. S. Citrin, "Determination of the eigenfunctions of arbitrary nanostructures using time domain simulation," *Journal of Applied Physics*, vol. 91, pp. 3219–3226, Mar. 2002.

[43] R. Anderson, “Germanium-Gallium Arsenide Heterojunctions [Letter to the Editor],” *IBM Journal of Research and Development*, vol. 4, no. 3, pp. 283–287, July 1960.

[44] M. Grupen and K. Hess, “Simulation of carrier transport and nonlinearities in quantum-well laser diodes,” *Quantum Electronics, IEEE Journal of*, vol. 34, no. 1, pp. 120–140, Jan 1998.

[45] M. Grupen, K. Hess, and G. H. Song, “Simulation of transport over heterojunctions,” in *Proc. 4th Int. Conf. Simul. Semicon. Dev. Process*, vol. 4, 1991, pp. 303–311.

[46] K. Yang, J. R. East, and G. I. Haddad, “Numerical modeling of abrupt heterojunctions using a thermionic-field emission boundary condition,” *Solid-State Electronics*, vol. 36, no. 3, pp. 321–330, 1993.

[47] C. Crowell and V. Rideout, “Normalized thermionic-field (T-F) emission in metal-semiconductor (Schottky) barriers,” *Solid-State Electronics*, vol. 12, no. 2, pp. 89 – 105, 1969. [Online]. Available: http://www.sciencedirect.com/science/article/pii/0038110169901178

[48] A. A. Grinberg, “Thermionic emission in heterosystems with different effective electronic masses,” *Phys. Rev. B*, vol. 33, pp. 7256–7258, May 1986. [Online]. Available: http://link.aps.org/doi/10.1103/PhysRevB.33.7256

[49] C. Wu and E. Yang, "Carrier transport across heterojunction interfaces," *Solid-State Electronics*, vol. 22, no. 3, pp. 241 – 248, 1979. [Online]. Available: http://www.sciencedirect.com/science/article/pii/0038110179900285

[50] S. Hojfeldt and J. Mork, "Modeling of carrier dynamics in quantum-well electroabsorption modulators," *Selected Topics in Quantum Electronics, IEEE Journal of*, vol. 8, no. 6, pp. 1265–1276, Nov 2002.

[51] U. Mishra and J. Singh, *Semiconductor Device Physics and Design*. Springer Netherlands, 2007. [Online]. Available: http://books.google.com.sa/books?id=7WKOfUR-8M4C

[52] S. Chuang, *Physics of Optoelectronic Devices*, ser. Wiley Series in Pure and Applied Optics. Wiley, 1995. [Online]. Available: http://books.google.com.sa/books?id=ect6QgAACAAJ

[53] K. Brennan, *The Physics of Semiconductors: With Applications to Optoelectronic Devices*. Cambridge University Press, 1999. [Online]. Available: https://books.google.com.sa/books?id=6JElXbZpX3IC

[54] S. Datta, *Quantum phenomena*, ser. Modular Series on Solid State Devices, Vol 8. Addison-Wesley Longman, Incorporated, 1989. [Online]. Available: http://books.google.com.sa/books?id=xBcoAQAAMAAJ

[55] V. O. Turin, "A modified transferred-electron high-field mobility model for GaN devices simulation," *Solid-State Electronics*, vol. 49, no. 10, pp. 1678 – 1682, 2005.

[56] L.-A. Yang, Y. Hao, Q. Yao, and J. Zhang, "Improved Negative Differential Mobility Model of GaN and AlGaN for a Terahertz Gunn Diode," *Electron Devices, IEEE Transactions on*, vol. 58, no. 4, pp. 1076–1083, April 2011.

[57] M. A. Z. Abou El-Ela, F. M., "Electron Transport Characteristics of Wurtzite GaN," *ISRN Condensed Matter Physics*, vol. 2013, p. 6, 2013.

[58] F. Schwierz, "An electron mobility model for wurtzite GaN," *Solid-State Electronics*, vol. 49, no. 6, pp. 889 – 895, 2005.

[59] M. Farahmand, C. Garetto, E. Bellotti, K. F. Brennan, M. Goano, E. Ghillino, G. Ghione, J. Albrecht, and P. Ruden, "Monte-Carlo simulation of electron transport in the III-nitride wurtzite phase materials system: binaries and ternaries," *Electron Devices, IEEE Transactions on*, vol. 48, no. 3, pp. 535–542, Mar 2001.

[60] R. Thomas, "Carrier mobilities in silicon empirically related to doping and field," *Proceedings of the IEEE*, vol. 55, no. 12, pp. 2192–2193, Dec 1967.

[61] E. Bellotti and F. Bertazzi, *Nitride Semiconductor Devices: Principles and Simulation.* Ed. Wiley-VCH Verlag GmbH & Co. KGaA, 2007, ch. Transport Parameters for Electrons and Holes, pp. 69–93.

[62] C. Jacoboni and L. Reggiani, "The Monte Carlo method for the solution of charge transport in semiconductors with applications to covalent materials," *Rev. Mod. Phys.*, vol. 55, pp. 645–705, Jul 1983. [Online]. Available: http://link.aps.org/doi/10.1103/RevModPhys.55.645

[63] C. Mauder, B. Reuters, L. R. Khoshroo, M. Rzheutskii, E. Lutsenko, G. Yablonskii, J. Woitok, M. Heuken, H. Kalisch, and R. Jansen, "Development of m-plane GaN anisotropic film properties during {MOVPE} growth on LiAlO2 substrates," *Journal of Crystal Growth*, vol. 312, no. 11, pp. 1823 – 1827, 2010. [Online]. Available: http://www.sciencedirect.com/science/article/pii/S0022024810001697

[64] G. Umana Membreno, T. Fehlberg, S. Kolluri, D. Brown, G. Parish, B. Nener, S. Keller, U. Mishra, and L. Faraone, "Mobility spectrum analysis of anisotropic electron transport in N-polar GaN/AlGaN heterostructures on vicinal sapphire substrates," *Microelectronic Engineering*, vol. 88, no. 7, p. 10791082, 2011.

[65] J. F. F. M. Shulong Wang, Hongxia Liu and X. Lei, "Anisotropic longitudinal electron diffusion coefficient in wurtzite gallium nitride," *Appl. Phys. A*, vol. 112, no. 4, pp. 933–938, Sep 2013.

[66] F. Bernardini, *Nitride Semiconductor Devices: Principles and Simulation, chapter = Spontaneous and piezoelectric polarization: Basic theory vs. practical recipes.* Ed. Wiley-VCH Verlag GmbH & Co. KGaA, Weinheim, Germany, 2007, pp. 49–67.

[67] F. Bernardini, V. Fiorentini, and D. Vanderbilt, "Spontaneous polarization and piezoelectric constants of III-V nitrides," *Phys. Rev.*

B, vol. 56, pp. R10 024–R10 027, Oct 1997. [Online]. Available: http://link.aps.org/doi/10.1103/PhysRevB.56.R10024

[68] E. T. Yu, G. J. Sullivan, P. M. Asbeck, C. D. Wang, D. Qiao, and S. S. Lau, “Measurement of piezoelectrically induced charge in GaN/AlGaN heterostructure field-effect transistors,” *Appl. Phys. Lett.*, vol. 71, no. 19, 1997.

[69] T. Takeuchi, S. Sota, M. Katsuragawa, M. Komori, H. Takeuchi, H. Amano, and I. Akasaki, “Quantum-Confined Stark Effect due to Piezoelectric Fields in GaInN Strained Quantum Wells,” *Japanese Journal of Applied Physics*, vol. 36, no. 4A, p. L382, 1997. [Online]. Available: http://stacks.iop.org/1347-4065/36/i=4A/a=L382

[70] M. F. Schubert and E. F. Schubert, “Effect of heterointerface polarization charges and well width upon capture and dwell time for electrons and holes above GaInN/GaN quantum wells,” *Appl. Phys. Lett.*, vol. 96, no. 13, pp. –, 2010. [Online]. Available: http://scitation.aip.org/content/aip/journal/apl/96/13/10.1063/1.3373610

[71] D. Zhu, A. N. Noemaun, M. F. Schubert, J. Cho, E. F. Schubert, M. H. Crawford, and D. D. Koleske, “Enhanced electron capture and symmetrized carrier distribution in GaInN light-emitting diodes having tailored barrier doping,” *Appl. Phys. Lett.*, vol. 96, no. 12, 2010.

[72] J. Xu, M. F. Schubert, D. Zhu, J. Cho, E. F. Schubert, H. Shim, and C. Sone, “Effects of polarization-field tuning in GaInN light-emitting

diodes," *Appl. Phys. Lett.*, vol. 99, no. 4, pp. –, 2011. [Online]. Available: http://scitation.aip.org/content/aip/journal/apl/99/4/10.1063/1.3609783

[73] R. D. Underwood, P. Kozodoy, S. Keller, S. P. DenBaars, and U. K. Mishra, "Piezoelectric surface barrier lowering applied to InGaN/GaN field emitter arrays," *Appl. Phys. Lett.*, vol. 73, no. 3, 1998.

[74] E. T. Yu, X. Z. Dang, P. M. Asbeck, S. S. Lau, and G. J. Sullivan, "Spontaneous and piezoelectric polarization effects in IIIV nitride heterostructures," *Journal of Vacuum Science & Technology B*, vol. 17, no. 4, pp. 1742–1749, 1999. [Online]. Available: http://scitation.aip.org/content/avs/journal/jvstb/17/4/10.1116/1.590818

[75] F. Bernardini and V. Fiorentini, "Nonlinear Behavior of Spontaneous and Piezoelectric Polarization in IIIV Nitride Alloys," *physica status solidi (a)*, vol. 190, no. 1, pp. 65–73, 2002. [Online]. Available: http://dx.doi.org/10.1002/1521-396X(200203)190:1¡65::AID-PSSA65¿3.0.CO;2-0

[76] V. Fiorentini, F. Bernardini, and O. Ambacher, "Evidence for nonlinear macroscopic polarization in IIIV nitride alloy heterostructures," *Appl. Phys. Lett.*, vol. 80, no. 7, 2002.

[77] F. Bernardini and V. Fiorentini, "Polarization fields in nitride nanostructures: 10 points to think about ," *Applied Surface Science*, vol. 166, no. 14, pp. 23 – 29, 2000, 7^{TH} INTERNATIONAL CONF. ON

FORMATION OF SEMICONDUCTOR INTERFACES. [Online]. Available: http://www.sciencedirect.com/science/article/pii/S0169433200004347

[78] S. S. Sundaresan, V. M. Gaddipati, and S. S. Ahmed, “Effects of spontaneous and piezoelectric polarization fields on the electronic and optical properties in GaN/AlN quantum dots: multimillion-atom sp3d5s* tight-binding simulations,” *International Journal of Numerical Modelling: Electronic Networks, Devices and Fields*, 2014.

[79] J. F. Nye, *Physical Properties of Crystals: Their Representation by Tensors and Matrices.* Oxford at the Clarendon Press, 1964.

[80] P.-Y. Prodhomme, A. Beya-Wakata, and G. Bester, “Nonlinear piezoelectricity in wurtzite semiconductors,” *Phys. Rev. B*, vol. 88, p. 121304, Sep 2013.

[81] F. Bernardini and V. Fiorentini, “Nonlinear macroscopic polarization in III-V nitride alloys,” *Phys. Rev. B*, vol. 64, p. 085207, Aug 2001. [Online]. Available: http://link.aps.org/doi/10.1103/PhysRevB.64.085207

[82] T. Goudon, V. Miljanovi, and C. Schmeiser, “On the ShockleyReadHall Model: Generation-Recombination in Semiconductors,” *SIAM Journal on Applied Mathematics*, vol. 67, no. 4, pp. 1183–1201, 2007.

[83] S. M. Lee, M. A. Belkhir, X. Y. Zhu, Y. H. Lee, Y. G. Hwang, and T. Frauenheim, “Electronic structures of GaN edge dislocations,” *Phys. Rev. B*, vol. 61, pp. 16 033–16 039, Jun 2000.

[84] W. Shockley and W. T. Read, “Statistics of the Recombinations of Holes and Electrons,” *Phys. Rev.*, vol. 87, pp. 835–842, Sep 1952.

[85] Z. Bandi, P. Bridger, E. Piquette, and T. McGill, “The values of minority carrier diffusion lengths and lifetimes in GaN and their implications for bipolar devices,” *Solid-State Electronics*, vol. 44, no. 2, pp. 221 – 228, 2000.

[86] S. R. V. Bougrov, M. Levinshtein and A. Zubrilov, *Properties of Advanced Semiconductor Materials: GaN, AlN, InN, BN, SiC, SiGe.* Wiley, New York, 2001, ch. 1, p. 2.

[87] Y. C. Shen, G. O. Mueller, S. Watanabe, N. F. Gardner, A. Munkholm, and M. R. Krames, “Auger recombination in InGaN measured by photoluminescence,” *Appl. Phys. Lett.*, vol. 91, no. 14, 2007.

[88] Q. Dai, Q. Shan, J. Wang, S. Chhajed, J. Cho, E. F. Schubert, M. H. Crawford, D. D. Koleske, M.-H. Kim, and Y. Park, “Carrier recombination mechanisms and efficiency droop in GaInN/GaN light-emitting diodes,” *Appl. Phys. Lett.*, vol. 97, no. 13, 2010.

[89] M. Meneghini, N. Trivellin, G. Meneghesso, E. Zanoni, U. Zehnder, and B. Hahn, “A combined electro-optical method for the determination of the recombination parameters in InGaN-based light-emitting diodes,” *Journal of Applied Physics*, vol. 106, no. 11, 2009.

[90] A. De Mari, "An accurate numerical one-dimensional solution of the P-N junction under arbitrary transient conditions," in *Electron Devices Meeting, 1967 International*, vol. 13, 1967, pp. 100–100.

[91] D. M. Sullivan, *Quantum Mechanics for Electrical Engineers.* IEEE Press, 2012.

[92] D. M. Sullivan and P. M. Wilson, "Time-domain determination of transmission in quantum nanostructures," *Journal of Applied Physics*, vol. 112, no. 6, pp. –, 2012. [Online]. Available: http://scitation.aip.org/content/aip/journal/jap/112/6/10.1063/1.4754812

[93] D. M. Sullivan and D. S. Citrin, "Determination of the eigenfunctions of arbitrary nanostructures using time domain simulation," *Journal of Applied Physics*, vol. 91, no. 5, 2002.

[94] C. Snowden, *Semiconductor device modelling.* Springer-Verlag, 1989. [Online]. Available: http://books.google.com.sa/books?id=WRdTAAAAMAAJ

[95] P. Shah, V. Mitin, M. Grupen, G. H. Song, and K. Hess, "Numerical simulation of wide bandgap AlGaN / InGaN lightemitting diodes for output power characteristics and emission spectra Numerical simulation of wide band-gap AlGaN / InGaN light-emitting diodes for output power characteristics and emission spectra," *Appl. Phys. Lett.*, vol. 2755, no. 79, 1996.

Vitae

- Name : Irfan Khan
- Nationality : Pakistan
- Date of Birth : March 25, 1988
- Email : *irfan_345@hotmail.com*
- Academic Background :
  - Master of Science in Electrical Engineering, King Fahd University of Petroleum and Minerals, Dhahran, Saudi Arabia, April 2015
  - Bachelor of Science in Electronic Engineering, Ghulam Ishaq Khan Institute of Engineering Sciences & Technology, Pakistan, June 2010
- Publications :
  - Khan, I., Susilo, Tri B., Alsunaidi, M. A., Analysis of a Graded-well Graded-EBL Light-emitting Diode Structures, Accepted at IC-MAT2015.
  - Susilo, Tri B., Khan, I., Alsunaidi, M. A., Modelling, Identification and Verification of Intermixing Process in Coupled InGaN/GaN Multiple Quantum Wells, Accepted at ICMAT 2015.

- Khan, I.; Alsunaidi, M.A., ”Tuning of bowtie nano-antenna resonance using As2S3 chalcogenide glass substrate,” 8th IEEE GCC Conference and Exhibition (GCCCE), 2015, pp.1,4, 1-4 Feb. 2015.
- Susilo, Tri B., Khan, I., Chao S., Ooi, Boon S., Alsunaidi, M. A.: Intermixing effects on emission properties of InGaN/GaN coupled quantum wells, In: The 3rd Saudi International Nanotechnology Conference, 2014. (presented)
- M. Shemis, M. Gondal, E. Alkhazrajib, M. Najmib, M. A. Abalkhail, I. Khan, T. B. Susilo, S. G. Rashid and M. A. Alsunaidi, Synthesis and Photoluminescence of Metal Coated ZnO Nanoparticles, IEEE HONET 2014, Charlotte, NC, USA.
- Ahmad, F.; Khan, I; Mahmud, S.A; Khan, G.M.; Yousaf, F.Z., ”Real time evaluation of shortest remaining processing time based schedulers for traffic congestion control using wireless sensor networks,” International Conference on Connected Vehicles and Expo (ICCVE), pp.381,387, 2-6 Dec. 2013.